

**Towards the Synthesis of Redox-active  
Ferrocene-based  
Macrocycles via Successive Ring Expansion  
(SuRE)**

**Lucy Hudson, BSc**

**MSc by Research**

**University of York**

**Chemistry**

**December 2022**

# Abstract

Due to their exceptional properties, macrocycles have been investigated for a broad range of applications including use in therapeutics,<sup>1</sup> catalysis,<sup>2</sup> chemical sensors,<sup>3-5</sup> peptide mimics,<sup>6-8</sup> and molecular electronics.<sup>9</sup> Functionalisation allows these properties to be altered, allowing fine-tuning of macrocycles for these applications. Ferrocene is of interest for inclusion into macrocycles due to its unique characteristics such as its mild oxidation to ferrocenium, along with its optical and mechanical properties. Incorporation of ferrocene into a macrocycle is therefore likely to have a significant impact on the redox, optical and mechanical properties of the whole macrocycle. The synthesis of ferrocene-containing macrocycles is therefore an exciting avenue to widen the scope of macrocyclic chemistry. However, there are many drawbacks associated with current methods for the synthesis of both organic and ferrocene-containing macrocycles. These include poor selectivity, difficulty synthesising larger rings and the formation of by-products resulting in lower yields. Therefore, it would be advantageous to develop alternative methods towards the synthesis of ferrocene-containing macrocycles, and this is the focus of this Master's thesis.

SuRE (Successive Ring Expansion) is an attractive alternative to currently used methods for macrocycle synthesis as it allows high control and selectivity over linear side-products and is able to be done successively.<sup>10,11</sup> This project aimed to investigate the use of SuRE in the formation of ferrocene-containing macrocycles and analyse the optical and redox properties of ferrocene-containing precursors. Two ferrocene-containing starting materials for use in SuRE were successfully synthesised and SuRE was attempted using a variety of conditions. Unfortunately, the conditions tested led to decomposition and favoured the formation of the acid anhydride side-product. This is likely due to the proximity of the acid chloride functional group with ferrocene's Cp ring. Nonetheless, the properties of ferrocene-containing precursors were analysed by DFT calculations, cyclic voltammetry and UV-Visible spectroscopy.

# List of Contents

Abstract .....	2
List of Contents .....	3
List of Tables.....	5
List of Figures & Schemes .....	5
Acknowledgements .....	12
Declaration.....	13
1. Introduction.....	13
1.1 <i>Macrocycles</i> .....	13
1.2 <i>Synthesis of Macrocycles and Medium-Sized Rings: End-to-End Cyclisation</i> .....	22
1.3 <i>Synthesis of Macrocycles and Medium-sized Rings: Ring Expansions</i> .....	25
1.4 <i>Synthesis of Macrocycles: Successive Ring Expansion (SuRE)</i> .....	33
1.5 <i>Introduction to Ferrocene</i> .....	39
1.6 <i>Ferrocene Properties and Uses</i> .....	40
1.7 <i>Ferrocene-containing Macrocycles</i> .....	48
1.8 <i>Synthesis of Ferrocene Macrocycles</i> .....	52
1.8 <i>Project Aims</i> .....	55
2. Synthesis of SuRE Starting Material 2.5 .....	57
3. SuRE: Acyl Chloride Formation .....	65
4. SuRE: <i>N</i> -acylation .....	69
4.1 <i>General N-acylation Conditions</i> .....	69
4.2 <i>Alternative N-acylation Conditions</i> .....	71
5. Synthesis of SuRE Starting Material 2.26 .....	74

6. Electrochemistry & UV-Visible Spectroscopy .....	78
7. Further Work.....	86
8. Conclusion and Summaries .....	87
9. Experimental.....	90
Appendices .....	104
Abbreviations .....	123
References .....	124

## List of Tables

Table 1. Relationship between charge transfer interference and rotational conformation of the ferrocene (Fc) Cp rings

Table 2. Table of the purification methods and reagent addition methods with yields in the formation of **2.3**.

Table 3. Optimisation table for the formation of **2.4** and by-product **2.5**. \* x2 Net<sub>3</sub>, x5 scale

Table 4. Investigation of whether purification of the DPPA contaminant from crude **2.4** improves yield of **2.5**

Table 5. Table of the wavelengths of MLCT and  $\pi$ - $\pi^*$  transfer bands of compounds **2.1**, **2.4**, **2.6**, **2.19** and **2.20**.

Table 6. Electrochemical analysis of compounds **2.1**, **2.4-2.6**, **2.19** and **2.20** including  $E_{pa}$  and  $E_{pc}$  along with calculated values of  $\Delta E_p$ ,  $E_{1/2}$  and  $i_{pa}/i_{pc}$ .

Appendix Table 1. Crystal data for **2.4**.

Appendix Table 2. Crystal data for **2.5**.

Appendix Table 3. Crystal data for **2.20**.

Appendix Table 4. Crystal data for **2.22**.

Appendix Table 5. Crystal data for **2.24**

## List of Figures & Schemes

Figure 1. Examples of applications of macrocycles.

Figure 2. The drug candidate compound **1.1**, a macrocyclic peptide first isolated from *Zinnia elegans* seeds. Compound **1.1** has attractive traits such as proteolysis resistance and the ability to permeate cells. These and others have allowed it to act as a small molecule character to carry the drug Daunorubicin directly to cancer cell lines. Image reproduced from article by Payne et al.,<sup>12</sup>, no permissions required.

Figure 3. Macrocyclic drug candidate compound **1.2**, which is currently in clinical trials for treatment of the autoimmune disorder, generalized myasthenia gravis.<sup>13</sup>

Figure 4. The sequential reduction of compound **1.3** and binding of Lithium ions, facilitated by through-space electron delocalisation.

Figure 5. Differences in oxidation potential between cyclic (c-pPn) and linear (l-pPn) p-phenylene polymers. Quinoidal distortion caused by structural reorganisation in l-pPn is illustrated.

Figure 6. Monomer of a self-insulating interlocked molecular wire, **1.4**, synthesised by Sugiyasu et al.,<sup>14</sup>

Figure 7. Mechanical properties and structure of molecular necklace, **1.5**. Shifting pattern of **1.5.1** (red) can be split into 1) dissociation of host-guest recognition; 2) sliding of the **1.5.1** units along the bis(pyridinium) ligand; 3) bond deformation and finally; 4) metal-coordination dissociation. HG = host-guest complex.

Figure 8. Synthesis of TADF co-crystals via host-guest chemistry.

Figure 9. Diagram of how curubit[n]uril, **1.8**, facilitates the electrocatalysis of CO<sub>2</sub>. Yellow = gold electrode, Red = Oxygen, Green = Carbon. Inspired by figures from Wagner et al.

Figure 10. Host-guest interaction of Alzheimer's protein markers with compound **1.9**, resulting in \*activation of the dye and detection of a fluorescent signal.

Scheme 1. Generalised scheme for macrocyclization via reaction of end groups (end-to-end cyclisation) and its competing dimerization reactions.

Scheme 2. a) direct cyclisation attempt to synthesis compound **1.15**. b) Synthesis of compound **1.15** using tethering approach followed by ring contraction.

Scheme 3. RCM of diene precursors.

Scheme 4. CuAAC click reaction to form a macrocyclic precursor for the synthesis of ligand **1.26** in 72 % yield. TIPS = Triisopropylsilyl ether.

Scheme 5. Ring expansion via stabilisation of a radical in the intermediate, ring expanded product.

Scheme 6. Radical promoted ring opening using photocatalysis.

Scheme 7. Ring expansion using Sommelet–Hauser [2,3]-sigmatropic rearrangement

Figure 11. Formation of compound **1.45** via photochemical rearrangement (blue) followed by the thermal [1,5]-sigmatropic H-shift (red).

Figure 12. Ring expansion via bicyclic rings. a) from a bicyclic starting material; b) via a bicyclic intermediate.

Scheme 8. Ring expansion via Grob fragmentation to form Jatrophatrione.

Scheme 9. Ring expansion using Eschenmoser fragmentation in the formation of musk analogues. Ts = tosyl.

Scheme 10. Ring expansion techniques using redox-mediated oxidations. a) *in situ* initiation of Grob/Eschenmoser-type fragmentation b) ozonolysis

Scheme 11. Ring expansion via side chain insertion, promoted by ring-strain relief.

Scheme 12. Ring expansion via side chain insertion promoted by an electron-withdrawing nitro group. TBAF = Tetra-n-butylammonium fluoride.

Scheme 13. 'zip' reaction by Hesse's group via the less energetically 10-membered medium-sized ring, followed by successive expansion to the more stable 14-membered ring.

Scheme 14. 'Zip' reaction by Hesse's group to form a 53-membered ring product from a 12-membered ring product.

Scheme 15. General SuRE reaction scheme. X = first functional group; Y = first attacking nucleophile; Z = second attacking nucleophile; PG = Protecting group.

Scheme 16. SuRE with  $\beta$ -ketoesters. Side chain insertion is achieved using  $MgCl_2$  and pyridine to promote C-acylation, followed by Fmoc deprotection which passes through a bicyclic intermediate to result in ring expansion. Successive expansions occur by repeating steps 1) and 2).

Scheme 17. SuRE with  $\beta$ -lactams. Side chain insertion is achieved using DMAP and pyridine to promote N-acylation, followed by Fmoc deprotection which passes through a bicyclic intermediate to result in ring expansion. Successive expansions occur by repeating steps 1) and 2).

Scheme 18. SuRE with thiolactones. Side chain insertion is achieved using DMAP and pyridine to promote N-acylation, followed by Fm deprotection which passes through a bicyclic intermediate to result in ring expansion.

Scheme 19. The accidental synthesis of ferrocene instead of bicyclopentadienyliidene when by from cyclopentadienylmagnesium bromide and  $FeCl_3$ .

Figure 13. Structure of ferrocene. a) structure proposed by Keally and Pauson in 1951 b) current structure accepted by the scientific community, proposed by Wilkinson and Woodward in 1952.

Scheme 20. The different reactivities of ferrocene. Inspired by a figure from Didier Astruc's review.<sup>15</sup>

Figure 14. One electron oxidation of ferrocene to its ferrocenium ion. Colour change is from orange to dark blue. Oxidation occurs at +0.4 V vs. SCE.

Scheme 21. The ROP of different monomeric rings such as L-lactide illustrated here, by a ferrocene-linked aluminium complex developed by Lai et al.,<sup>16</sup>

Figure 15. Ferrocene-based redox sensor. The device is able to detect glucose via transfer of a charge to a rGO electrode. Electrons are passed from glucose bound to glucose oxidase, to FADH<sub>2</sub>, to ferrocenium and a charge is detected by a rGO electrode.

Figure 16. DSFO<sup>+</sup> molecular wire developed by Bazan's group<sup>17</sup>

Figure 17. Thiol terminated ferrocene molecular wires developed by Xiao et al.,<sup>18</sup>

Figure 18. Generalised diagram of a ferrocenophane. Ferrocene's Cp rings are able to tilt by up to 30° to form a 60° between the centre of the Cp ring and the iron centre

Figure 19. The ROP of carbon-bridged [2]ferrocenophanes to form poly(ferrocenylethylene)s

Figure 20. Tilting of ferrocene's Cp rings to allow coordination of **1.227** in a metal ion  $\kappa^3$  coordinated system and non-tilted  $\kappa^2$  coordinated system **1.228**. D= donor atom, M=metal, L=ligand

Figure 21. Rotation of ferrocene's Cp ring between eclipsed ( $D_{5h}$ ) and staggered ( $D_{5d}$ ) conformations via a small energy barrier of 4 kJmol<sup>-1</sup>.

Figure 22. One electron oxidation of ferrocene its ferrocenium ion. Colour change is from red to blue. Oxidation occurs at +0.4 V vs. SCE.

Figure 23. Ferrocene-based environmental sensor developed by Zapata et al.,<sup>85</sup> binding of Hg<sup>2+</sup> shifts UV-Visible absorption spectra.

Figure 24. Different types of ferrocene macrocycles. a) exo-functionalised; b) endo-functionalised; c) edge-functionalised and; c) corner-functionalised.

Scheme 22. **1.134** which incorporates six ferrocene-1,1'-diyl units.

Figure 25. Ferrocene-containing covalent organic framework nanosheets, compound **1.131**, assembled on gold electrodes for use in early detection of AMI.

Figure 26. Cyclic ferrocene-peptide conjugate **1.138**, used to mimic with a 1,2'-conformation with respect to the ferrocene moiety.

Figure 27. Electrochemically controlled conjugate macrocycle **1.139**. Upon oxidation the ferrocene-ring moves into the pillar[6]arene to form a host-guest complex

Scheme 23. RCM of olefin monomers.

Scheme 24. TROP of strained ferrocenophanes **1.140** and **1.141** to form cyclic polymer **1.142**.

Scheme 25. Sonogashira cross-coupling and Ullmann-like coupling to form ridged ferrocene-containing macrocycles.

Scheme 26. Coordination-driven formation of ferrocene-containing macrocycles.

Scheme 27. Synthesis of ferrocene containing macrocycles, **1.153** via SuRE.

Scheme 28. Proposed Synthetic Pathway for **2.5**

Scheme 29. Reaction scheme and mechanism for the formation of **2.1** and by-product **2.2** from the Friedel-Crafts acylation of ferrocene

Scheme 30. Reaction scheme and mechanism for the formation of **2.3** from the haloform reaction of **2.1**.

Scheme 31. Reaction scheme and mechanism of the acyl azide **2.4**, followed by the Curtius rearrangement to form **2.5**.

Scheme 32. Reaction scheme for the synthesis of **2.4** and the by-product **2.6** from **2.3** via acyl azide formation.

Scheme 33. Reaction scheme of the acyl azide **2.4**, followed by the Curtius rearrangement to form **2**.

Scheme 34. The Curtius rearrangement of **2.4** upon heating and trapping with Fmoc-OH to form **2.5** or trapping with water to form **2.4.3** and **2.4.4**

Scheme 35. Final synthetic method resulting in 15 % yield for **2.5** from **2.3** across a 2-step pathway.

Scheme 36. General SuRE methodology using a ferrocene-starting material. PG= protecting group, DMAP.

Scheme 37. conversion of **2.5** into **2.7** by the action of oxalyl chloride and DMF.

Scheme 38. Synthesis of **2.9** from **2.8** using oxalyl chloride in and DMF.

Scheme 39. Trapping of ferrocenyl acyl-chlorides. a) Trapping of **2.9** with methanol, b) Trapping of **2.7** with methanol, c) Trapping of **2.9** with aniline, d) Trapping of **2.7** with aniline.

Scheme 40. General scheme for SuRE using a ferrocene-containing starting material. PG = protecting group, DMAP = 4-Dimethylaminopyridine

Scheme 41. Attempts at the N-acylation step of SuRE. a) Using 13-membered lactam and stirring for 1 h; b) using 13-membered lactam and stirring for 12 h; c) using a 6-membered lactam and stirring for 16 h.

Scheme 42. Formation of acid anhydride by-product **2.18** in place of the intended imide **2.15**

Scheme 43. Schemes showing the different N-acylation reagents tested and the product (**2.19**, **2.21**) and by-product (**2.20**, **2.18**) yields. a) reacting **2.9** with DMAP and pyridine; b) reacting **2.9** with NEt<sub>3</sub>; c) reacting **2.9** with MeMgBr d) reacting **2.7** with DMAP and pyridine.

Scheme 44. Reaction of **2.9** with the work-up agent NH<sub>4</sub>Cl to form **2.22**

Scheme 45. Proposed Synthetic Pathway for **2.6**

Scheme 46. Reaction scheme for the esterification of **2.8** to form **2.23**.

Scheme 47. Reaction scheme and mechanism for the Friedel-Crafts acylation of **2.23** to form **2.24**.

Scheme 48. Reaction scheme and mechanism for the reduction of **2.23** to form **2.24**.

Scheme 49. Reaction schemes for alcohol protection on of **2.24** to form **2.25**. a) using strong base, NaH and benzyl bromide and b) using milder base Ag<sub>2</sub>O and benzyl bromide.

Scheme 50. Reaction scheme for the ester hydrolysis of **2.23** to form **2.24**.

Scheme 51. Reaction scheme for the introduction of into SuRE.

Figure 28. Shifting of peaks in the NMR spectra of **2.29** from the ferrocene region to the aromatic region of the NMR spectrum after stirring for 16 hours, indicating decomposition.

Figure 29. One electron oxidation of ferrocene its ferrocenium ion. Colour change is from red to blue. Oxidation occurs at +0.4 V vs. SCE.

Figure 30. Diagram illustrating the regions of the macrocycle which will have the most impact on optical and redox properties of the entire macrocycle, with the most influential being functional groups directly attached to the ferrocene.

Figure 31. The frontier molecular orbitals HOMO-3 to LUMO+3 of a) **2.4** and b) **2.3** as calculated by DFT.

Figure 32. The HOMO and LUMO of compound Fc and 2.1-2.6 in order of electron withdrawing ability of the Cp ring substituents

Figure 33. The energy of the frontier molecular orbitals (HOMO-3 to LUMO+3) for compounds **Fc** and **2.1-2.6** arranged from the highest to lowest energy HOMO.

Figure 34. UV-Visible spectra of compounds **2.1**, **2.4**, **2.20** and **2.6**

Figure 35. Electrochemical analysis of **2.20**. a) cyclic voltammogram at different scan rates; b) Scan rate dependence vs. voltage; c) current vs. the square root of scan rate.

Figure 36. Graph of  $E_{1/2}$  values of compounds **2.1-2.6**, **2.19** and **2.20**

Figure 37. a) XRD analysis of compound **2.5** b) CV analysis of **2.5**

Scheme 52. Possible SuRE starting materials **2.27** and **2.28** that incorporate a spacer between the Cp ring and the carboxylic acid functional group.

Appendix Figure 1. Crystal structure of **2.4** as discovered by XRD analysis

Appendix Figure 2. Crystal structure of **2.5** as discovered by XRD analysis

Appendix Figure 3. Crystal structure of **2.20** as discovered by XRD analysis

Appendix Figure 4. Crystal structure of **2.22** as discovered by XRD analysis.

Appendix Figure 5. Crystal structure of **2.24** as discovered by XRD analysis

Appendix Figure 6. Molecular orbitals of **Fc** calculated by DFT.

Appendix Figure 7. Molecular orbitals of **2.1** calculated by DFT.

Appendix Figure 8. Molecular orbitals of **2.3** calculated by DFT.

Appendix Figure 9. Molecular orbitals of **2.4** calculated by DFT

Appendix Figure 10. Molecular orbitals of **2.5** calculated by DFT.

Appendix Figure 11. Molecular orbitals of **2.6** calculated by DFT.

Appendix Figure 12. Molecular orbitals of **2.20** calculated by DFT.

Appendix Figure 13. UV-Visible spectrum of **2.1** at concentrations  $4.1 \times 10^{-4}$ ,  $2.0 \times 10^{-4}$ ,  $1.2 \times 10^{-5}$ ,  $8.1 \times 10^{-6}$ ,  $4.1 \times 10^{-7}$  and  $3.3 \times 10^{-8}$  M.

Appendix Figure 14. UV-Visible spectrum of **2.4** at concentrations  $3.3 \times 10^{-4}$ ,  $1.7 \times 10^{-4}$ ,  $1.0 \times 10^{-4}$ ,  $6.7 \times 10^{-5}$ ,  $3.3 \times 10^{-5}$ ,  $3.3 \times 10^{-5}$ ,  $2.7 \times 10^{-5}$  M.

Appendix Figure 15. UV-Visible spectrum of **2.6** at concentrations of  $3.0 \times 10^{-4}$ ,  $1.5 \times 10^{-4}$ ,  $1.2 \times 10^{-4}$ ,  $7.4 \times 10^{-5}$ ,  $1.5 \times 10^{-5}$  M.

Appendix Figure 16. UV-Visible spectrum of **2.19** at concentrations of  $2.6 \times 10^{-4}$ ,  $1.3 \times 10^{-4}$ ,  $7.7 \times 10^{-5}$ ,  $5.1 \times 10^{-5}$ ,  $2.6 \times 10^{-5}$ ,  $2.1 \times 10^{-5}$  M.

Appendix Figure 17. UV-Visible spectrum of **2.20** at concentrations  $2.8 \times 10^{-4}$ ,  $2.3 \times 10^{-4}$ ,  $1.8 \times 10^{-4}$ ,  $9.1 \times 10^{-5}$ ,  $4.5 \times 10^{-5}$  and  $3.6 \times 10^{-5}$  M.

Appendix Figure 18. Electrochemical analysis of **2.1**. a) cyclic voltammogram at different scan rates; b) Scan rate dependence vs. voltage; c) current vs. the square root of scan rate.

Appendix Figure 19. Electrochemical analysis of **2.4**. a) cyclic voltammogram at different scan rates; b) Scan rate dependence vs. voltage; c) current vs. the square root of scan rate.

Appendix Figure 20. Electrochemical analysis of **2.5**. a) cyclic voltammogram at different scan rates; b) Scan rate dependence vs. voltage; c) current vs. the square root of scan rate

Appendix Figure 21. Electrochemical analysis of **2.6**. a) cyclic voltammogram at different scan rates; b) Scan rate dependence vs. voltage; c) current vs. the square root of scan rate.

Appendix Figure 22. Electrochemical analysis of **2.19**. a) cyclic voltammogram at different scan rates; b) Scan rate dependence vs. voltage; c) current vs. the square root of scan rate

Appendix Figure 23. Electrochemical analysis of **2.20**. a) cyclic voltammogram at different scan rates; b) Scan rate dependence vs. voltage; c) current vs. the square root of scan rate

## Acknowledgements

Firstly, I would like to acknowledge my supervisors, Dr Luke Wilkinson and Dr William Unsworth who have helped me tirelessly throughout my project. They have both gone above and beyond their role as supervisors. Their enthusiasm, patience and encouragement helped me build confidence in the lab and write a thesis that I am proud of. Not only that, but they made the time I spent on this project incredibly enjoyable. For that I am very grateful. I truly believe any university or student would be incredibly lucky to work with either of them.

I would also like to thank Heather Fish and Alex Heyman for tirelessly maintaining the NMR equipment, along with Karl Heaton for his reliable work running mass spectroscopy samples and Adrian Whitwood and Theo Tanner for running and analysing XRD crystallography data, providing me with beautiful images of my compounds.

I would also like to thank the Wilkinson and Unsworth groups' for not only providing useful suggestions for any issues I had during my project, but also, along with the rest of the E214 lab, providing me with numerous friendships and lovely memories. Particularly, I would like to thank our former post doc Dr Christopher Golt, an amazing teacher, who always spared the time to answer any questions extremely patiently, along with Dr Iman Khazal who reliably runs the E214 lab and without whom, it might descend into chaos.

Finally, I would like to thank my summer student Oscar Schwabe. Oscar is an incredibly talented student who is responsible for a large chunk of the work in this thesis (the synthesis of starting material **2.26**) which he was able to do in under 8 weeks. Oscar was a pleasure to work with and I wish him luck with his degree and whatever he chooses to do next!

## Declaration

I declare that this thesis is a presentation of original work, and I am the sole author. This work has not previously been presented for an award at this, or any other, University. All sources are acknowledged as References.

# 1. Introduction

## 1.1 *Macrocycles*

For years, macrocycles have attracted attention for their unique properties and applications in areas such as therapeutics,<sup>1</sup> catalysis,<sup>2</sup> chemical sensors,<sup>3-5</sup> peptide mimics,<sup>6-8</sup> and molecular electronics (figure 1).<sup>9</sup> Significantly, macrocycles have attracted attention as cyclic peptide therapeutics as they often exhibit favourable properties that are not exhibited by their linear equivalents. These properties include the ability to bind certain targets more selectively due to their cyclic structures.<sup>19</sup> Furthermore, this oftentimes improves cell permeability and stability under proteolytic conditions thus resulting in improved bioavailability.<sup>20</sup>

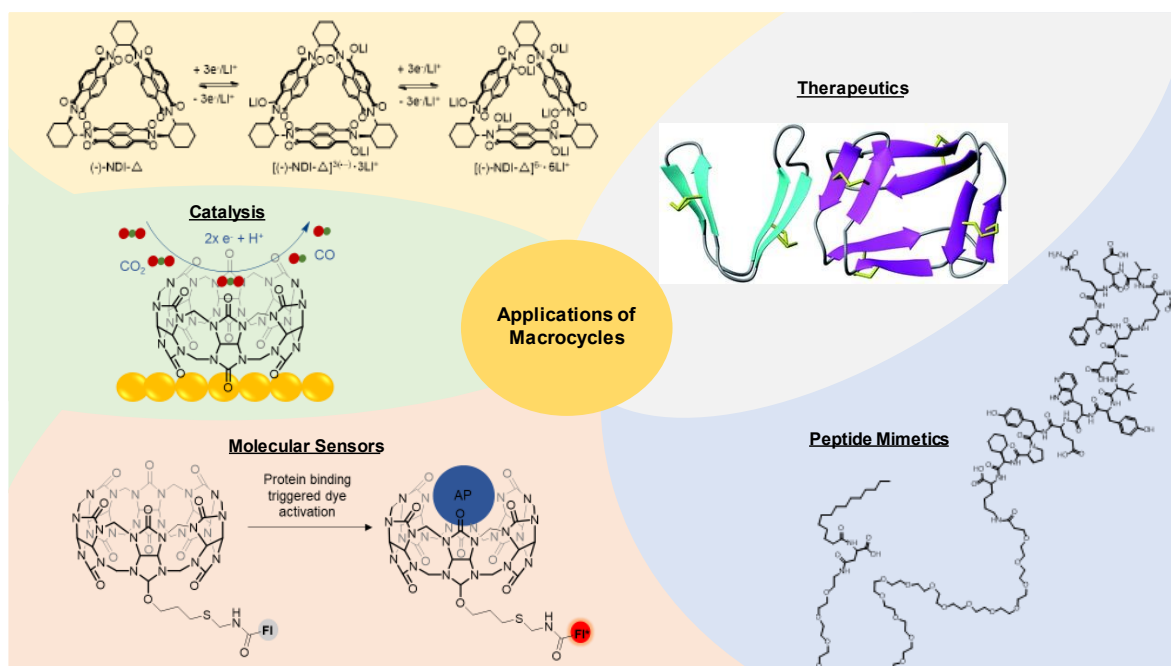
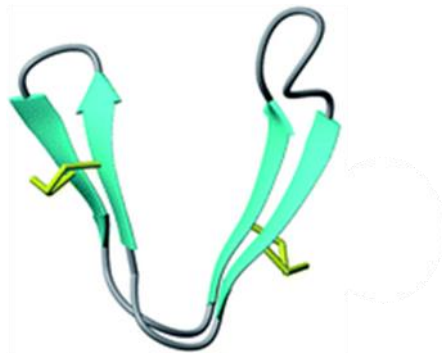


Figure 1. Examples of applications of macrocycles.

Many natural products with useful bioactivity include macrocycles and medium-sized rings. Recently, a macrocyclic peptide, compound **1.1** (represented in a simplified form in Figure 2), discovered in *Zinnia elegans* seeds was synthesised for use as a drug candidate.<sup>20</sup> It was demonstrated that in conjugation with the chemotherapy drug Daunorubicin, compound **1.1** was able to specifically target cancer cell lines that were characteristically overexpressing the multidrug exporter P-gp. Compound **1.1** was resistant to proteolysis, as is characteristic of peptides with disulfide-rich character, and exhibited chameleonic traits which allowed it to efficiently permeate cells and adapt to different environments. This allowed it to act as a small molecule carrier and permeate cancer cell lines, delivering Daunorubicin directly. Manipulation of chain lengths and tertiary structure offers an opportunity for application in small molecule carriers for multiple drug targets, further demonstrating the possibilities for use of macrocycles in therapeutic peptides. Despite their frequency in natural products and their demonstrated use in therapeutics, examples of macrocycles, and particularly, medium-sized rings in drug-screening libraries are lacking, and therefore examples in which these synthetic large rings have been investigated for pharmaceutical use are relatively rare. This is likely due to the challenges associated with synthesising these rings, a topic that will be addressed later.



1.1

*Figure 2. The drug candidate compound 1.1, a macrocyclic peptide first isolated from Zinnia elegans seeds. Compound 1.1 has attractive traits such as proteolysis resistance and the ability to permeate cells. These and others have allowed it to act as a small molecule character to carry the drug Daunorubicin directly to cancer cell lines. Image reproduced from article by Payne et al.,<sup>20</sup> no permissions required.*

Synthetic macrocycles containing nitrogen are also of pharmaceutical interest for their use as peptide mimetics as they can display similar binding properties to naturally occurring proteins such as membrane ion channels or enzymes and can stabilise peptide motifs.<sup>7,8,21</sup> They can also be used as macrocyclic peptide drug candidates, such as compound **1.2** (Figure 3) which is being examined for its use in the treatment of the autoimmune disorder, generalised myasthenia gravis.<sup>13</sup>

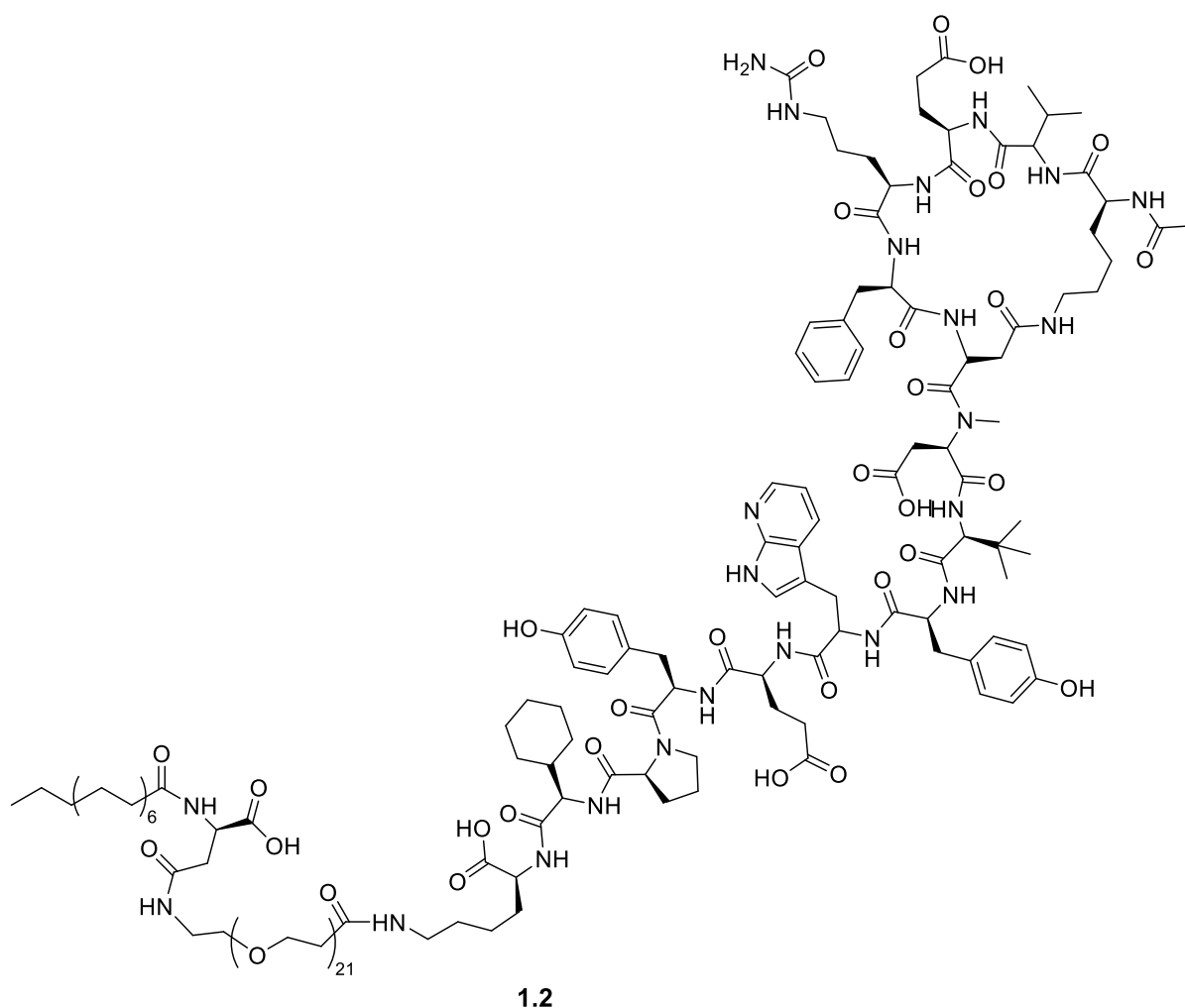
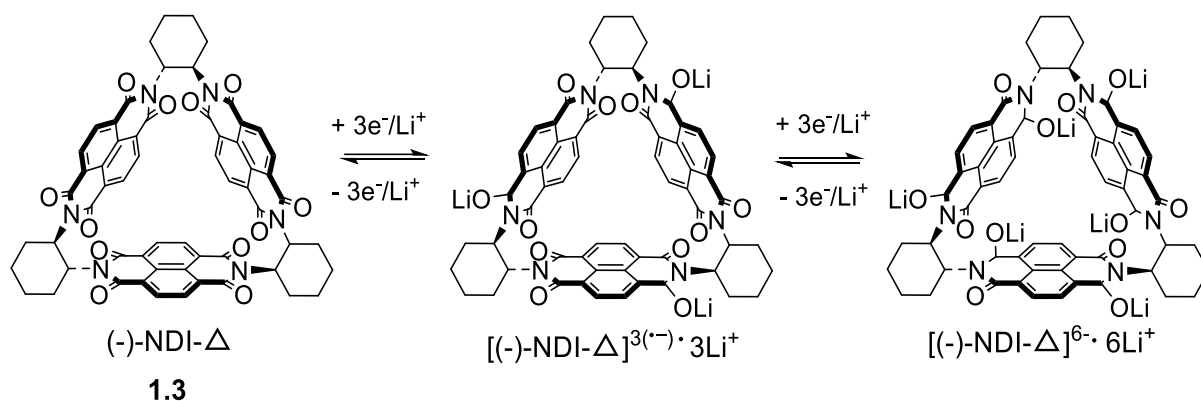


Figure 3. Macrocyclic drug candidate compound **1.2**, which is currently in clinical trials for treatment of the autoimmune disorder, generalized myasthenia gravis<sup>22</sup>

Macrocycles have also been explored for use in molecular electronics to be used for alternative energy storage techniques and as cathodes. The Stoddart group took advantage of the unique features that come with macrocyclisation by oligermisation of naphthalenediimide (NDI) units to form (-)-NDI- $\Delta$  triangles e.g. compound **1.3** (Figure 4). The structure of this triangle was found to be key to improving its performance for use in organic rechargeable lithium-ion batteries. Macrocyclisation allowed overlap of  $\pi$ -orbitals which was demonstrated to facilitate through-space electron delocalisation,<sup>23</sup> enabling compound **1.3** to store up to six electrons. The electron deficient triangles are also able to undergo host-guest interactions to bind  $I^3^-$  anions, through anion- $\pi$  interactions, which in turn, induces a  $\pi$ - $\pi$  stacking interaction between triangles that was not observed in the absence of the  $I^3^-$  anions.<sup>24</sup> Furthermore, testing their potential as lithium ion batteries, the rigidity and nanoporosity of compound **1.3** increased  $Li^+$  ion diffusion through channels at rates of up to four times that of a singular NDI unit. Finally, cyclisation of NDI units to form compound **1.3** resulted in reduced solubility in electrolyte solutions, which increased columbic capacity, resulting in an ultrahigh

performance rate, retaining its 1 C discharge capacity of up to 45 % when a current of 100 C was applied. This was not only far higher than the monomeric NDI, but it also significantly outperformed any organic cathodes that had been investigated at the time.



*Figure 4. The sequential reduction of compound 1.3 and binding of lithium ions, facilitated by through-space electron delocalisation.*

Macrocycles have also been linked to increased conductance in aromatic systems, which could be of use in molecular electronics or photovoltaics. For example, it has been demonstrated that in  $\pi$ -conjugated oligo-(para)phenylene systems, cyclic structures display a lower oxidation potential than their linear analogues, particularly for smaller systems (< 7 phenylene units).<sup>25</sup> This is partly due to a quinoidal distortion, which results in a greater stabilisation of the ring caused by structural reorganisation (Figure 5).<sup>25</sup> A further predicted advantage results from even hole distribution in rings with >7 atoms, meaning medium sized rings are even more likely to benefit from lower oxidation potentials.<sup>8</sup> Since lower oxidation potentials lend themselves to increased conductance in aromatic systems,<sup>14</sup> it is very possible that cyclic systems could serve as more efficient molecular wires. Despite this, there are very few examples of cyclic molecular wires being explored in the literature, representing a promising opportunity for investigation.

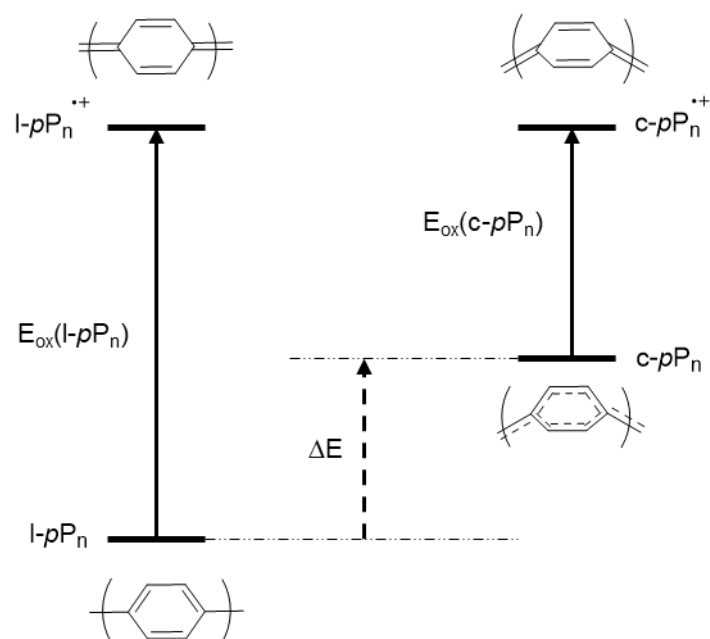


Figure 5. Differences in oxidation potential between cyclic (*c-pPn*) and linear (*l-pPn*) *p*-phenylene polymers. Quinoidal distortion caused by structural reorganisation in *l-pPn* is illustrated.

Electronic applications of macrocycles also extend to insulation of molecular wires to prevent charge transfer between adjacent molecular wires. Recently Sugiyasu *et al.*,<sup>14</sup> was able to demonstrate how an interlocked molecular wire, compound **1.4**, (Figure 6) had improved intrinsic hole mobility due to shielding by the surrounding macrocycle. This interlocked macrocycle-molecular wire could therefore have applications in molecular electronics such as anisotropic conductive materials.

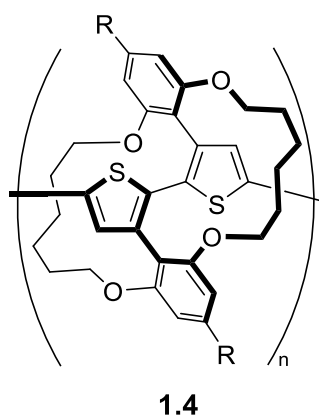
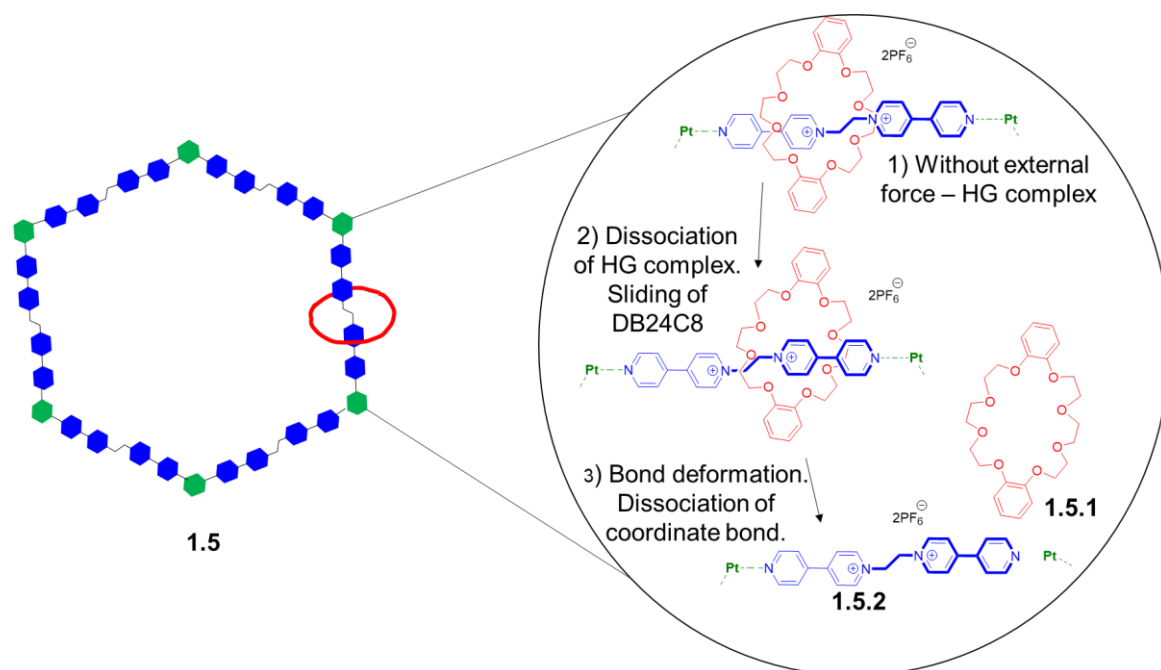


Figure 6. Monomer of a self-insulating interlocked molecular wire, **1.4**, synthesised by Sugiyasu *et al.*,<sup>14</sup>

Interlocked materials are another large area of macrocyclic chemistry and include other applications such as electrocatalysis, metal-organic frameworks and asymmetric catalysis.<sup>26–28</sup> One of the more intricate examples includes that of molecular ‘necklaces’, which are large macrocycles threaded through a number of smaller rings. These include those demonstrated

by Yan's group (Figure 7).<sup>29</sup> Yan's example, complex **1.5**, implemented extra stabilisation through supramolecular interactions cross-linking via host-guest interactions within the necklace and, in particular, metal-coordination, resulting in a molecule with improved mechanical properties such as higher toughness and tensile strength. Furthermore, the necklace demonstrated dynamic adaptability to external stimuli such as  $K^+$  and  $Br^-$  in four stages, namely; 1) dissociation of host-guest recognition; 2) sliding of smaller macrocycle, **1.5.1** along the bis(pyridinium) ligand, **1.5.2**; 3) bond deformation and finally; 4) metal-coordination dissociation. Efficient dissipation of energy associated with this adaptive dynamic behaviour is another advantageous property of the molecular necklace. Due to its various benefits complex **1.5** is attractive for applications in development of sturdy and intelligent molecular materials.



*Figure 7. Mechanical properties and structure of molecular necklace, **1.5**. Shifting pattern of **1.5.1** (red) can be split into 1) dissociation of host-guest recognition; 2) sliding of the **1.5.1** units along the bis(pyridinium) ligand; 3) bond deformation and finally; 4) metal-coordination dissociation. HG = host-guest complex.*

Due to their cyclic structure, macrocycles are often able to accept molecules into their pores which points towards potentially powerful applications in host-guest chemistry. This year (2022), host-guest chemistry was shown to have a possible application in thermally activated delayed fluorescence (TADF) materials by Chen's group.<sup>30</sup> TADF materials are often made from intramolecular charge-transfer systems since these are able to access a small singlet-triplet energy gap, however these often require challenging syntheses. The group demonstrated that more facile a synthesis of TADF systems could be accessed by use of host-guest chemistry to modify photophysical properties and improve the special arrangement of

the donor-acceptor system, resulting in improved charge-transfer states for photoluminescence. Use of a novel host macrocycle **1.6** as the donor and compound **1.7**, (known for its electron-withdrawing nature) as the guest the group were able to syntheses co-crystals with altered fluorescence spectra from the individual molecules (Figure 8). They were able to achieve the highest photoluminescence quantum yield for intramolecular donor-acceptor systems recorded at this time, due to the spatial separation between HOMO and LUMO energy levels resulting in a smaller singlet-triplet charge transfer gap.

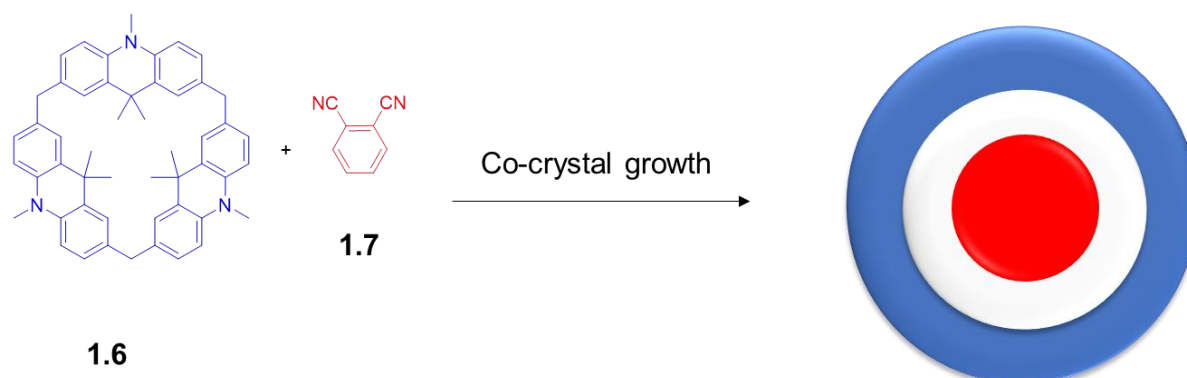


*Figure 8. Synthesis of TADF co-crystals via host-guest chemistry.*

More commonly, host-guest chemistry has been investigated for catalysis. This includes the use of macrocycles with hydrogen-bond donor ability to accelerate Diels-Alder reactions with high selectivity.<sup>22,23</sup>In 2020 it was demonstrated that the compound **1.8** could be adsorbed onto a gold electrode to improve the efficiency of electrocatalytic CO<sub>2</sub> reduction (figure 9).<sup>33</sup> Due to its 'barrel' shape, compound **1.8** is able to incorporate a CO<sub>2</sub> molecule into its central void with a higher affinity than the reduction by-product CO. This, along with near optimal hexagonal packing on the electrode surface enables compound **1.8** to raise the concentration of CO<sub>2</sub> on the surface of the electrode, which could result in improved efficiency and selectivity for the CO<sub>2</sub> reduction. However, improvement of compound **1.8**'s ability to stabilise reaction intermediates could be made. Properties such as a hydrophobic core, which excluded water molecules and electrostatic interactions caused by the carbonyl groups likely prevents stabilisation of the charged intermediate. It was suggested that tuning of functional groups in the active site cavity could allow for modified behaviour to enable the stabilisation of the intermediate.

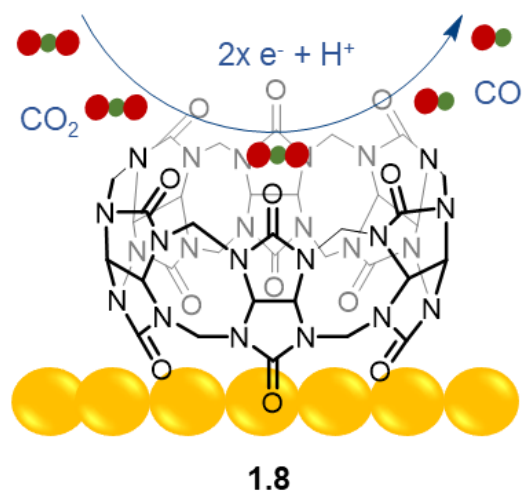


Figure 9. Diagram of how curubit[n]uril, **1.8**, facilitates the electrocatalysis of CO<sub>2</sub>. Yellow = gold electrode, red = oxygen, green = carbon.

Macrocycles have also seen applications in molecular sensing.<sup>34</sup> In this elegant study by Saha *et al.*,<sup>35</sup> Compound **1.9**, the macrocycle cucurbit[7]uril bound to different fluorescent dyes is used as a probe for misfolded proteins through host-guest interactions (Figure 10). Often, misfolded protein accumulation can be hallmarks for disease progression and significantly in some cases, such as that of Alzheimer's they can be an early indicator of onset and their identification could lead to earlier treatment, which can be incredibly important in stemming disease progression. Saha *et al.*, were able to demonstrate that in conjugation with different dyes, **1.9** could use host-guest chemistry to specifically identify a range of different proteins via alteration of the fluorescence fingerprint of the dyes. This variation in fluorescence could be detected and specific proteins could be identified using machine learning. It was shown that **1.9** was vital to the detection mechanism as encapsulation of the misfolded protein guest molecule by host **1.9** via specific interactions of **1.9** with the protein surface, allowed the fluorescent dyes to be brought into close proximity of the protein, triggering fluorescence. When a negative **1.9** control was used, no fluorescence was observed. Impressively, this probing system was seen to be able to discriminate between protein aggregates which are early markers of Alzheimer's disease from the normal, healthy proteins with similar folding with 100 % accuracy. This demonstrates an incredibly sensitive system for application in diagnosis of Alzheimer's disease.

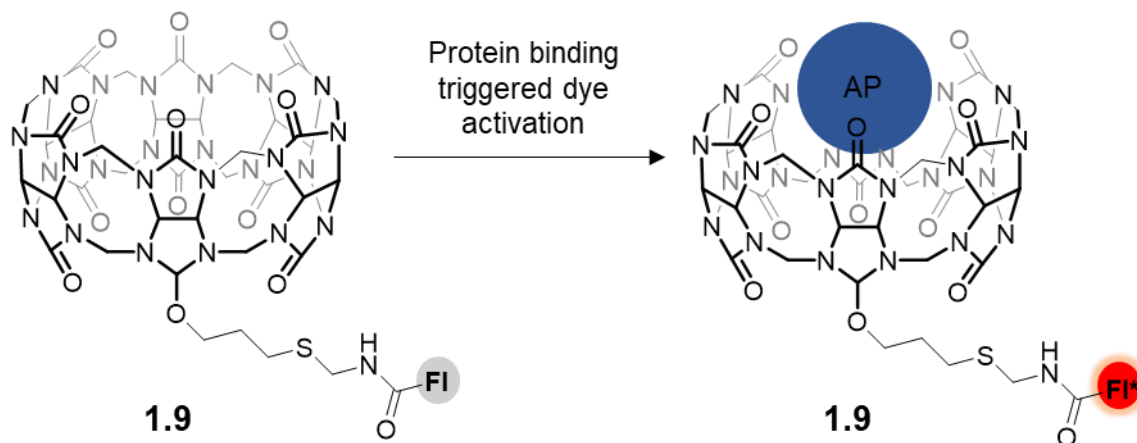


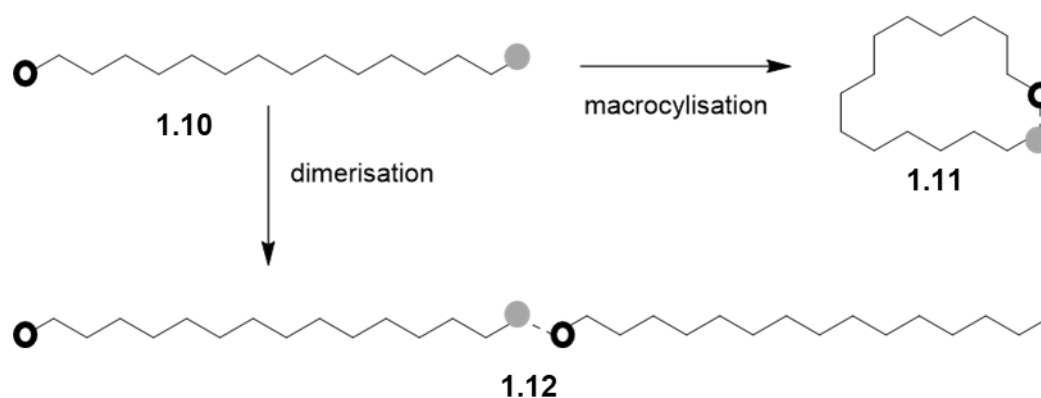
Figure 10. Host-guest interaction of Alzheimer's protein markers with compound **1.9**, resulting in \*activation of the dye and detection of a fluorescent signal.

It is clear that macrocycles have unique properties which are important for investigation towards applications such as molecular electronics, molecular sensing,<sup>35</sup> catalysis,<sup>22–24</sup> therapeutics and peptide mimetics.<sup>13,20,36</sup> However, they are underrepresented in literature due to the challenges associated with their synthesis, particularly when specific functionalisation is required.<sup>37</sup> The challenges and possible solutions associated with macrocyclic synthesis will be discussed in the next section of this chapter.

## 1.2 Synthesis of Macrocycles and Medium-Sized Rings: End-to-End Cyclisation

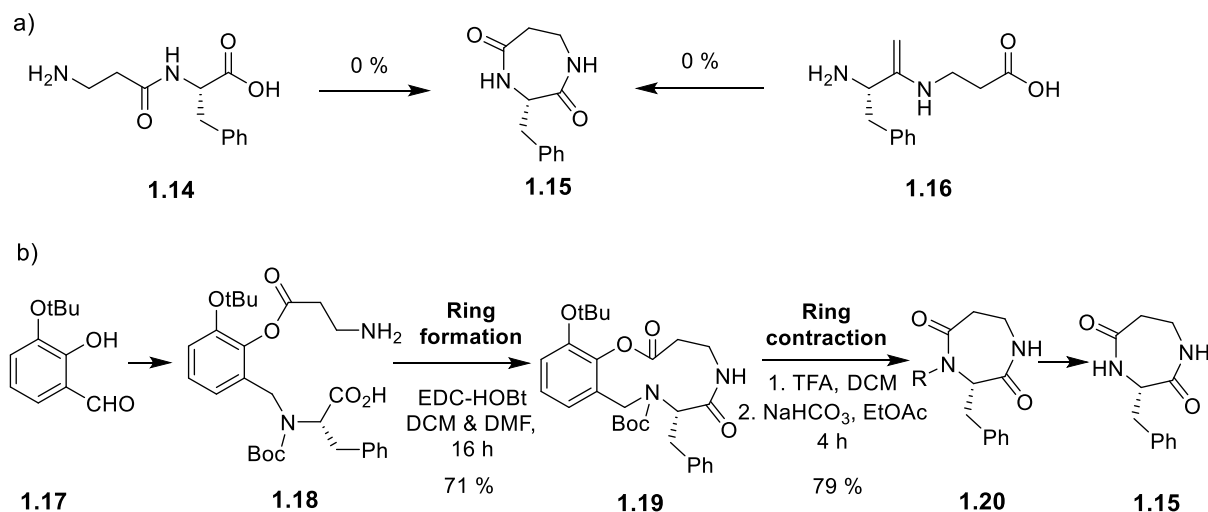
### End-to-End Cyclisation

Despite their potential for use in many different applications, making macrocycles remains a major synthetic challenge, especially on large scale. Commonly, the synthetic method used to form both medium-sized rings and macrocycles of the type **1.11** is via end-to-end cyclisation (Scheme 1), whereby reactive groups at the end of a linear precursor **1.10** react to form a ring. However, these reactions tend to be hindered by competing dimerisation (to form **1.12**) and oligomerisation side reactions. In the case of macrocyclic rings, cyclisation tends to be entropically unfavourable as upon cyclisation, the products suffer from a loss of entropy, due to increased order in the system. Destabilising enthalpic effects such as torsional and ring strain also make cyclisation more challenging, especially for medium-sized rings.<sup>38,39</sup> When making such cyclic products it is therefore important that end-to-end cyclisation occurs more quickly than competing intermolecular side reactions. A common strategy to help promote this is the use of high dilution conditions or pseudo high dilution conditions to limit intermolecular side reactions. However, the outcome is dependent on the substrate and reagents and this approach is usually not viable for scale up.



*Scheme 1. Generalised scheme for cyclisation via reaction of end groups (end-to-end cyclisation) and its competing dimerisation reactions.*

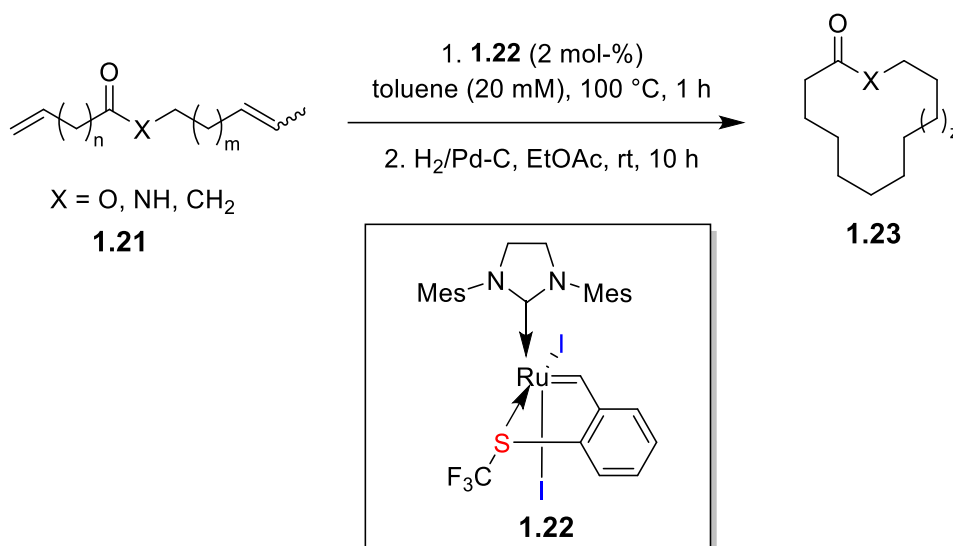
Templation methods can be used to help provide a thermodynamic driving force for the formation of macrocycles and medium sized rings (Scheme 2). For example, Bieräugel *et al.*,<sup>40</sup> were able to demonstrate how the yields of lactamisation reactions could be increased by use of tethered-templated approaches to provide the thermodynamic driving force for ring-contraction. Attachment of a linear precursor to auxiliary **1.17** brought reactive functional groups together to first form larger ring, **1.19**. This was followed by protecting group (PG) cleavage, triggering ring-contraction with the removal of the auxiliary (Scheme 2b). This method allowed compound **1.15** to be formed in 65 % yield, which represented a great improvement from direct cyclisation from precursors **1.14** and **1.16** which resulted in 0 % product formation (Scheme 2a).



*Scheme 2. a) direct cyclisation attempt to synthesis compound 1.15. b) Synthesis of compound 1.15 using tethering approach followed by ring contraction.*

Ring-closing metathesis (RCM) is also a common method used for end-to-end macrocyclisation. RCM makes use of metal catalysts (usually a ruthenium carbenoid) to

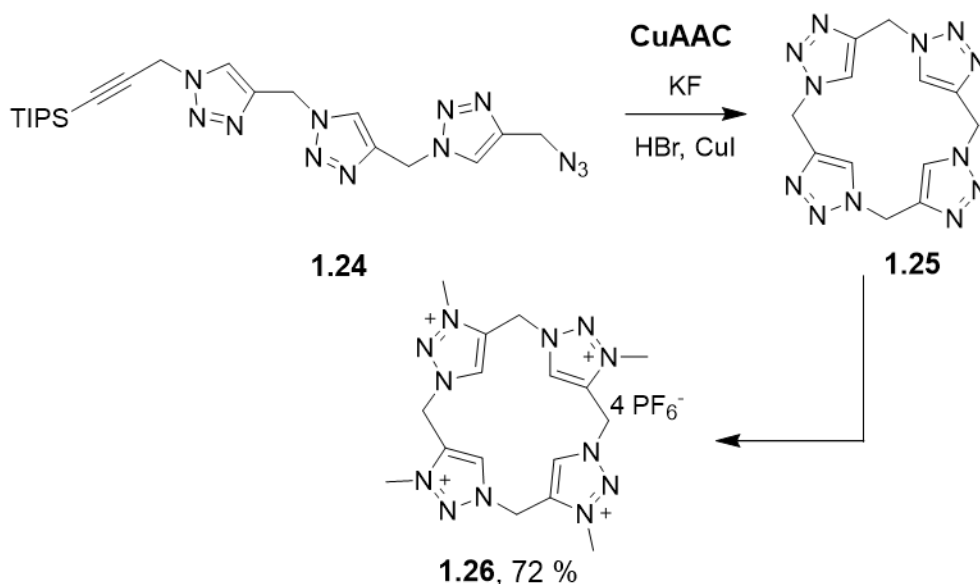
promote C-C bond formation from diene precursors. Recently, Ravindra *et al.*,<sup>41</sup> demonstrated the versatility of RCM reactions in the formation of macrocyclic lactams and lactones e.g. **1.23**, by using a selective latent ruthenium sulfur-chelated catalyst, **1.22**, activated either thermally or photochemically (Scheme 3). This method restricted side-reactions which can occur when reacting internal olefins, while still promoting high yields.



*Scheme 3. RCM of diene precursors.*

The use of preorganisation can also allow for a thermodynamic driving force by creating a conformational bias to favour cyclisation. This can be done internally e.g. by inclusion of a *cis* or *trans* bond to promote functional group proximity; or externally e.g. by using molecular scaffolds or coordination to bring reacting functional groups into close proximity.<sup>42</sup>

For example, in a paper published in August 2022, Zámbo *et al.*,<sup>43</sup> described the synthesis of the iron-coordinating ligand **1.26** through use of a CuI-catalyzed azide/alkyne cycloaddition (CuAAC). The high yields of 72 % was likely aided by the cyclisation geometry imposed by the multiple sp<sup>2</sup> centres in the linear precursor, as well as use of efficient CuAAC reactions in both the synthesis of the linear precursor **1.24** and the macrocyclization step. CuAAC is a popular ‘click chemistry’ method in which coordination of a Cu<sup>I</sup> catalyst to an alkyne functional group on the target molecule lowers its pK<sub>a</sub>, and also promotes cyclisation by azide coordination to the Cu centre, thus bringing the reactive groups into closer proximity.<sup>44</sup> Zámbo’s use of the CuAAC click reaction demonstrated its applicability to improve the yield of end-to-end cyclisation reactions and limited the occurrence of side reactions.



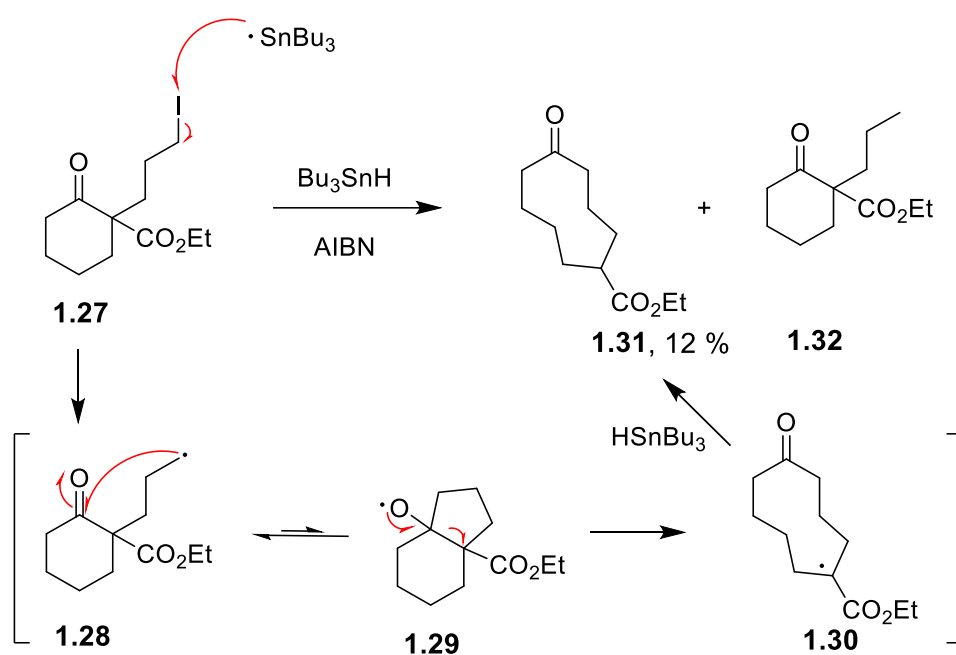
Scheme 4. CuAAC click reaction to form a macrocyclic precursor for the synthesis of ligand **1.26** in 72 % yield. TIPS = Triisopropylsilyl ether.

### 1.3 Synthesis of Macrocycles and Medium-sized Rings: Ring Expansions

Alternatively, expansion of pre-existing rings can provide favourable alternatives to end-to-end cyclisation. Ring expansion methods often remove the problem of side-product formation by dimerisation. However, expansion from normal into larger medium-sized or macrocyclic ring systems generally results in an increase in strain in the ring, requiring ring expansion reactions to have another thermodynamic driving force to overcome this. The different types of ring-expansion reactions have been comprehensively reviewed,<sup>10</sup> with selected highlights covered in the following section.

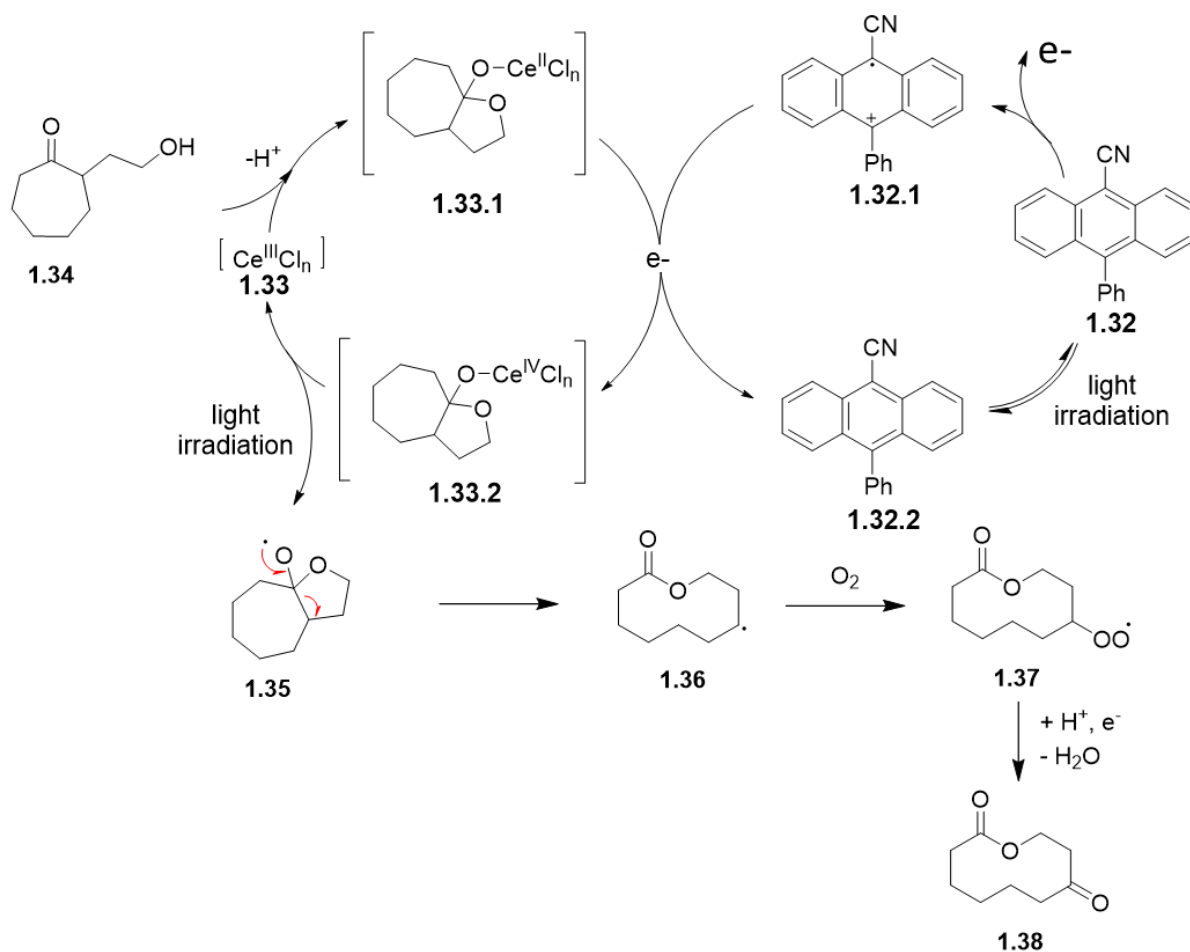
#### Radicals

One way in which a thermodynamic driving force can be provided for ring expansion is through stabilisation of radical intermediates. One of the more robust strategies includes the Dowd-Beckwith reaction for which many similar variations have been undertaken. An illustrative example includes that by the Dowd group (Scheme 5).<sup>45</sup> Here an alkyl radical on the side chain of **1.27** is formed, resulting in reversible cyclisation by radical attack onto the ketone. Ring opening of the bicyclic intermediate, **1.29** to form compound **1.30** provides the thermodynamic driving force for ring expansion due to the additional stability of the radical provided by conjugation with the adjacent ester functional group. The radical is then terminated with  $\text{Bu}_3\text{SnH}$  via C-H abstraction to form compound **1.31** in 12 % yield.



*Scheme 5. Ring expansion via stabilisation of a radical in the intermediate, ring expanded product.*

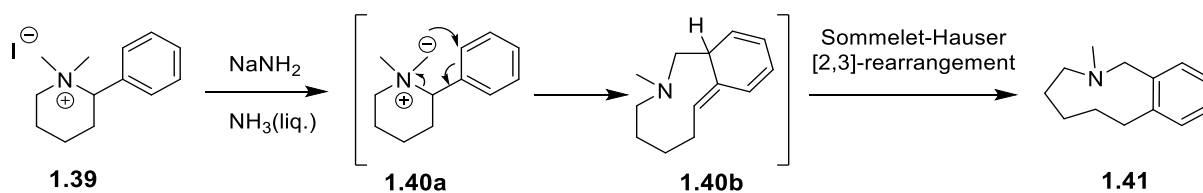
Recent examples of radical ring expansion reactions include the use of electrocatalysis and photocatalysis. In 2021, Du *et al.*,<sup>46</sup> demonstrated the use of the simple photocatalysts **1.32** and **1.33** to promote radical mediated ring expansions to form **1.38** in high yields (Scheme 6). This method demonstrated how mild reactions can be used to form macrocycles without the loss of yield or stereochemistry, to create a diverse library of macrocycles.



Scheme 6. Radical promoted ring opening using photocatalysis.

### Pericyclic Reactions

The most common type of pericyclic ring expansions are those based on sigmatropic rearrangements. These reactions require a driving force such as relief of ring strain for the formation of more stable bonds to prevent an equilibrium between the starting materials and products from forming. Hausner *et al.*,<sup>36</sup> used a Sommelet–Hauser [2,3]-sigmatropic rearrangement to trigger ring expansion to form compound **1.41** (Scheme 7). The reactivity of ylide **1.40a**, formed by deprotonation of **1.39**, followed by re-aromatisation to form **1.41** provided the driving force for ring expansion. The close proximity of the reacting groups allowed for a rapid ring expansion, thus minimising the formation of side-products.



Scheme 7. Ring expansion using Sommelet–Hauser [2,3]-sigmatropic rearrangement

More recently, Manning *et al.*,<sup>47</sup> described the expansion of **1.42** to form **1.45** via a photochemically induced [1,3]-sigmatropic rearrangement (Figure 11). The driving force for this rearrangement was triggered by the relaxation of the singlet state, **1.42\*** formed by photochemical excitation, into the rearrangement product **1.43**. This was followed by a [1,5]-sigmatropic H-shift to form **1.45**. These reactions allowed synthesis of a class of nitrogen heterocycles which were previously challenging to access.

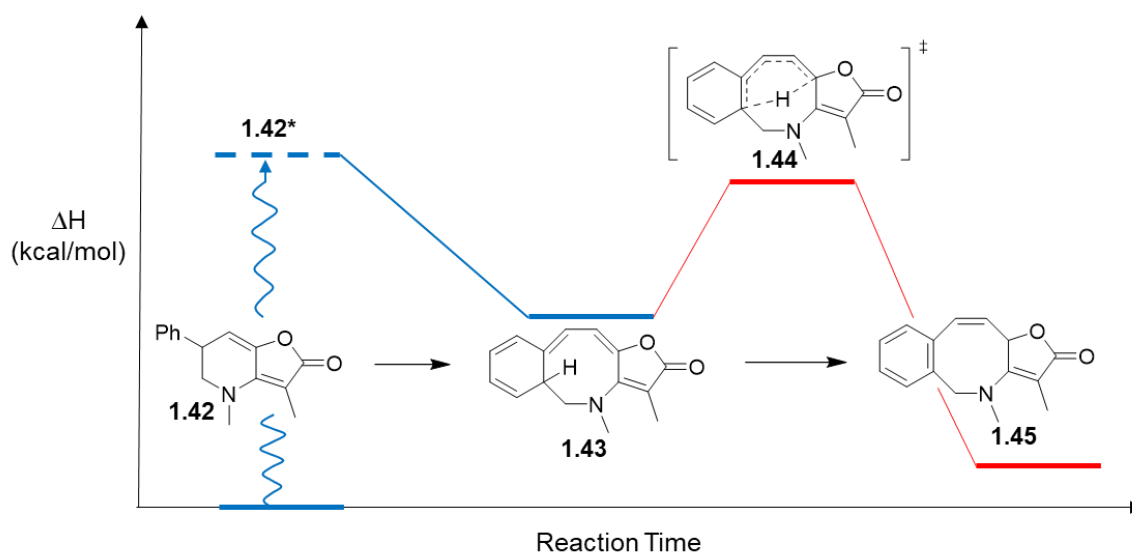


Figure 11. Formation of compound **1.45** via photochemical rearrangement (blue) followed by the thermal [1,5]-sigmatropic H-shift (red).

### Fragmentations

Fragmentations involve the cleavage of a central bond in a bicyclic system to create a larger ring. This can either be 1) *via* the cleavage of a bond in a pre-existing fused bicyclic system; or, 2) through the formation of a transient bicyclic species up on side chain attack, before ring expansion a.k.a. side chain insertion (Figure 12). Reactions with bicyclic systems as a starting material or as an intermediate, can enable the kinetic barrier to cyclisation to be lowered as higher energy medium-sized ring transition states are by-passed, resulting in a more kinetically favourable reaction.

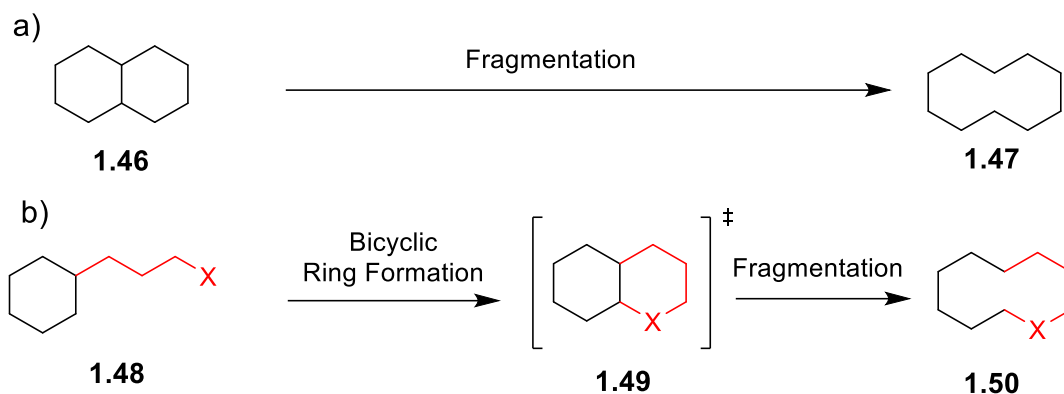
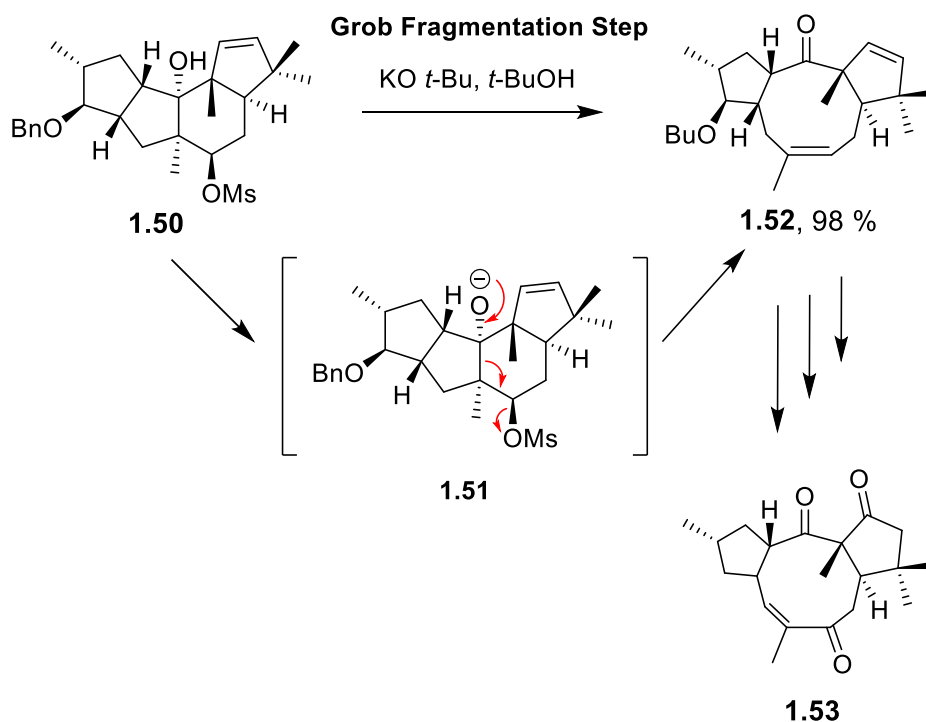


Figure 12. Ring expansion via bicyclic rings. a) from a bicyclic starting material; b) via a bicyclic intermediate.

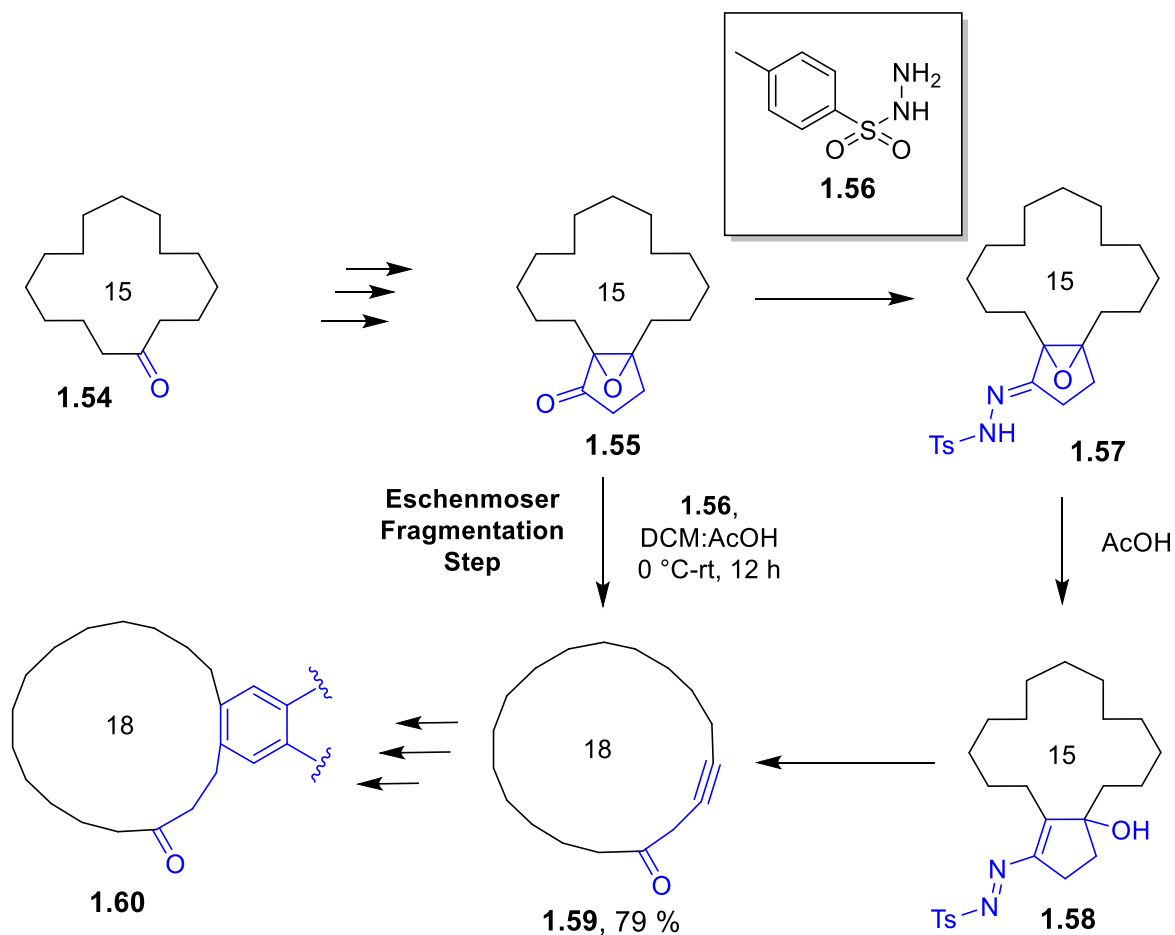
#### a) Fragmentation of Fused Bicyclic Rings

A common example of fused bicyclic cleavage would be Grob fragmentation. This involves the pushing of electrons through four bonds by an electron donating group towards the leaving group, resulting in C-C bond cleavage and the expulsion of the leaving group. Grob fragmentation is commonly used in natural product synthesis for medium-sized ring targets. An illustrative example published by Paquette *et al.*,<sup>48</sup> was included in their total synthesis of the antileukemia agent Jatropha-trione (Scheme 8; compound **1.53**). Here, the fragmentation requires the deprotonation of the sterically hindered hydroxyl group to form intermediate **1.51** which initiates bond cleavage, resulting in extrusion of the mesylate leaving group. This two-step synthesis resulted in a 98 % yield of Jatropha-trione precursor **1.52**.



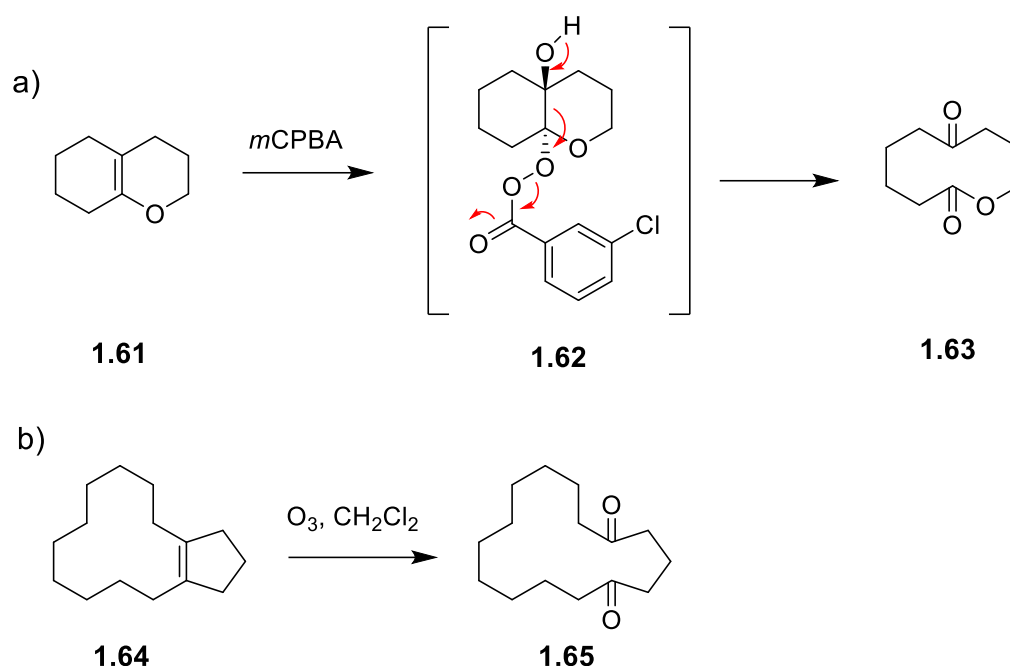
Scheme 8. Ring expansion via Grob fragmentation to form Jatropha-trione.

A similar fragmentation mechanism includes Eschenmoser fragmentation.<sup>49</sup> An example includes the ring expansion step in the total synthesis of various macrocyclic ring for use as musk analogues by Kotha's group (scheme 9).<sup>50</sup> Here, compound **1.56** attacks the ketone on the 15-membered macrocycle **1.55**, forming intermediate **1.57**. Addition of acid results in intermediate **1.58** which rearranges to form the 18-membered ring expanded precursor **1.59**. Compound **1.59** was later taken forward to synthesis musk analogue **1.60**.



*Scheme 9. Ring expansion using Eschenmoser fragmentation in the formation of musk analogues. Ts = tosyl.*

Other examples of this type of fragmentation can include redox-mediated oxidations that can be used to trigger Grob/Eschenmoser-type fragmentation *in situ* (Scheme 10a; **1.61**→**1.63**) or via alkene-cleaving reactions such as ozonolysis (Scheme 10b; **1.64**→**1.65**).<sup>51,52</sup>

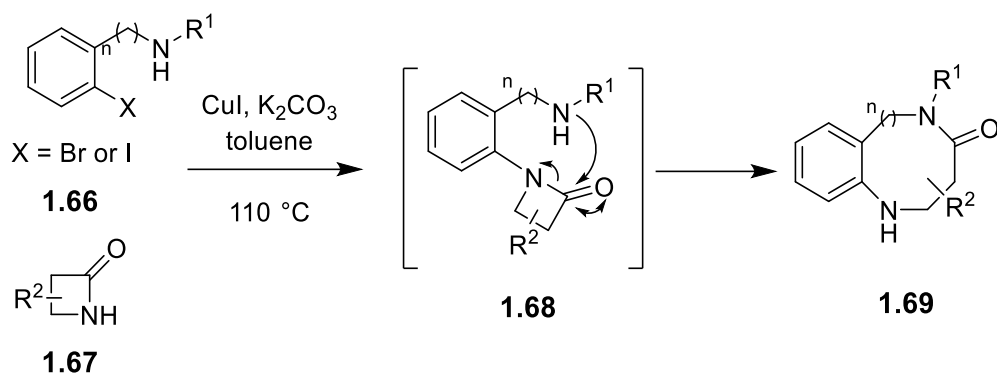


Scheme 10. Ring expansion techniques using redox-mediated oxidations. a) *in situ* initiation of Grob/Eschenmoser-type fragmentation b) ozonolysis

#### b) Side-chain insertion

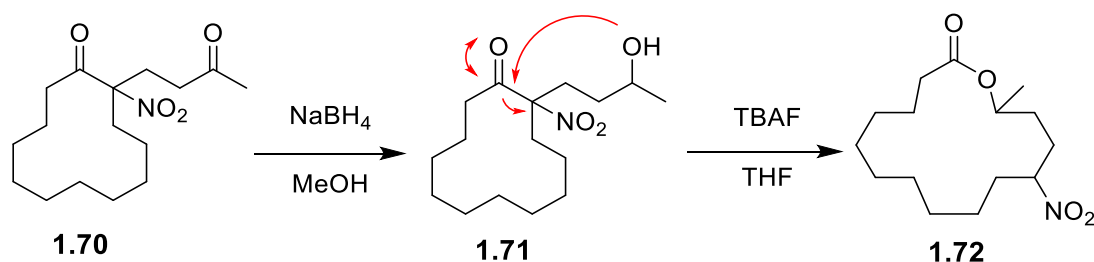
The second form of bicyclic system involves the bicyclic system as a transient intermediate in a side chain insertion, which is shortly followed by ring expansion to form new C-O, C-N or C-C bonds. Like previous examples side-chain insertion often requires a strong driving force to prevent an equilibrium forming between the expanded product and the side chain/bicyclic components. This can include techniques such as relief of ring strain,<sup>53</sup> promotion of the fragmentation step by the inclusion of electron withdrawing or donating groups,<sup>54</sup> or the formation (or reformation) of stabilised functional groups like amides or aromatic products, to enable the expanded ring to be favoured.<sup>55,56</sup>

The use of ring strain relief can be illustrated by the method developed by Buchwald *et al.*,<sup>53</sup> (Scheme 11) who utilised the insertion of side chain **1.66** into highly strained 4-membered  $\beta$ -lactam ring, **1.67** by heating with a copper(I) catalyst to form a new C-N bond in intermediate **1.68**. Ring strain relief associated with the formation of the medium-sized product, **1.69**, acted as the thermodynamic driving force for this reaction to result in the synthesis of **1.69** in high yields.



Scheme 11. Ring expansion via side chain insertion, promoted by ring-strain relief.

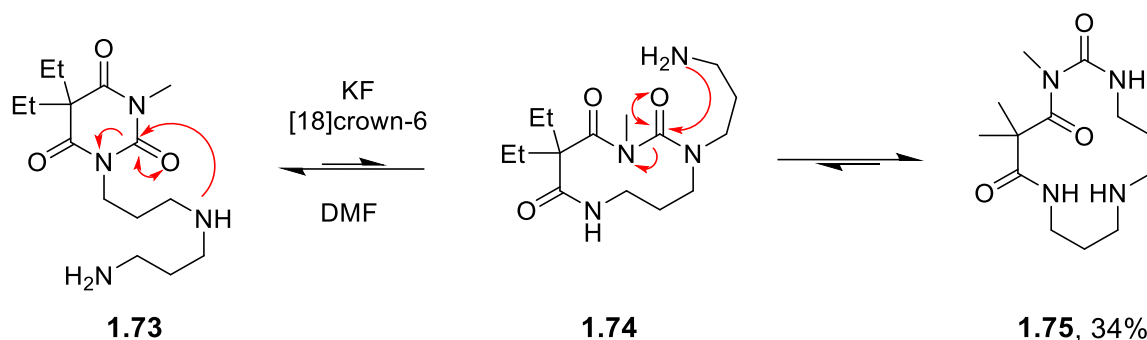
Many other examples include those developed by Hesse's group, who played a very important role in the development of ring expansion by side chain insertion chemistry throughout his career. One such example, illustrated in Scheme 12, includes the utilisation of a nitro electron withdrawing group in the cyclic precursor **1.70** to promote fragmentation and allow the formation of the intended macrolactone **1.72**.<sup>54</sup>



Scheme 12. Ring expansion via side chain insertion promoted by an electron-withdrawing nitro group. TBAF = Tetra-*n*-butylammonium fluoride.

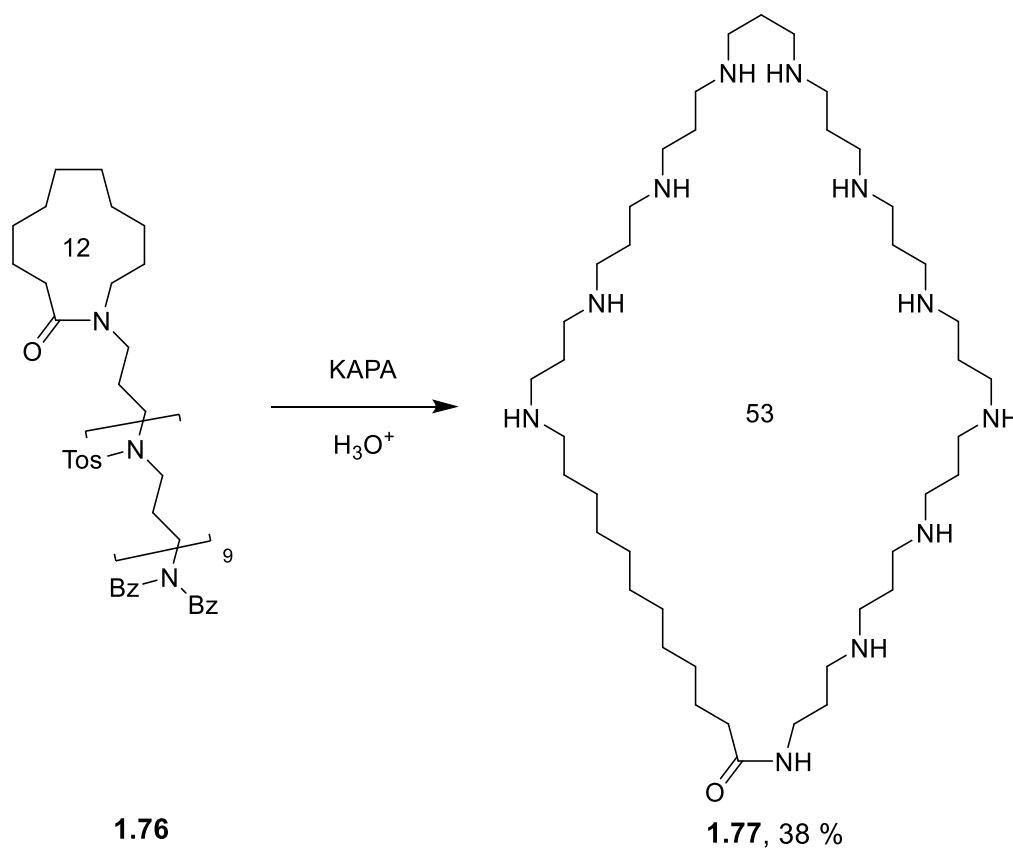
### Consecutive Ring Expansions

Side-chain ring expansion can also be achieved iteratively. For example, Hesse's group developed a group of reactions called "zip reactions" which involved the expansion of 6-membered ring **1.73**, first to an unstable 10-membered intermediate **1.74**, then upon a second expansion into a 14-membered product, resulting in an equilibrium between all three rings and allowing the 14-membered ring **1.75** in 34 % yield (Scheme 13).<sup>57</sup> Iterative ring expansions are advantageous as they allow specific functionalisation to be installed at different points in the ring. They also take advantage of the release of strain when moving between a medium-sized ring and a macrocycle.



Scheme 13. 'zip' reaction by Hesse's group via the less energetically 10-membered medium-sized ring, followed by successive expansion to the more stable 14-membered ring.

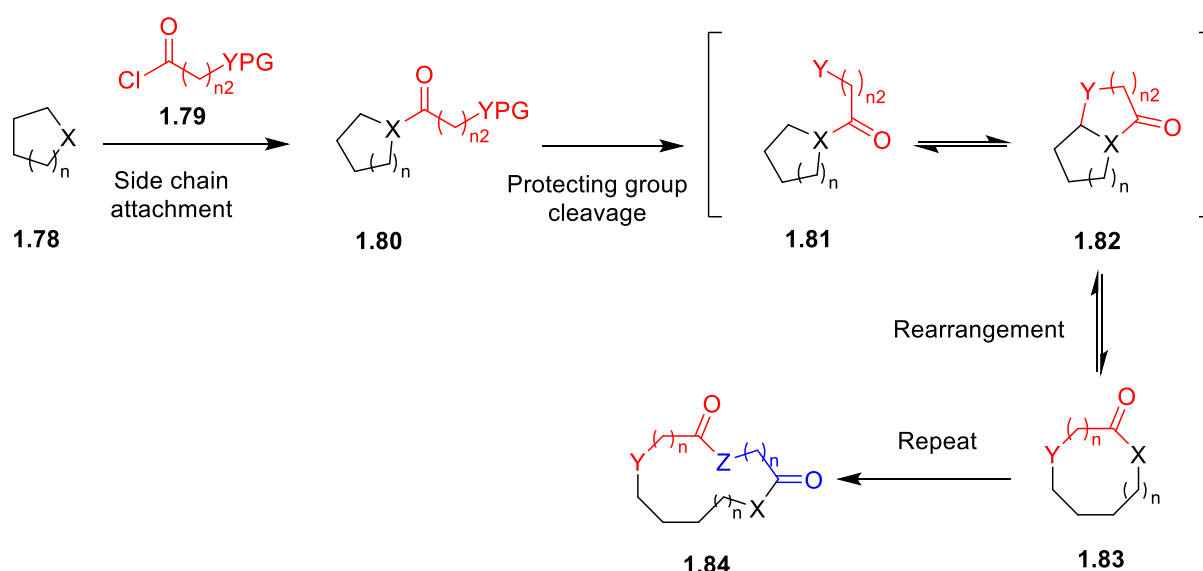
A particularly impressive example of this 'zip' chemistry by Hesse's group is their formation of a 53-membered macrolactam **1.77** from a 12-membered precursor **1.76** resulting in **1.77** in yields of 38 % (Scheme 14).<sup>55</sup> The development of consecutive ring expansions has previously been reviewed.<sup>11</sup>



Scheme 14. 'Zip' reaction by Hesse's group to form a 53-membered ring product from a 12-membered ring product.

#### 1.4 Synthesis of Macrocycles: Successive Ring Expansion (SuRE)

Partly inspired by the examples by Hesse's group explored above, the Unsworth group developed a method which utilises consecutive ring expansion via side chain insertion, coined 'Successive Ring Expansion' or 'SuRE'. In general terms, SuRE, (as summarised in Scheme 15), works by attachment of a side chain via reaction of a cyclic starting material, **1.78** with an acyl chloride, **1.79**, followed by PG cleavage, to form intermediate **1.81** which undergoes nucleophilic attack by Y forming bicyclic intermediate **1.82**, followed by fragmentation resulting in ring expansion to **1.83**. Importantly, SuRE is designed in such a way as to regenerate the original chemical functionality used to promote the reaction, which allows the expansion to be repeated, in theory, indefinitely. This allows the facile synthesis of macrocycles (and sometimes medium-sized rings) via the iterative insertion of different 3- and 4-atom linear fragments.<sup>58</sup> SuRE is able to incorporate a variety of linear fragments and cyclic starting materials, making it a valuable tool for creating a wide variety of macrocycles.



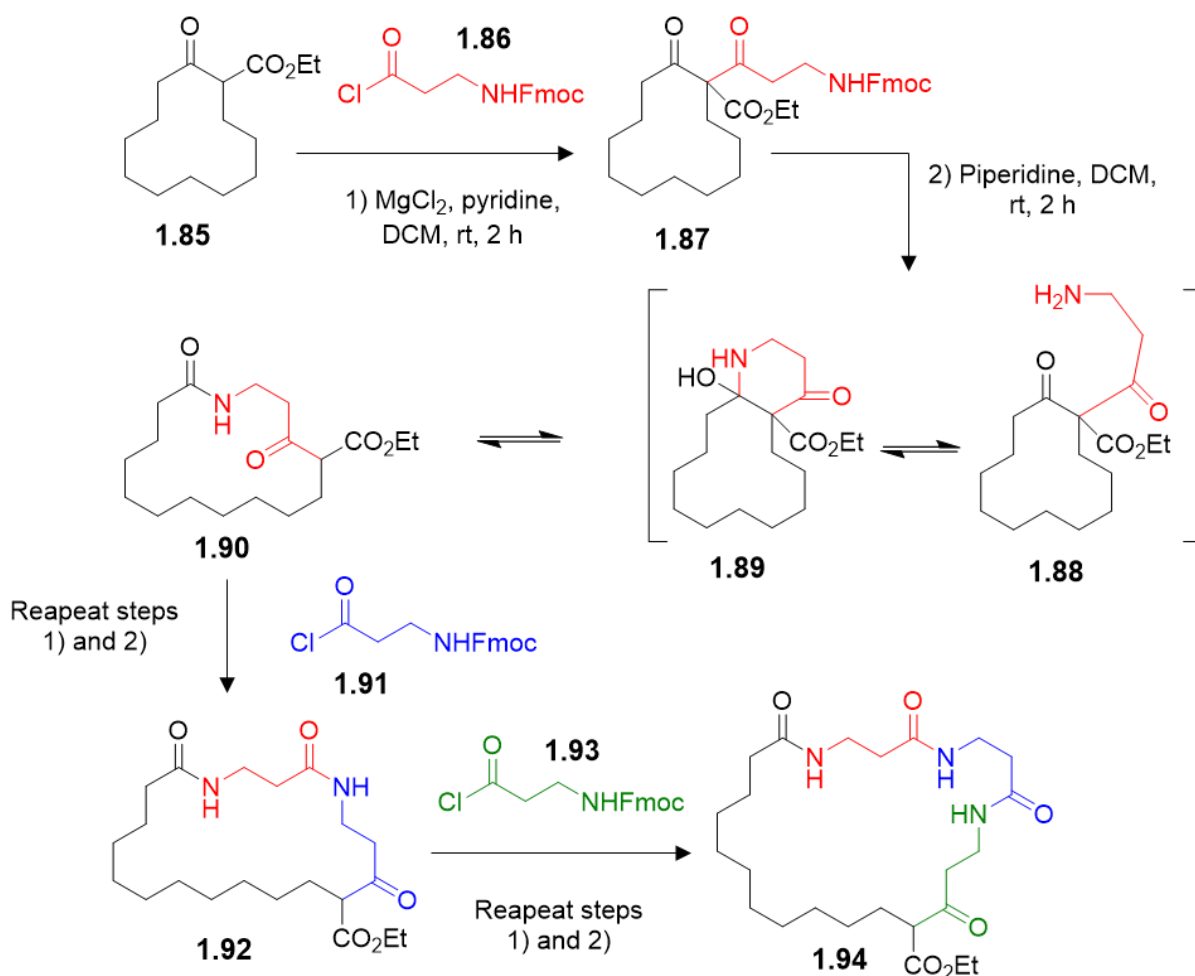
*Scheme 15. General SuRE reaction scheme. X = first functional group; Y = first attacking nucleophile; Z = second attacking nucleophile; PG = Protecting group.*

The rearrangement step of SuRE is thought to be reversible, as illustrated in Scheme 15, and therefore needs a thermodynamic driving force to overcome the barrier associated with the change in ring size. In SuRE this is thought to be provided by the conversion of relatively unstable bonds such as the internal imide C–N bond into more stabilised bonds such as amides or  $\beta$ -ketoesters. However, ring size is still the most important indicator as to whether ring expansion will proceed.

Both synthetic and computational (density functional theory, DFT) investigations have demonstrated that smaller cyclic starting materials are less favourable. This is due to the formation of medium-sized rings which are associated with an increase in torsional and ring strain. Those of less than 6 atoms are less likely to undergo ring expansion. Cyclic starting materials with 6-7 atoms generally require an acyl chloride unit of 4 or more atoms and those

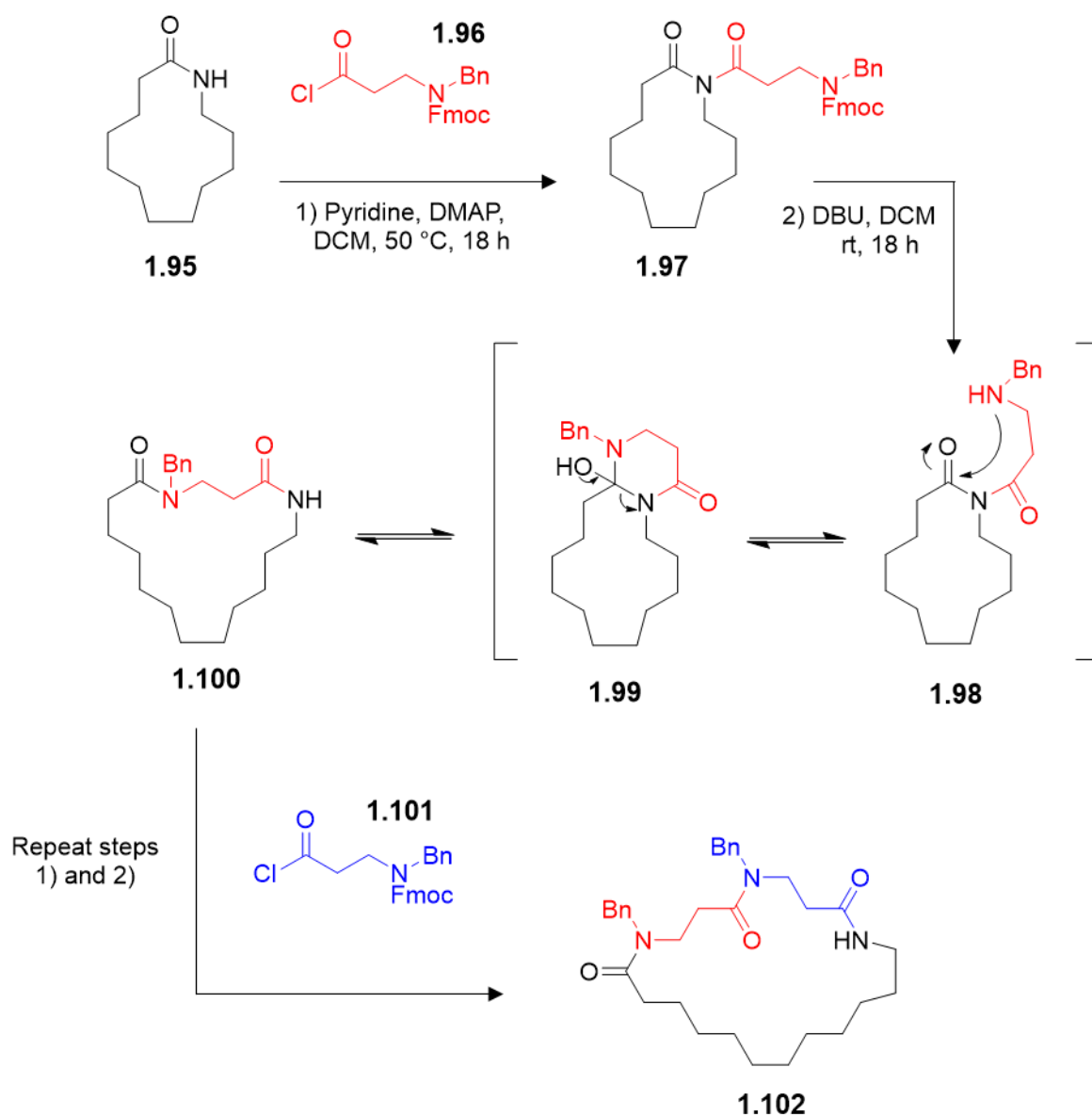
of 8 or more require at least 3-atom-containing acyl chlorides. Calculations, performed using a DFT methodology, are able to effectively estimate the likelihood that a given ring expansion will occur and also predict expansions that are thermodynamically unfavourable.<sup>59</sup> These calculations do not consider the reaction kinetics and the possibility of alternative side reactions, but they are nonetheless a useful predictive tool for reaction viability. The formation of medium-sized rings is particularly challenging due to the combination of both a decrease in entropic factors and an increase in enthalpic factors such as torsional and ring strain.

The original SuRE methodology was developed for use with  $\beta$ -ketoesters (Scheme 16).<sup>58</sup> It was demonstrated that acyl chloride **1.86** undergoes C-acylation at the  $\beta$ -carbon site of **1.85**. Removal of the PG, most commonly fluoromethyloxycarbonyl (Fmoc), allows nucleophilic attack on the ketone. Rearrangement of bicyclic intermediate **1.89** results in the complete insertion of **1.86** into the ring. The driving force behind ring expansion is thought to be the formation of the stabilised enolate and amide groups which favour formation of the macrocyclic product. This study demonstrated the viability of SuRE to include a variety of  $\beta$ -ketoesters, along with different linear fragments which include alcohols and derivatives of both  $\beta$ - and  $\alpha$ -amino acids. Furthermore, the ability of the technique to be repeated successively was demonstrated with linear fragments with varying functionalities. Significantly, the inclusion of  $\alpha$ -amino acids can create peptide-like macrocycles which may have applications in peptide mimetics or in therapeutics which mimic the action of natural products as explored earlier.



*Scheme 16. SuRE with  $\beta$ -ketoesters. Side chain insertion is achieved using  $\text{MgCl}_2$  and pyridine to promote C-acylation, followed by Fmoc deprotection which passes through a bicyclic intermediate to result in ring expansion. Successive expansions occur by repeating steps 1) and 2).*

The use of “metabolically liable”  $\beta$ -ketoester groups is central to this approach. However,  $\beta$ -ketoesters are too reactive/unstable to be present in drugs, meaning that it there is a requirement for its removal by further synthetic steps for the macrocycles to be deemed appropriate for use in pharmaceuticals. Due to this, the Unsworth group demonstrated that lactams (Scheme 17) are also able to be used in SuRE,<sup>60</sup> allowing the replacement of the  $\beta$ -ketoester motif with a more stable amide group.

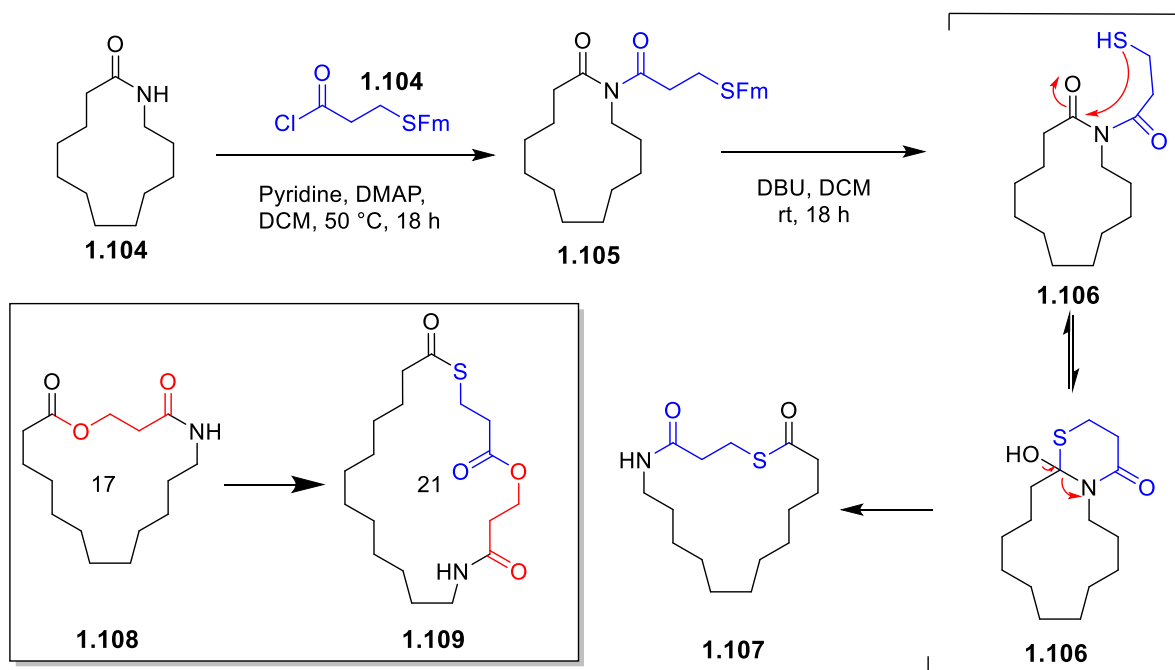


**Scheme 17.** SuRE with  $\beta$ -lactams. Side chain insertion is achieved using DMAP and pyridine to promote N-acylation, followed by Fmoc deprotection which passes through a bicyclic intermediate to result in ring expansion. Successive expansions occur by repeating steps 1) and 2).

This study demonstrated that lactams can be expanded using SuRE resulting in high yields and could also be repeated in succession twice more, also in high yields. The scope was then explored, and it was demonstrated that SuRE with lactams could be undertaken with a range of  $\beta$ -amino acid chlorides, including *N*-methylated species which can improve the characteristics of cyclic peptides for use as drug candidates. Furthermore,  $\alpha$ -amino acids could also be used as an expansion group, with a higher success than the previously explored lactone expansions, resulting in a range of cyclic peptides which have significant medicinal relevance. Optimisation of these  $\alpha$ -amino acid expansions are yet to be undertaken and would be useful if their products were found to have medicinal relevance. Cyclic peptoids, which are

also medicinally relevant could be synthesised using peptoid units in high yields. A separate study by the Unsworth group exploring the drug lead-like behaviour of the SuRE products, and using computational methods they found that the lactam derivatives made have high potential for use as medicinally relevant lead-like molecules.<sup>61</sup> Using *N*-carboxybenzyl (Cbz) protected alcohols in place of Fmoc-protected amines was also shown to allow the generation of a cyclic lactones, which are found in antimicrobial natural products.<sup>58,62</sup>

Finally, SuRE using lactams has been extended further to include the synthesis of thiolactone Scheme 18.<sup>63</sup> Thioesters are of high interest due to their abundance in biosynthetic pathways,<sup>64</sup> their ability to ring open upon addition of water is beneficial for use as prodrugs, or for use in polymer science.<sup>65</sup> Despite this, there are limited examples of the synthesis of thiolactone in the literature. The thioester group is less stable than a lactam or lactone, and hence provides a smaller thermodynamic driving force than the previous amide and  $\beta$ -ketoester SuRE methods. This was reflected in the DFT calculations. Despite this, optimisation of the conditions for SuRE allowed the synthesis of a variety of larger rings, although the process suffered from deleterious side reactions resulting in lower yields. This study also showed the ability of SuRE to functionalise rings in a variety of ways as demonstrated by the synthesis of compound **1.109**, a macrocycle which incorporated a lactam, lactone and a thiolactone as functional groups.

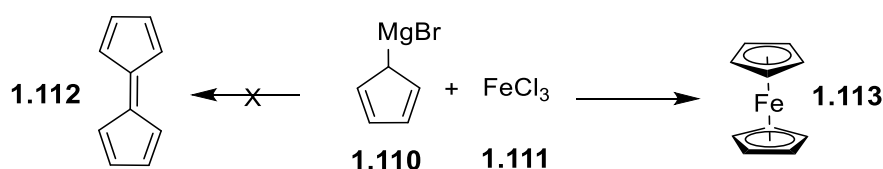


*Scheme 18. SuRE with thiolactones. Side chain insertion is achieved using DMAP and pyridine to promote *N*-acylation, followed by Fm deprotection which passes through a bicyclic intermediate to result in ring expansion. Fm = Fluorenylmethyl.*

To summarise, there are challenges associated with the synthesis of organic, functionalised macrocycles and medium-sized rings, particularly associated with side reactions, which result in low yields and a requirement to use high-dilution conditions. Expanding smaller rings via an intermediate medium-sized ring offers significant improvements and practical advantages. Significantly, SuRE is a promising technique which minimises side reactions and allows fine control over the product formed resulting in a large library of macrocycles and medium-sized rings. It can also be done successively, and theoretically indefinitely. SuRE is therefore a promising strategy for use in the synthesis of a wider range of functionalisation and for more challenging macrocyclic products. It is likely that the full breath of its versatility is only just being explored.

### 1.5 Introduction to Ferrocene

Ferrocene (Fc) was first observed in 1951 by Thomas J. Keally and Peter L. Pauson, who had originally aimed to synthesise bicyclopentadienylidene from cyclopentadienylmagnesium bromide and  $\text{FeCl}_3$  (Scheme 19), but instead obtained an air-stable orange solid. Finding this solid to have the molecular formula  $\text{C}_{10}\text{H}_{10}\text{Fe}$ , Keally and Pauson proposed a structure (figure 13a) which included  $\sigma$ -bonds from the cyclopentadienyl (Cp) rings to the central iron atom and suggested that enhanced stability was due to a combination of its aromatic nature and resonance effects.<sup>66</sup>



*Scheme 19. The accidental synthesis of ferrocene instead of bicyclopentadienylidene from cyclopentadienylmagnesium bromide and  $\text{FeCl}_3$ .*

In 1952, soon after its discovery, Geoffrey Wilkinson and Robert Burns Woodward published an alternative structure. The structure described ferrocene as a sandwich, with  $\eta^5$ -coordinated Cp rings bonding a central iron atom (figure 13b). The structure was later confirmed by X-ray crystallography. Wilkinson and Woodward's publication also noted the reversible oxidation of ferrocene's neutral state into the cation  $[\text{C}_{10}\text{H}_{10}\text{Fe}]^+$  which was seen to be stable and paramagnetic.<sup>67</sup>

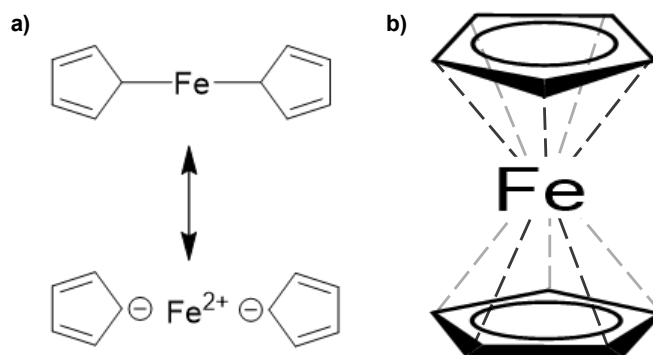


Figure 13. Structure of ferrocene. a) structure proposed by Keally and Pauson in 1951 b) current structure accepted by the scientific community, proposed by Wilkinson and Woodward in 1952.

Since then, ferrocene has been extensively studied for its exceptional properties which include:

- Thermal stability (extending to 400 °C)
- Low energy barrier for rotation, 4 kJmol<sup>-1</sup> of the Cp rings.<sup>15</sup>
- Unique and versatile reactivity such as reactivity with electrophiles
- Reversible 1 electron oxidation at low voltages (+ 0.4 V vs. saturated calomel electrode (SCE))
- Tuneable optical and electrochemical properties upon addition of electron withdrawing and donating substituents.

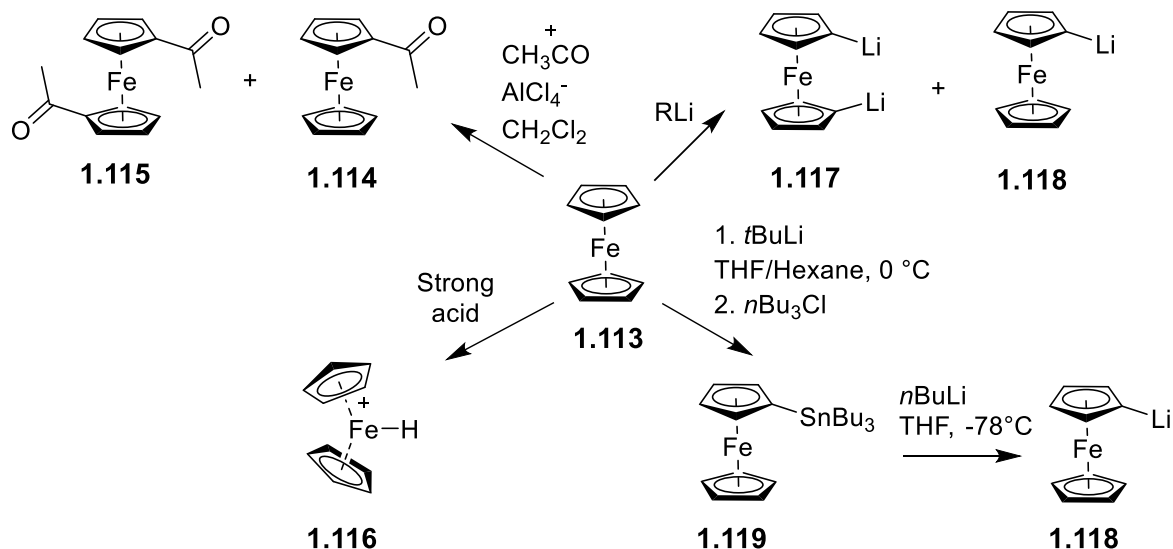
The background and properties of ferrocene have been reviewed in depth.<sup>68</sup> It is clear that study of these properties over the last 70 years has not only allowed a better understanding and exploration of organometallic chemistry but has also allowed for investigation of ferrocene as a tool for multiple applications, some of which will be explored below.

### 1.6 Ferrocene Properties and Uses

#### Reactivity

One widely studied characteristic of ferrocene is its versatile reactivity (Scheme 20). Due to its aromaticity, ferrocene can partake in a number of reactions which resemble the reactivity of benzene. One such example includes the Friedel-Crafts acylation of ferrocene. This reaction demonstrates the deactivation of both the substituted Cp ring and the unsubstituted Cp ring upon a single acylation to **1.114** causing a second acylation to **1.115** to have a slower reaction rate. This allows fine control over the selectivity of the reaction for the mono- or di-substituted product by the variation of the stoichiometry of the reagents. Increased concentration of aluminium chloride has also been associated with the formation of a complex

salt, **1.116** which is non-reactive to acylation.<sup>69</sup> Formation of similar iron (IV) hydride complexes have been associated with protonation of ferrocene by strong acids.<sup>15</sup>



*Scheme 20. The different reactivities of ferrocene. Inspired by a figure from Didier Astruc's review.<sup>15</sup>*

Lithiation of ferrocene has also been used for applications such as alkylation reactions and the formation of ferrocene amides.<sup>70,71</sup> Formation of (tri-*n*-butylstannyl)ferrocene **1.119** has allowed the selective formation of the mono-lithiated form of ferrocene, in contrast with direct lithiation which forms both the mono- (**1.118**) and di- lithiated (**1.117**) form.<sup>72</sup>

### Redox Activity

Ferrocene's ability to undergo a mild one electron oxidation to the ferrocenium ion at + 0.4 V (vs. SCE, Figure 14) has led to its use as a ubiquitous reference for redox potential along with other substituted ferrocenes such as dexamethylferrocene.<sup>33,72</sup> Substituting ferrocene with electron withdrawing or donating groups also allows alteration of the redox potential, with electron withdrawing substituents increasing redox potential and *vice versa*. This allows fine-tuning of ferrocenes for applications such as reducing agents.<sup>68</sup> Furthermore, the redox activity of ferrocene has been explored in more versatile applications such as for sensors,<sup>73</sup> in molecular electronics,<sup>74-76</sup> liquid crystals,<sup>77</sup> or in medicinal chemistry.<sup>78</sup>

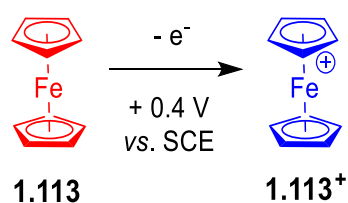
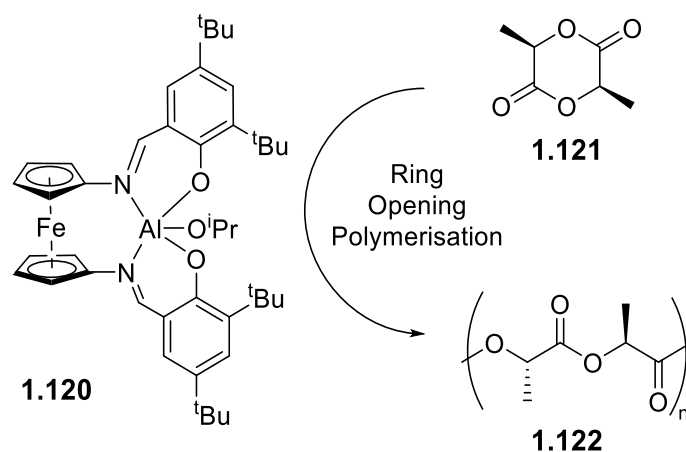


*Figure 14. One electron oxidation of ferrocene to its ferrocenium ion. Colour change is from orange to dark blue. Oxidation occurs at + 0.4 V vs. SCE.*

The oxidation from ferrocene to ferrocenium allows ferrocene-derived moieties to switch from having strong electron-donating behaviour to electron-withdrawing behaviour and this can be presented throughout the molecule to which the moiety is bound. This has allowed ferrocene to be used in redox-switchable catalysts. One example (Scheme 21) published in 2019 by Lai *et al.*,<sup>16</sup> explored the use of **1.120** as a catalyst for ring opening polymerisation (ROP) e.g. **1.121**→**1.122**. Control over which rings the catalyst was active for could be achieved *via* oxidation. When in the neutral form the catalyst was active for polymerisation of certain rings such as lactones, however when oxidised it became inactive for lactones and active for epoxides. This allowed the formation of block co-polymers where switching between neutral and oxidised states of **1.120** resulted in a switch in the monomer unit being reacted. This may have applications in improving ROP procedure by reducing the need for purification steps.



Scheme 21. The ROP of different monomeric rings such as *L*-lactide illustrated here, by a ferrocene-linked aluminium complex developed by Lai *et al.*,<sup>16</sup>

Ferrocene redox sensors generally consist of a motif which interacts with the analyte attached to a ferrocene unit *via* an conductive spacer and a change in redox potential of the ferrocene will be detected *via* electrochemical analytics.<sup>68</sup> Such sensors have wide-reaching applications in medicinal chemistry. For example, in 2019 a reduced graphene oxide (rGO) electrode was doped with ferrocene by Matysiak-Brynda *et al.*, for use as a glucose sensor.<sup>79</sup> Upon binding of glucose to glucose oxidase, ferrocene was able to transfer the resultant change in redox state to the rGO electrode allowing the current increase to be detected via cyclic voltammetry (CV, Figure 15). This technology was successful at determining glucose concentration, even at low concentrations in rat serum, making it a promising technology for use in a medical setting, improving pre-existing medical devices such as blood-glucose detectors which work in a similar way.

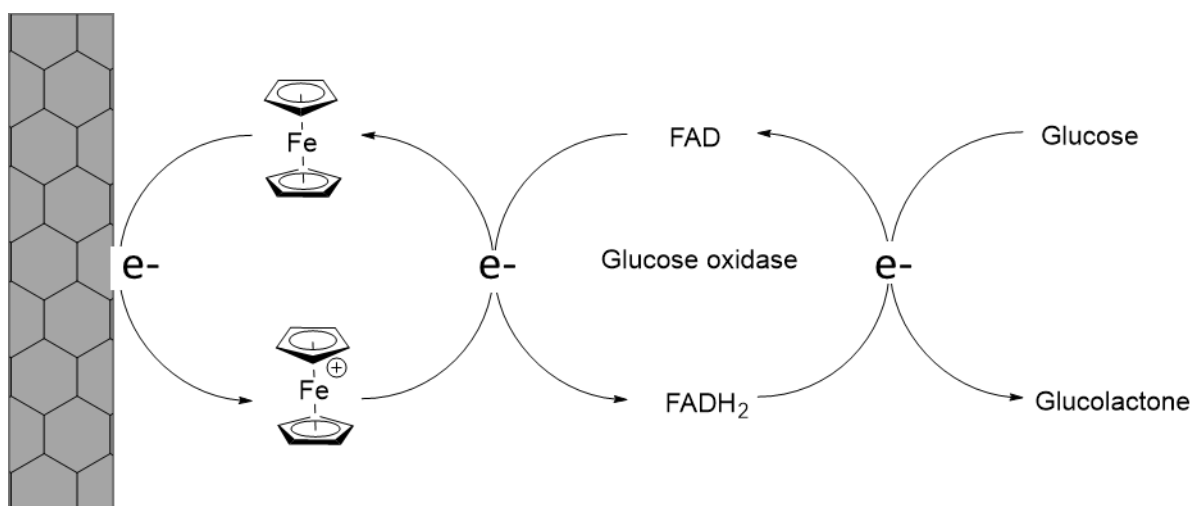


Figure 15. Ferrocene-based redox sensor. The device is able to detect glucose via transfer of a charge to a rGO electrode. Electrons are passed from glucose bound to glucose oxidase, to  $FADH_2$ , to ferrocenium and a charge is detected by a rGO electrode.

Transition metals can influence the characteristics of molecular wires such as charge-voltage traits and conduction,<sup>80</sup> which has led to attention in the field of molecular electronics. Ferrocene-containing molecular wires have been shown to have a successful application in clean energy production. In 2017, Bazan's group designed molecular wire **1.222** which can act as a "protein prosthetic" to improve electron transfer between the bacterium *S. oneidensis* and a working electrode for use in bioelectrochemical reactors (Figure 16).<sup>17</sup> This study was also shown to have applications in bioremediation of water sources as wire **1.222** not only improves the electron yield from substrates but also improves contaminant breakdown.

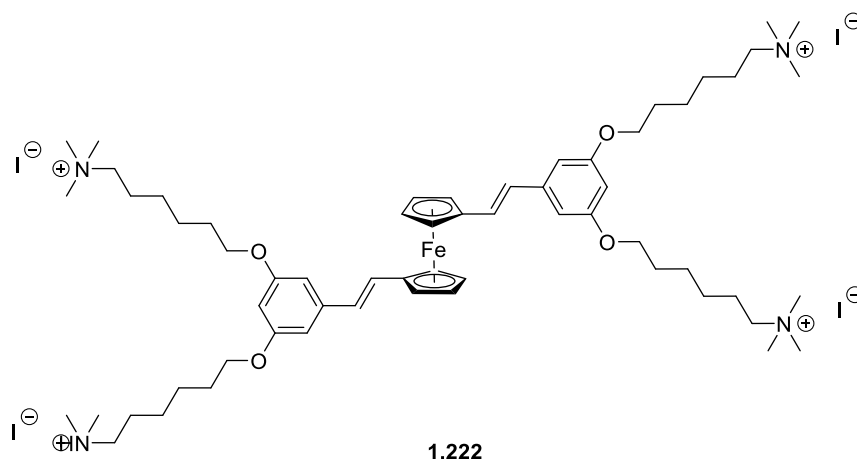


Figure 16.  $DSFO^+$  molecular wire developed by Bazan's group<sup>17</sup>

Redox gating is a common mechanism for control of charge transfer in organometallic wires. A study by Xiao *et al.*,<sup>81</sup> aimed to synthesis and analyse thiol-terminated ferrocene-based molecular wires **1.223** and **1.224** (Figure 17). The ability for these molecules to act as gated wires was investigated by tracking the conductance of the molecule against electrode potential

using a scanning tunnelling microscope (STM) break-junction technique. The study found fluctuations in current and a general increase in conductance when moving from the reduced to oxidised ferrocene states, which would infer that ferrocene could act as a redox gate. CV also demonstrated a lack of communication between adjacent molecules in a monolayer, which illustrates an improved intramolecular electron transport as intermolecular electron transport is suppressed. This type of gating could aid macrocyclic molecular electronics such as those described previously.

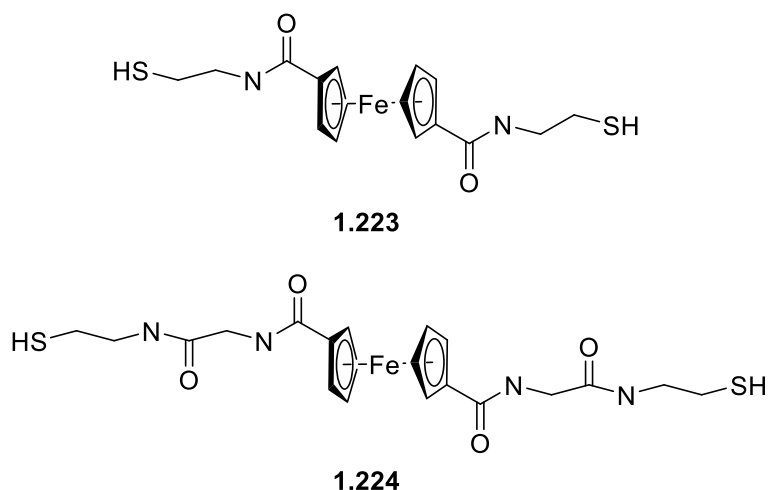


Figure 17. Thiol terminated ferrocene molecular wires developed by Xiao *et al.*,<sup>18</sup>

## Steric Behaviour

Ferrocene also exhibits unique steric behaviour which allows an even more diverse array of applications. Generally, the Cp rings of ferrocene are in a parallel orientation, however under certain conditions they are able to tilt up to 30°. This allows ferrocene to form unique products such as ferrocenophanes (Figure 18).<sup>81</sup> These compounds are *ansa*-metallocenes which have the Cp rings linked by at least one bridging atom and can be highly strained, allowing for applications in ROP. An example, published by Nelson *et al.*, in 1997, describes the synthesis of multiple ferrocene-containing polymers, **1.225** via ROP of carbon-bridged [2]ferrocenophanes, **1.226** (Figure 19).<sup>82</sup>

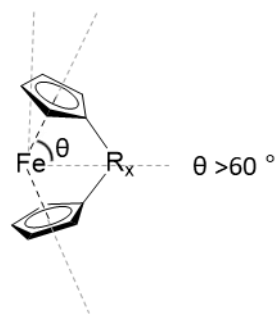


Figure 18. Generalised diagram of a ferrocenophane. Ferrocene's Cp rings are able to tilt by up to  $30^\circ$  to form a  $60^\circ$  between the centre of the Cp ring and the iron centre.

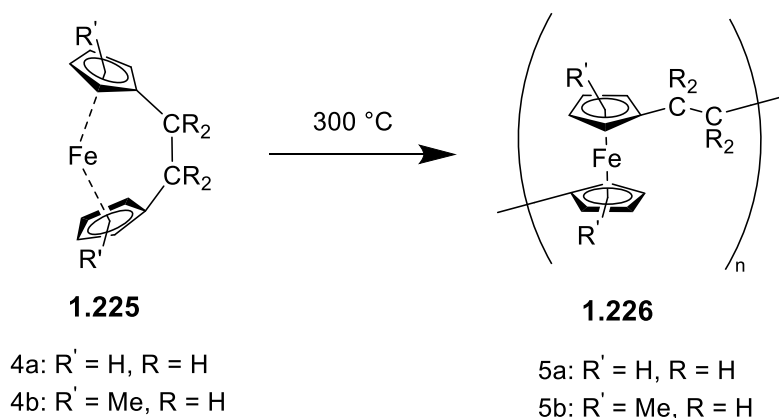


Figure 19. The ROP of carbon-bridged [2]ferrocenophanes to form poly(ferrocenylethy1ene)s

Tilting of the Cp rings also allows for coordination of a metal ion via an  $\text{Fe} \rightarrow \text{M}$  dative bond, forming  $\kappa^3$  coordination systems (Figure 20; **1.227**) in catalysts which bind two donor atoms and the active catalytic metal centre. These have shown advantages over  $\kappa^2$  coordination systems (Figure 20; **1.228**) such as faster reaction times which may be due to the ferrocene acting as a metal-coordinating ligand.<sup>83</sup>



Figure 20. Tilting of ferrocene's Cp rings to allow coordination of **1.227** in a metal ion  $\kappa^3$  coordinated system and non-tilted  $\kappa^2$  coordinated system **1.228**. D= donor atom, M=metal, L=ligand

Furthermore, ferrocene has a low energy barrier of rotation for its Cp rings of  $4 \text{ kJmol}^{-1}$  (Figure 21). Ferrocene is therefore able to exist in both an eclipsed ( $D_{5h}$ ) and staggered ( $D_{5d}$ ) conformation. Particularly, rotation of the Cp rings around the ferrocene axis allows ferrocene to optimise itself for binding such as in catalysis or inside enzyme pockets. A study using X-

ray crystallography found that ferrocene is able to use rotation to optimise interactions between itself and the active site of an enzyme such as carbonic anhydrase which is a therapeutic target for a number of diseases.<sup>84</sup> This could therefore allow ferrocene to be investigated for use as a therapeutic enzyme inhibitor. This optimisation ability could also aid the use of macrocycles for these type of applications, potentially allowing them to adapt their conformation to fit to enzyme pockets more efficiently.

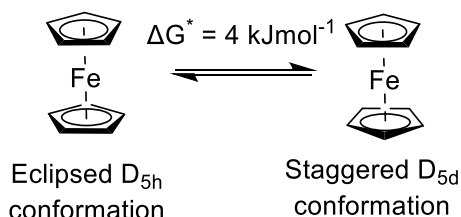


Figure 21. Rotation of ferrocene's Cp ring between eclipsed ( $D_{5h}$ ) and staggered ( $D_{5d}$ ) conformations via a small energy barrier of  $4 \text{ kJmol}^{-1}$ .

This low-energy barrier to rotation also has implications in molecular electronics, specifically in mechanical gating. Camarasa-Gómez *et al.*,<sup>85</sup> demonstrated that ferrocene exhibited varying electron transport properties (conductance) as a function of the twist-angle of the Cp-Fe-Cp axis (Table 1). It was found that the straight chain ferrocene molecules studied had very low conductivity, but mechanical adjustment allowed conductivity to increase due to improved overlap of molecular orbitals. STM-based studies found that the conductivity increased by 6.7 times when the ferrocene junction was in the "closed" position at  $90^\circ$  which was found to be due to constructive quantum interference mediated by the interaction between the d-orbital and the  $\pi$ -system of the Cp ring.

Table 2. Relationship between charge transfer interference and rotational conformation of the ferrocene (Fc) Cp rings.

Rotation of Cp rings	$0^\circ$	$30^\circ$	$90^\circ$
Diagram			
Interference	Relaxed	Destructive	Constructive

## Optical Properties

Finally, ferrocene has also been recognised for its optical properties. As an aromatic organometallic compound, ferrocene is colourful and switches between its orange, neutral state and its blue, positively charged state when oxidised (Figure 22). This has been particularly useful in fluorescent sensors. Ferrocene's applicability to environmental sensors was demonstrated by Zapata *et al.*,<sup>86</sup> who synthesised **1.299** (Figure 23) which, when bound to either  $\text{Hg}^{2+}$ ,  $\text{Zn}^{2+}$  or  $\text{Pb}^{2+}$  showed a shift in UV-Visible absorption spectra unique to each ion and observable by the naked eye. UV-Visible spectroscopy also showed an increase and decrease in distinct absorption bands when the concentration of  $\text{Hg}^{2+}$  was increased or decreased, indicating that the sensor was concentration dependant. This shows the ability of ferrocene to produce accurate and selective sensors. Many other examples of ferrocene-conjugates being used in sensing have been reviewed elsewhere.<sup>87</sup>

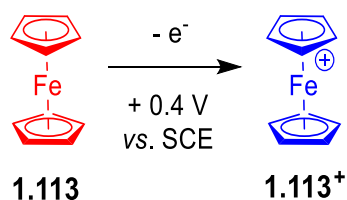


Figure 22. One electron oxidation of ferrocene its ferrocenium ion. Colour change is from orange to blue. Oxidation occurs at +0.4 V vs. SCE

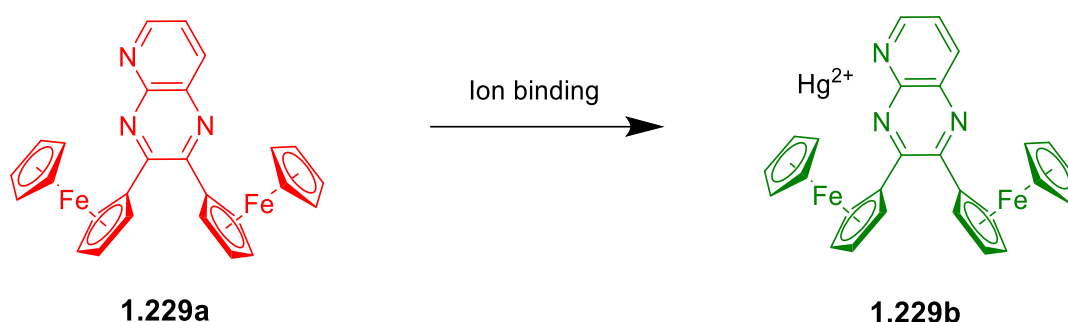


Figure 23. Ferrocene-based environmental sensor developed by Zapata *et al.*,<sup>85</sup> binding of  $\text{Hg}^{2+}$  shifts UV-Visible absorption spectra.

Ferrocene's unique properties, stability and affordability has allowed it to be used for a number of applications as discussed in this section. Therefore, targeting ferrocene for the implementation of organometallic components into macrocycles and medium-sized rings could allow the synthesis of macrocycles with altered properties. The synthesis of ferrocene-containing macrocycles is a topic of considerable interest (*vide infra*) but as with most

macrocycles, there are inherent challenges associated with their synthesis. Examples of the synthesis of macrocycles with ferrocene components are discussed in the next section.

### *1.7 Ferrocene-containing Macrocycles*

Due to the aforementioned properties and applications of ferrocene-based molecules, it may be useful to incorporate ferrocene as a component in medium-sized and macrocyclic rings. In fact, a number of examples of ferrocene-containing rings existing in the literature and can be split into two groups: (i) endo- and exo-functionalised ferrocene macrocycles and (ii) edge- or corner-functionalised ferrocenes (Figure 24). The most common type is endo/exo-functionalised macrocycles, in which the ferrocene moieties are on the inside or outside of the macrocycle respectively, rather than part of the backbone of the macrocycle **1.130** and **1.131**. Exo-functionalised macrocycles are beyond the scope of this review, but examples have been reviewed previously.<sup>88–90</sup>

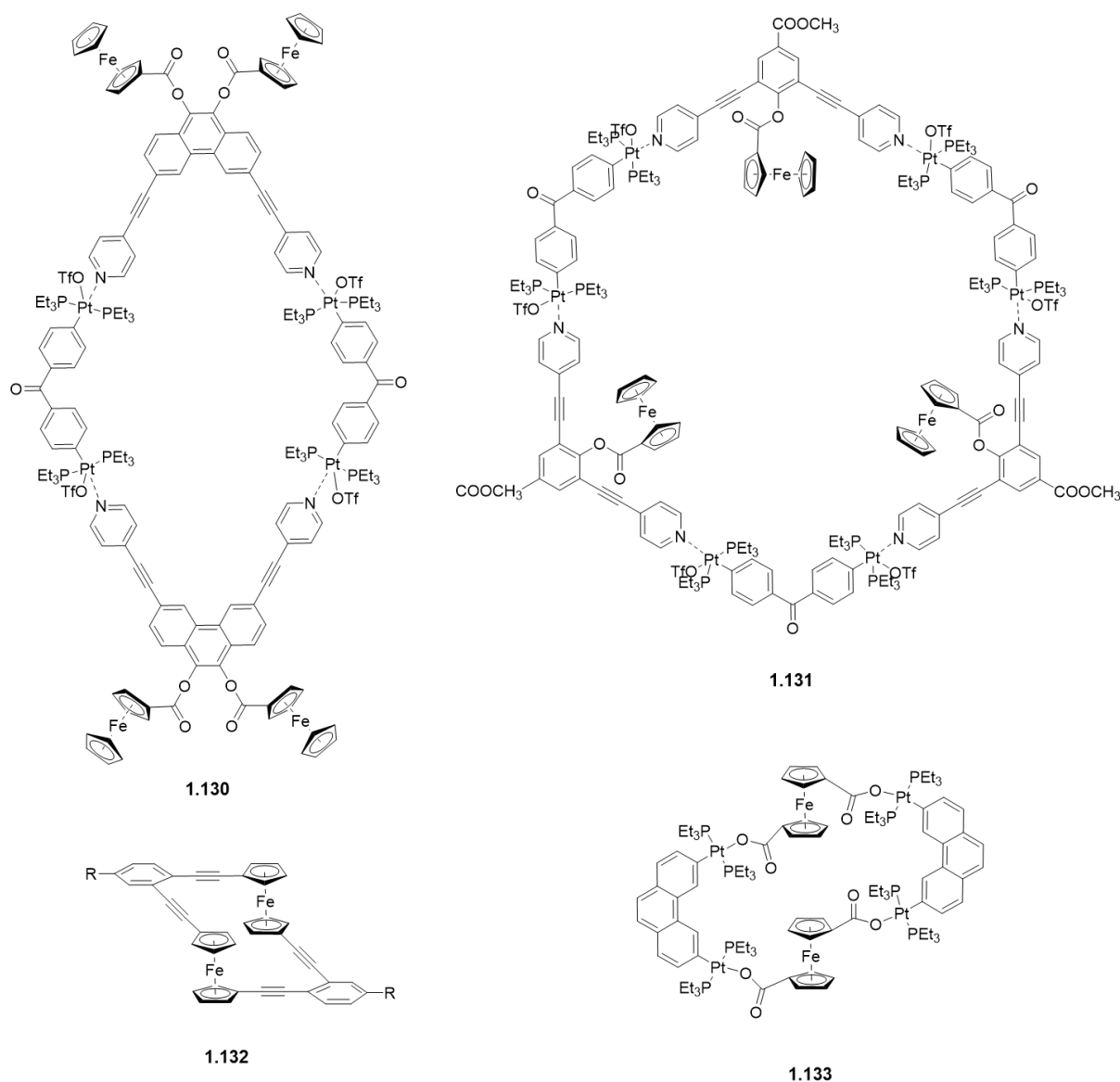
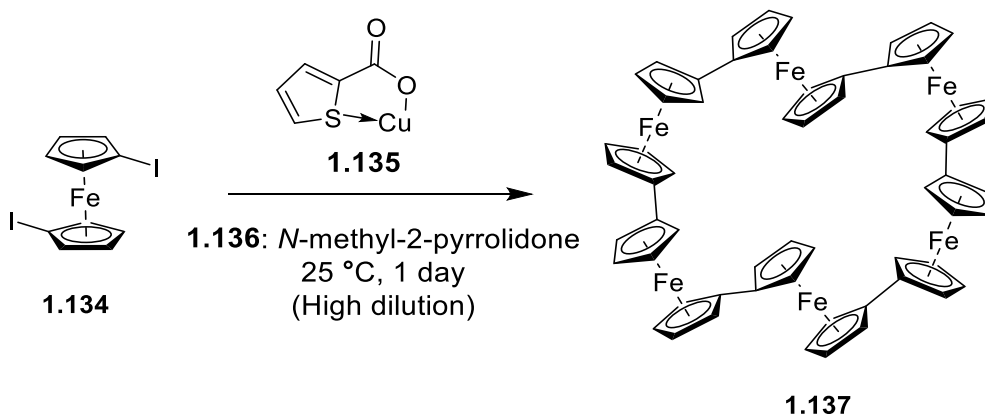


Figure 24. Different types of ferrocene macrocycles. a) *exo*-functionalised; b) *endo*-functionalised; c) *edge*-functionalised and; c) *corner*-functionalised.

Here, the focus will be on *edge*- and *corner*-functionalised ferrocene macrocycles which incorporate ferrocene as part of the backbone or the macrocycle **1.132** and **1.133**. Long's group demonstrated the synthesis of perhaps one of the most impressive of these, compound **1.137** (Scheme 22), an oligomer synthesised from 6 ferrocene-containing monomers (**1.134**).<sup>91</sup> **1.137** was shown to be redox-active with four sequential 1 e<sup>-</sup> reversible oxidations. It was demonstrated that charge transfer between the ferrocene centres was faster than charge transfer in solution, which could indicate possible applications in molecular wires. Furthermore, crystallography studies of **1.137** demonstrate that ferrocene's mechanical flexibility may allow for host-guest activity, which could infer an applications in devices such as sensors.



Scheme 22. **1.134** which incorporates six ferrocene-1,1'-diyl units.

In fact, a number of examples of edge- and corner-functionalised ferrocene macrocycles have been demonstrated to have possible applications as sensors.<sup>92–94</sup> Recently, Song *et al.*,<sup>95</sup> demonstrated the use of ferrocene-containing macrocycle, **1.131** as a monomer for implementation into ferrocene-containing covalent organic framework nanosheets (Fc-COFNs), illustrated in Figure 25 for sensing Cardiac troponin I (cTnI), a highly important biomarker for early diagnosis of acute myocardial infarction (AMI). The Fc-COFNs were assembled on gold electrodes, allowing their electrochemical response to be measured. This device used aptamer strands, short strands of DNA or RNA which can bind target molecules, to bind cTnI. Previous devices using aptamer strands in this way have struggled with aptamer immobilisation, however here the aptamer strands were able to bind to the Fc-COFN via hydrogen bonds and  $\pi$ -stacking interactions induced  $\pi$ -conjugation present in the macrocyclic framework. Binding of the cTnI specific aptamer strands reduced the electrochemical response of ferrocene. This response could then be restored upon addition of cTnI which removed aptamer strands from the framework, allowing the Fc-COFNs to successfully detect the presence of cTnI at a low limit of detection. It is therefore possible that this design could be used to aid early diagnosis of AMI in the future.

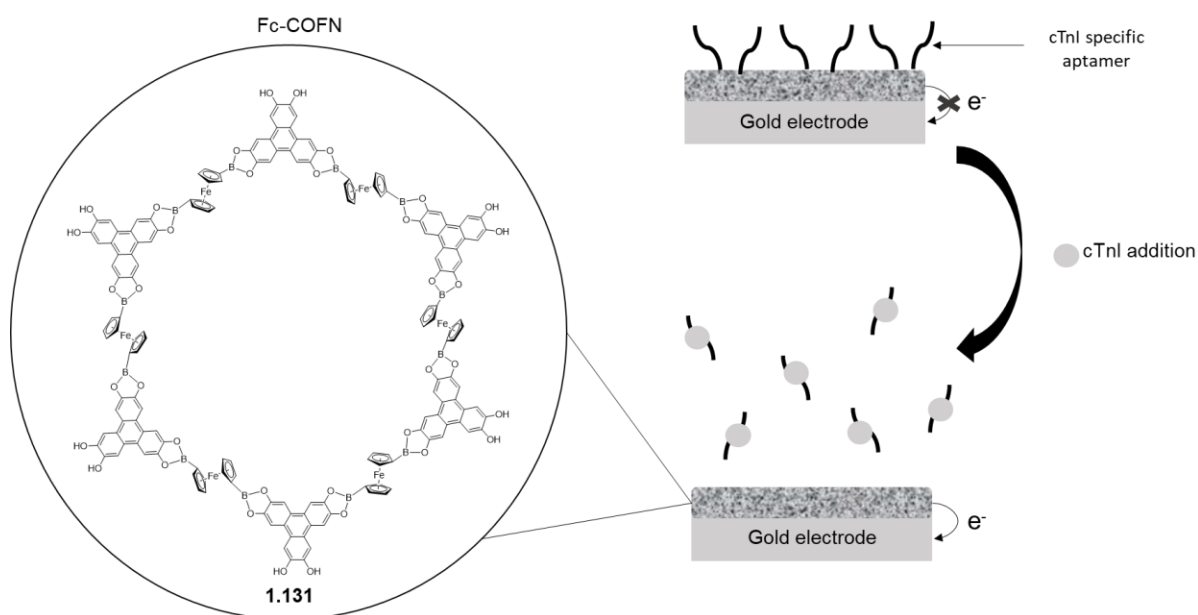


Figure 25. Ferrocene-containing covalent organic framework nanosheets, compound **1.131**, assembled on gold electrodes for use in early detection of AMI.

Another area of interest in ferrocene macrocycles is that of cyclic ferrocene-peptide conjugates.<sup>96</sup> These are macrocycles which include ferrocene attached to peptide chains, causing the peptide structure to alter, allowing for a wide range of conformations. These macrocycles have seen a range of properties, particularly, the combination of peptide chains and ferrocene, which resembles the structure of iron containing proteins, may allow for simulation of biological activity, insinuating possible applications in medicinal chemistry.

Modelling of biological systems could be one such application. Models for biological channels such as transmembrane pores are in high demand due to their potential ability to aid drug delivery.<sup>97</sup> Difficulties with mimicking hydrogen bonding associated with the  $\beta$ -sheet motifs often present in these channels have, however, been experienced. Through the synthesis of a cyclic ferrocene-peptide conjugate, **1.138** (Figure 26) Kraatz's group was able to mimic such motifs.<sup>98</sup> The rotational freedom of ferrocene's Cp rings allowed for a 1,2'-conformation resulting in cyclisation and the formation of hydrogen bonds resembling those in antiparallel  $\beta$ -sheets to form between N-H and C=O groups on the peptide backbone. This allowed the macrocycles to behave like channels, which could result in their use in biological channels mimetics. Their ability to hydrogen bond and their electrochemical activity also lend these macrocycles to applications in hydrogels or as drug delivery targets.<sup>99</sup>

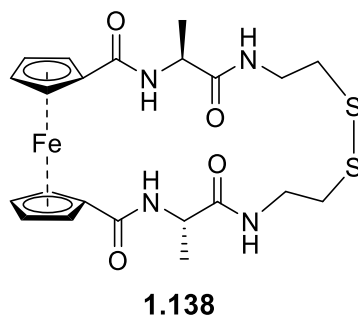


Figure 26. Cyclic ferrocene-peptide conjugate **1.138**, used to mimic with a 1,2'-conformation with respect to the ferrocene moiety.

Finally, a particularly fascinating property seen in ferrocene macrocycles caused by a ferrocene's redox activity was observed recently by Yang's group<sup>100</sup> which builds on work looking at the inversion of chirality caused by changes in the redox states of transition metal complexes. The authors synthesised complex **1.139** for which the capture and release behaviour of the fused ferrocene-containing ring could be controlled by oxidation/reduction of the complex. Upon oxidation, the ferrocene-containing ring moved into the pillar[6]arene creating a host-guest complex (Figure 27). The results indicated a possible application in nanomachinery. This study not only demonstrated how the implementation of ferrocene into a ring system can have a novel impact on a macrocycle's properties, but also provided an example of how these ring systems could have marketable applications.

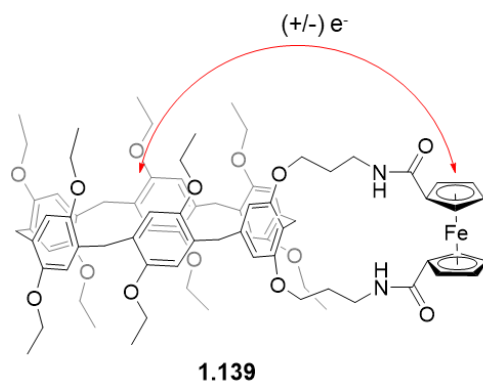


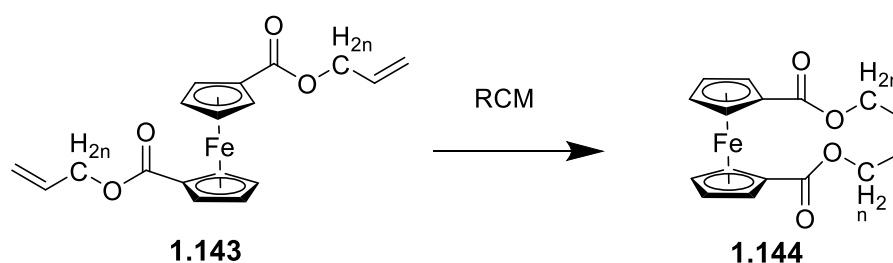
Figure 27. Electrochemically controlled conjugate macrocycle **1.139**. Upon oxidation the ferrocene-ring moves into the pillar[6]arene to form a host-guest complex

### 1.8 Synthesis of Ferrocene Macrocycles

Previously, ferrocene macrocycles have been synthesised by a variety of literature methods such as thermal ring-opening polymerisation (TROP), ring closing metathesis, cross-coupling

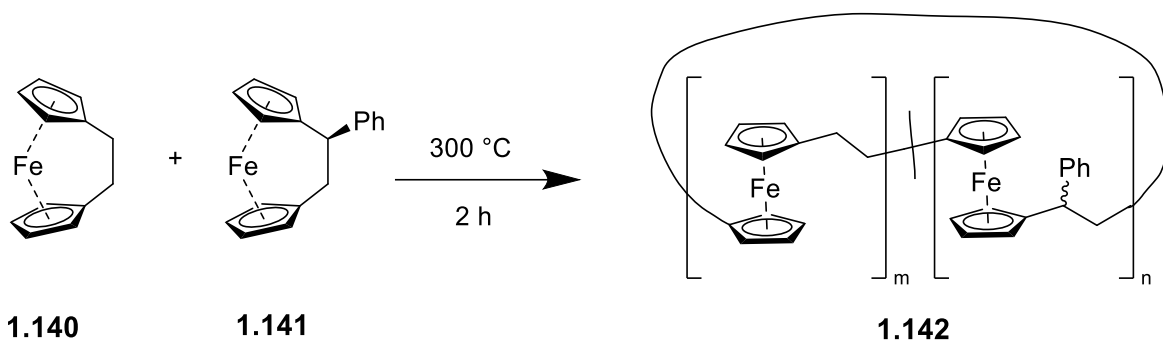
reactions, and coordination driven chemistry.<sup>101–104</sup> However, there are significant drawbacks associated with poor selectivity for the intended products and difficult synthesis of larger rings. Particularly, reduced yields due to side reactions such as dimerization is a problem and this often results in high dilution conditions being required, which is not easily applicable to scale-up.

RCM is an attractive method for the formation of unsaturated ferrocene-containing macrocycles and medium-sized rings (Scheme 23). One study explored the formation of ferrocene-containing rings by this method for use as monomers in ROP to form linear polymers.<sup>105</sup> The group was able to synthesis a range of unsaturated ferrocene-containing macrocycles e.g. **1.144**, however this method still suffered from low yields due to intermolecular side reactions, necessitating the use of high-dilution conditions. It was found that the success of RCM was determined by both ring size and the groups linking the ferrocene substituent and the alkene, with larger rings being more likely to form due to lowered ring strain. Different groups favoured different stereochemistry where ester groups favoured cyclic monomers with *cis* selectivity and bisacrylate-containing structures favouring *trans*-isomers when longer chain lengths are used. This selectivity is likely to have prevented the formation of medium-sized rings and smaller macrocycles by this method. Furthermore, the olefin group present in **1.144** is likely to restrict the rotation of ferrocene's Cp rings, therefore resulting in a less flexible ring which may limit its properties and applications.



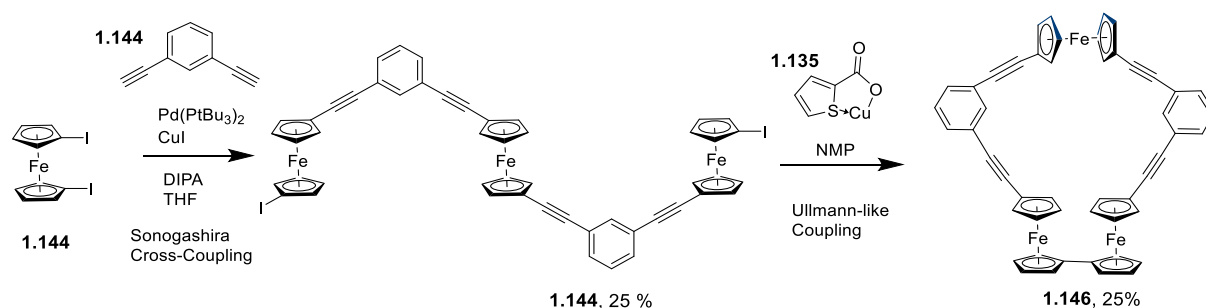
Scheme 23. RCM of olefin monomers.

Alternatively, TROP is able to exploit the ring strain in ferrocenophane starting materials to form cyclic polymers when heated to 300 °C. A study by Gilroy *et al.*,<sup>101</sup> found that heating provided the energy required for Fe-Cp bond cleavage, which then allowed the reformation of more stable, larger rings (Scheme 24). Although a variety of cyclic polymers could be formed (**1.142**), problems with the formation of linear products were still experienced, along with issues of poor solubility and practically no control over the nature of the polymers formed. Furthermore, any other functional groups included would have to be on the outside of the ring, rather than in the backbone. It should also be noted that polymerisation-based cyclisation will always result in at least two ferrocene moieties present in the ring, therefore if it is intended that only one ferrocene centre be present, these techniques would be inadequate.



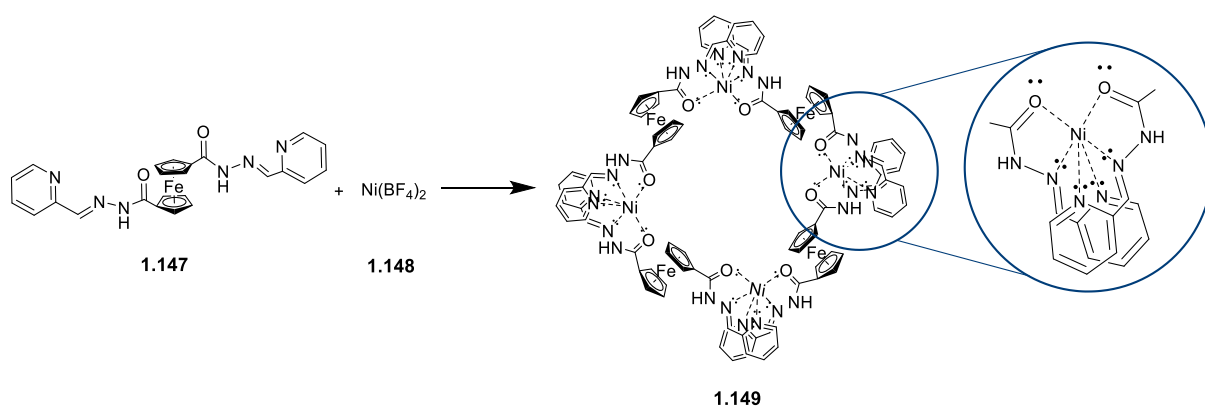
**Scheme 24.** TROP of strained ferrocenophanes **1.140** and **1.141** to form cyclic polymer **1.142**.

Significantly, an example of the synthesis of ferrocene-containing macrocycles via cross-coupling includes work done by Long's group, in which **1.146** was synthesised via Sonogashira cross-coupling and Ullmann-like coupling (Scheme 25).<sup>103</sup> This paper demonstrated that ferrocene-containing macrocycles have unique electronic properties in comparison to their linear equivalents and later work by Long's group indicated the presence of intervalence charge transfer and mixed-valency in biferrocene-containing rings which could infer properties such as improved conductivity or redox modulation.<sup>106</sup> Here, rigidity was implemented into the rings, overcoming problems with previous synthetic methods caused by the rotation of ferrocene's Cp rings. The method also allowed for high control of the rings being formed and variation of the linker groups, allowing for easy formation of rings with varied properties. However, yields of **1.146** at 25 %, indicate that mass is likely lost to side reactions during the formation of linear products. High dilution conditions were used, presumably to try to reduce side-reactions, a technique which is detrimental to a possible scale-up. Furthermore, some of the rings formed were poorly soluble and although implementing rigidity may have improved synthetic efficacy, it does not allow the possible benefit of ferrocene's mechanical flexibility to be explored. More recently, the same group also published the synthesis of pyridyl-bridged ferrocene-containing macrocycles by the same methods, however these suffered from the same issues and presented even lower yields ranging from 3-8 %.<sup>107</sup>



**Scheme 25.** Sonogashira cross-coupling and Ullmann-like coupling to form ridged ferrocene-containing macrocycles.

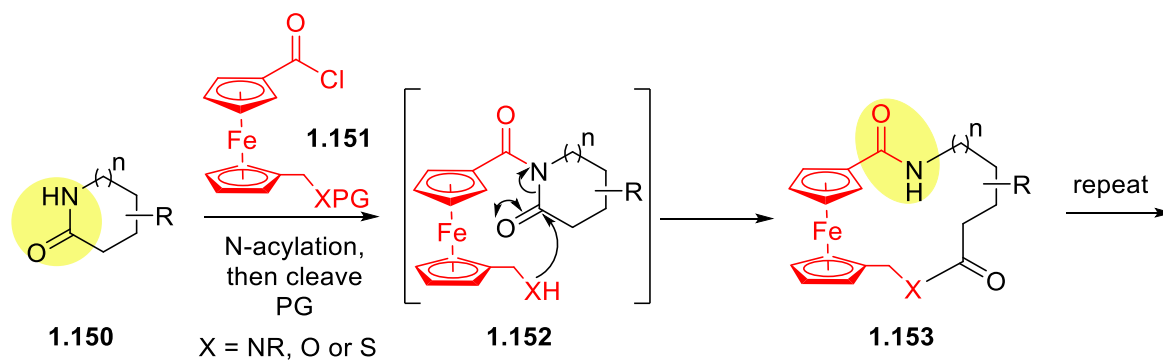
Alternatively, Jiang *et al.*,<sup>104</sup> were able to synthesise hemicage **1.149** by combining precursor units **1.147** and **1.148** using coordination chemistry (Scheme 26) This approach used ferrocene's rotational ability to alter directionality of the linear ligands, aiding formation of the hemicages. Coordination-driven formation of ferrocene-containing macrocycles is an accelerating area in organometallic and macrocyclic chemistry, with syntheses demonstrating facile and high-yielding routes towards a large variety of macrocycles.<sup>108</sup> This approach has the ability to form a variety of macrocyclic rings in almost quantitative yields and larger rings structures have been accessible. However, other disadvantages such as susceptibility to fragmentation, caused by coordination of Lewis basic solvents presents a significant challenge in this area.<sup>109</sup>



Scheme 26. Coordination-driven formation of ferrocene-containing macrocycles.

### 1.8 Project Aims

Current synthetic methods towards ferrocene-containing macrocycles have significant drawbacks which may prevent the facile synthesis of a range of rings. These cyclic structures have shown promise in a range of applications including bioactivity and molecular electronics. For this reason, it would be advantageous to explore other macrocyclic synthesis methods. As discussed above, SuRE has many advantages over other cyclisation methods including reduction of side reactions, a high level of control and the ability for expansions to be repeated successively. Use of SuRE in the synthesis of ferrocene-containing macrocycles and medium-sized rings may therefore be advantageous over previously employed methods to create a library of varying rings in high yields. As of yet, no efforts have been made to synthesise organometallic-containing rings using SuRE, so the implementation of a ferrocene-containing starting material into SuRE will be unprecedented if realised.



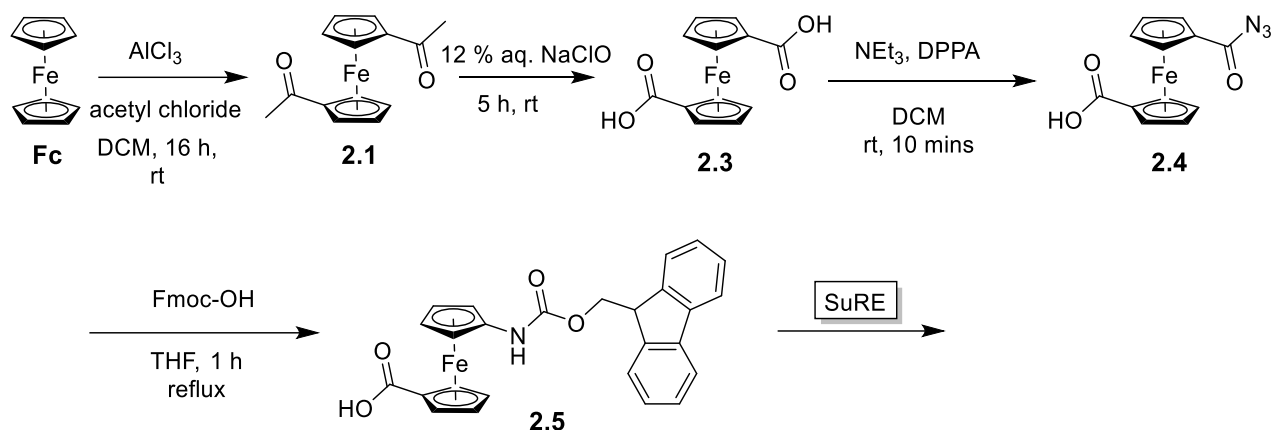
Scheme 27. Synthesis of ferrocene containing macrocycles, **1.153** via SuRE.

Therefore, this project aims to:

- 1) Create a synthetic pathway for key ferrocene-containing starting materials for use in SuRE (Scheme 27)
- 2) Analyse the electrochemical and optical activity of different ferrocene-containing species to identify how they might affect the properties of subsequent rings.
- 3) To perform a ring expansion using a ferrocene-containing starting material to assess whether implementation into SuRE is feasible.

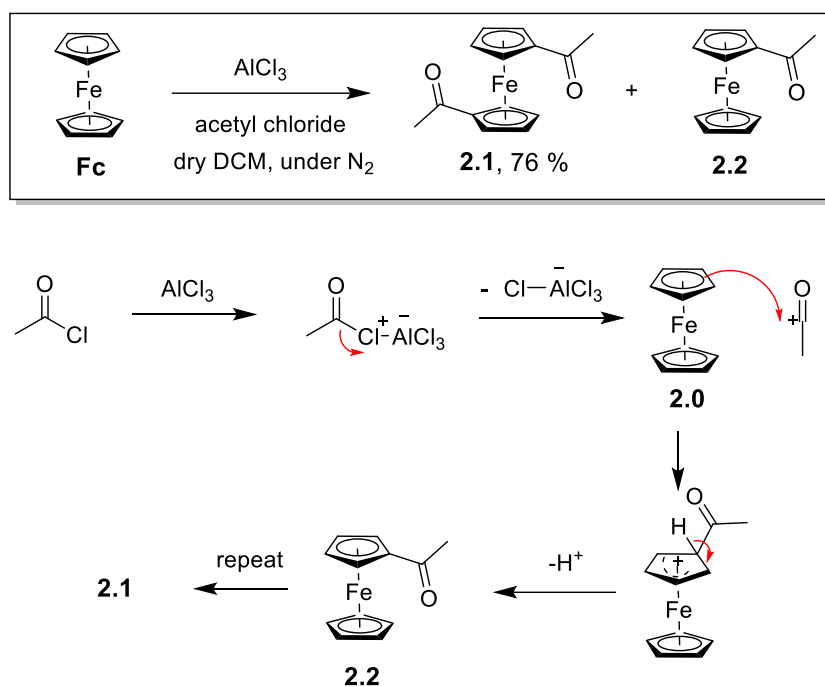
## 2. Synthesis of SuRE Starting Material 2.5

The proposed synthetic pathway for the first ferrocene-based starting material planned for use in SuRE is shown in Scheme 28. Using this route, **2.5** was successfully synthesised and isolated, as described in the following section.



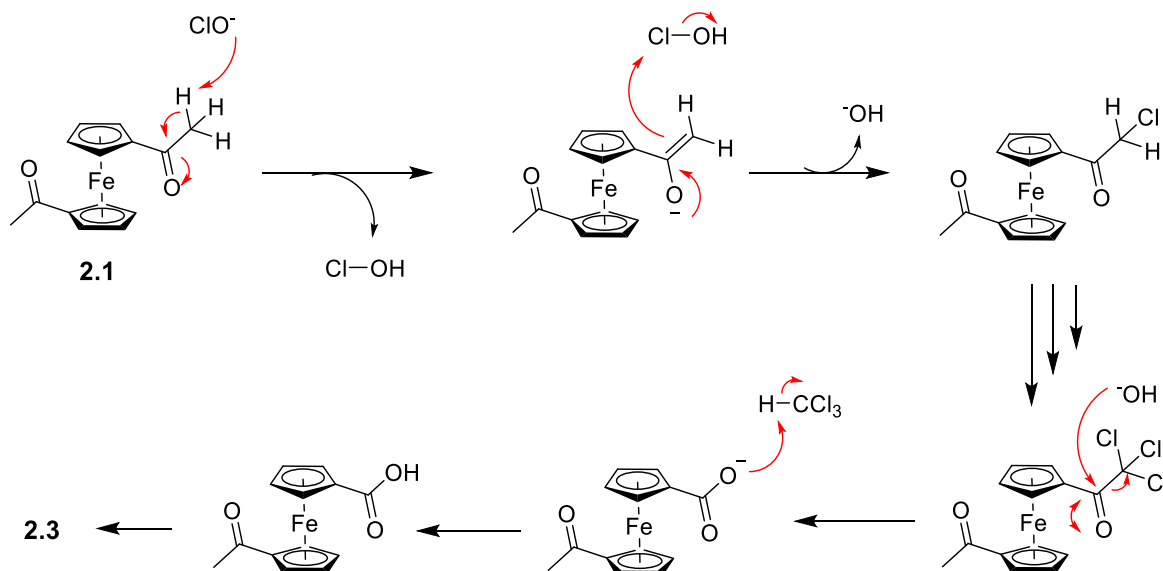
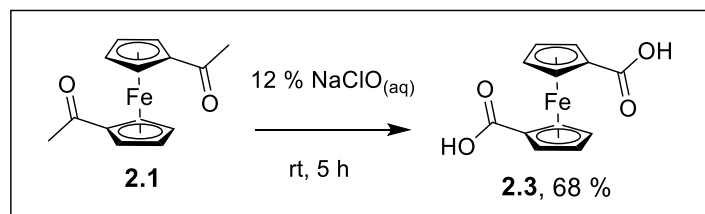
Scheme 28. Proposed Synthetic Pathway for **2.5**. DPPA = Diphenylphosphoryl azide, Fmoc-OH = 9-Fluorenylmethanol

The first step in this reaction scheme is a standard Friedel–Crafts acylation reaction to form **2.1** (Scheme 29). This step was successfully performed using the methodology described by Yang’s group.<sup>110</sup> Our first attempt at this reaction resulted in a 0 % yield; in this attempt, rigorous dry and oxygen free conditions were not used, thus demonstrating the importance of doing this reaction under  $\text{N}_2$  and with dry solvents, likely due to the ease with which acyl chlorides and aluminium chloride react with moisture in the air. Once these more stringent conditions were applied, **2.1** was obtained in a much improved 76 % yield. Formation of **2.1** over side-product **2.2** was favoured by 1) having a relatively long reaction time compared with known mono acylation methods and 2) adding the ferrocene solution dropwise to a pre-stirred solution of aluminium chloride and acyl chloride.



Scheme 29. Reaction scheme and mechanism for the formation of **2.1** and by-product **2.2** from the Friedel-Crafts acylation of ferrocene

The next step involved the oxidation of **2.1** via the haloform reaction to form **2.3**. This was originally attempted using the method outlined by Xaio *et al.*,<sup>111</sup> which involved the bulk addition of 12 % NaClO<sub>(aq)</sub> to **2.1** followed by stirring for 5 hours and purifying by two acid-base washes (Scheme 30), however no pure product could be obtained using this procedure (Table 2, entry 1). The acid-base wash was identified to cause a reduction in the amount of material, so the synthesis was therefore repeated, but omitting the second purification stage from the procedure. This resulted in the isolation of the desired product **2.3** in 25 % yield (Table 2, entry 2). In an attempt to improve the yield, an alternative literature method reported by Kraatz's group was considered;<sup>112</sup> this method reported that the addition of 12 % NaClO<sub>(aq)</sub> at 1.5, 2 and 3 hours intervals led to an improved yield. The same study also reported the use of light protected conditions and rapid stirring. This is likely due to the light-mediated decomposition of NaClO, resulting in its inactivation. Rapid stirring and the addition of fresh reagent throughout the reaction may also allow even distribution of undecomposed reagent which would aid the formation the diacid product. Pleasingly, the application of this modified procedure resulted in the product being obtained in a much improved 68 % yield (Table 2, entry 3). Despite a yield of 68 %, this remained a challenging synthesis and reliably reproducing this yield was not easy. For this reason, **2.3** was purchased from a commercial supplier and the commercial material was used for the following steps of the synthesis.

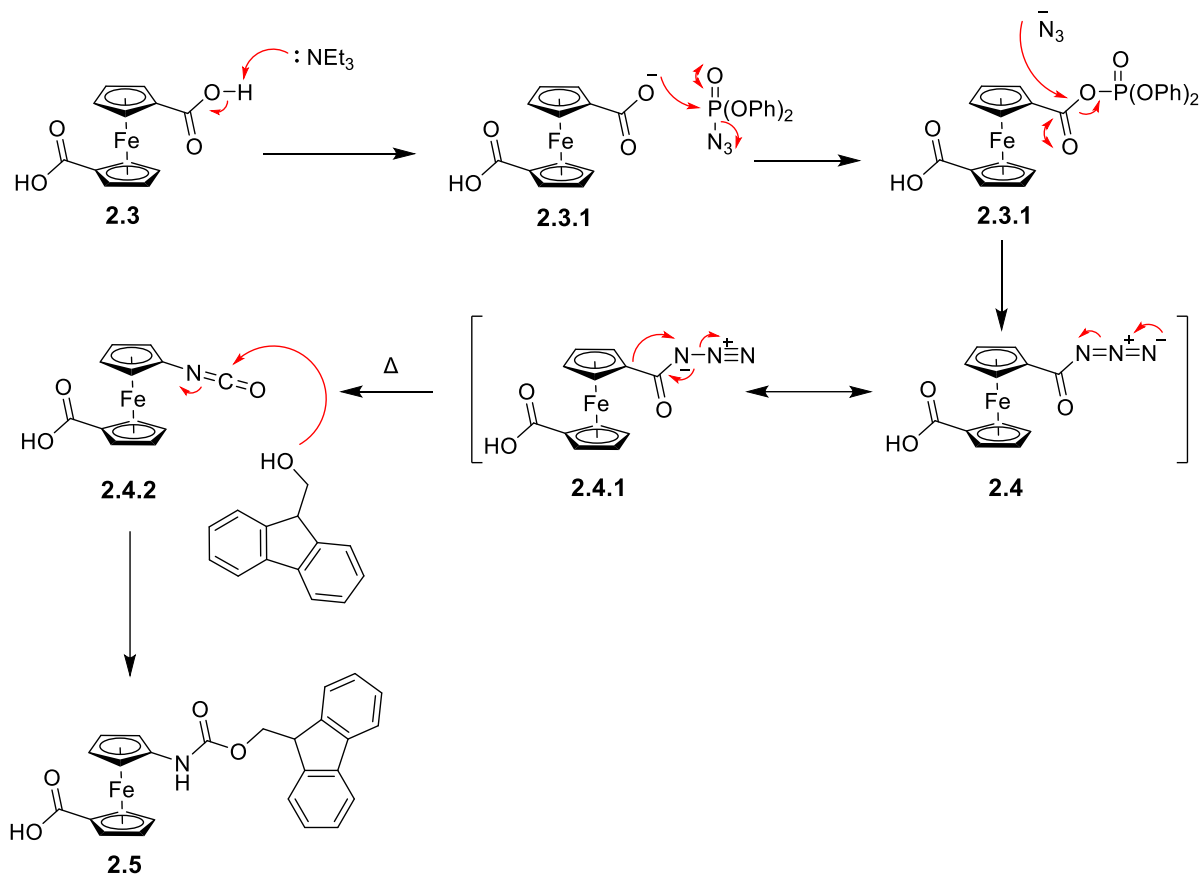
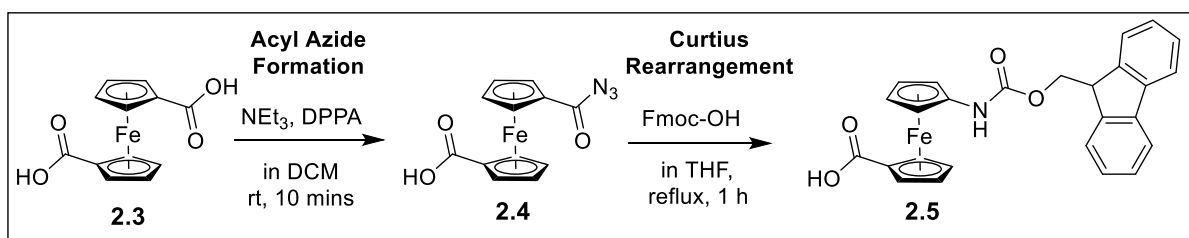


Scheme 30. Reaction scheme and mechanism for the formation of **2.3** from the haloform reaction of **2.1**.

Table 2. Table of the purification methods and reagent addition methods with yields in the formation of **2.3**.

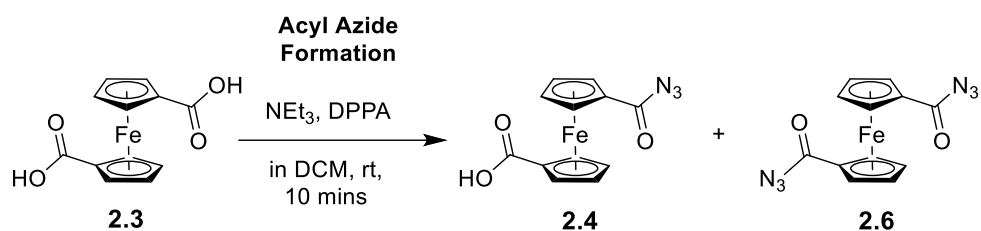
Entry	2nd acid-base wash	Light Protected, Rapid Stirring	Addition method	Yield of <b>2.3</b>
1	Yes	No	Bulk	0 %
2	No	No	Bulk	25 %
3	No	Yes	Portions	68 %

Removing the symmetry from diacid **2.3** to form acyl azide **2.4** was expected to be the most challenging step in the synthetic pathway. For this step a synthetic procedure was adapted from a procedure originally outlined by Erb *et al.*<sup>113</sup> This involved the use of triethylamine and diphenylphosphorylazide (DPPA) as the azide transfer reagent to form **2.4** which would then be followed by a Curtius rearrangement, which is a heat triggered rearrangement of **2.4** to form isocyanate **2.4.1** followed by trapping of **2.4.1** with 9-fluorenylmethanol (Fmoc-OH). This would afford **2.5** which could be used as a starting material for SuRE (Scheme 31).



Scheme 31. Reaction scheme and mechanism of the acyl azide **2.4**, followed by the Curtius rearrangement to form **2.5**.

In a first attempt, azide **2.4** was synthesised in 13 % yield, with the formation of di-substituted side-product **2.6** (Scheme 32, see Table 3 entry 1 for conditions used). Due to the low reaction yield, optimisation of this step was attempted (Table 3). Neither the dropwise addition of DPPA, an increase of reaction time, nor an increase in temperature resulted in an improved yield of **2.4** (entries 1-6) and although the combined yield increase to 45 % after the reaction time was increased to 1 hour (entry 7), this was largely concomitant with an increase in the yield of the diazide side-product **2.6**. An increased yield of **2.4** only resulted when the reaction was scaled up by a factor of 5, resulting in 19 % yield of **2.4** (entry 8).

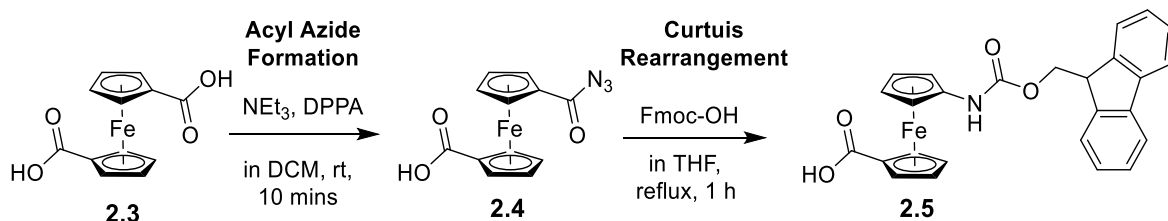


*Scheme 32. Reaction scheme for the synthesis of **2.4** and the by-product **2.6** from **2.3** via acyl azide formation.*

*Table 3. Optimisation table for the formation of **2.4** and by-product **2.5**. \* X2 Net<sub>3</sub>, x5 scale. N/A = compound obtained, but yield not collected.*

Repeat	DPPA dropwise	temp	Time	Yield of <b>2.6</b>	Yield of <b>2.4</b>	Combined yield
1	No	rt	10 min	N/A	13 %	N/A
2	Yes	rt	10 min	N/A	15 %	N/A
3	Yes	rt	10 min	6 %	11 %	17 %
4	Yes	40 °C	10 min	12 %	6 %	18 %
5	Yes	40 °C	30 min	34 %	7 %	40 %
6	Yes	40 °C	20 min	19 %	9 %	28 %
7	Yes	40 °C	1 hour	33 %	8 %	42 %
8*	Yes	rt	10 min	9 %	19 %	28 %

The isolated product commonly retained a DPPA-based contaminant after purification by column chromatography (this has been accounted for in the yields calculated in Table 3&4). The effect of this contaminant on the following Curtius rearrangement step was investigated by purifying the crude product using an aqueous wash and comparing the following reaction yields with non-purified reactions (Scheme 33, Table 4). Purification was seen to have no impact on the sequential reaction and in fact, the total yield of both reactions was lower when this step was included. Therefore, purification from the DPPA contaminant was not implemented into the procedure to prevent further product loss. It should be noted that the contaminant was assumed to be unreacted DPPA and the calculations undertaken were based on this assumption.

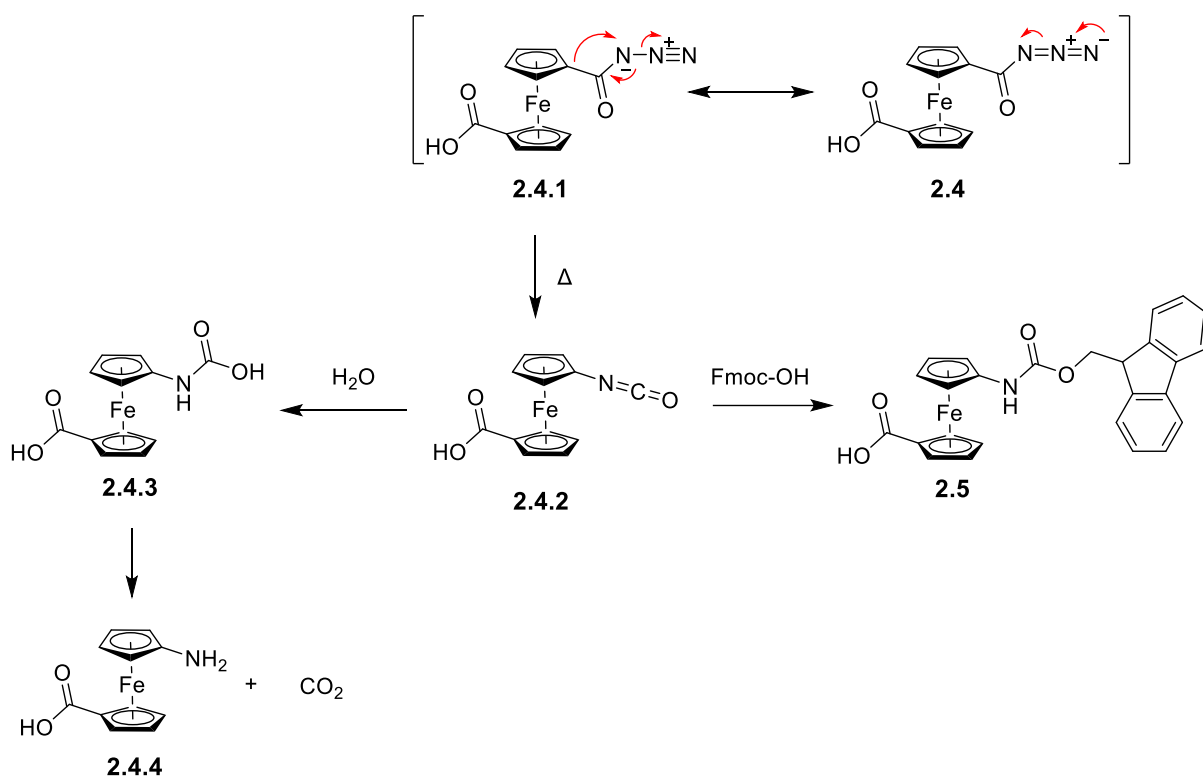
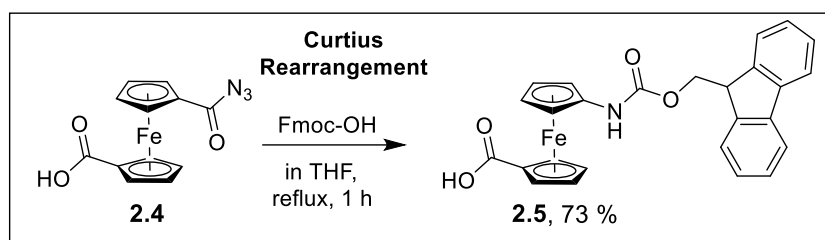


Scheme 33. Reaction scheme of the acyl azide **2.4**, followed by the Curtius rearrangement to form **2.5**.

Table 4. Investigation of whether purification of the DPPA contaminant from crude **2.4** improves yield of **2.5**

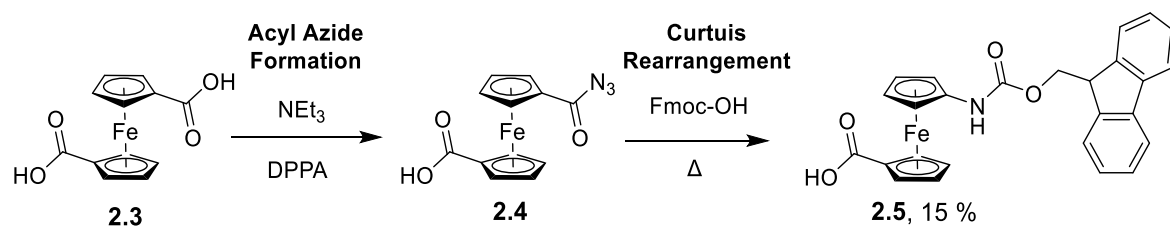
DPPA purified	Yield of <b>2.4</b>	Yield of <b>2.5</b>	Combined yield
Y	15 %	22 %	3 %
N	11 %	86 %	9 %

After acyl azide **2.4** was formed, the Curtius rearrangement was undertaken to form carbamate **2.5**, (Scheme 34). Originally, the reaction took place in solvents which had not been pre-dried, and no product was obtained. However, when anhydrous solvents were used, the product could be obtained in yields of 86 %. The original low yield was therefore likely due to the reaction of the unstable isocyanate intermediate, **2.4.2** reacting with water to form **2.4.4**.<sup>114</sup> A one step reaction (combining formation of **2.4** and then the Curtius rearrangement) was not attempted, as the presence of **2.6** (Scheme 32) in the reaction mixture for the Curtius rearrangement was reported by Erb *et al.*,<sup>113</sup> to have a detrimental effect on the yield.



*Scheme 34. The Curtius rearrangement of **2.4** upon heating and trapping with Fmoc-OH to form **2.5** or trapping with water to form **2.4.3** and **2.4.4***

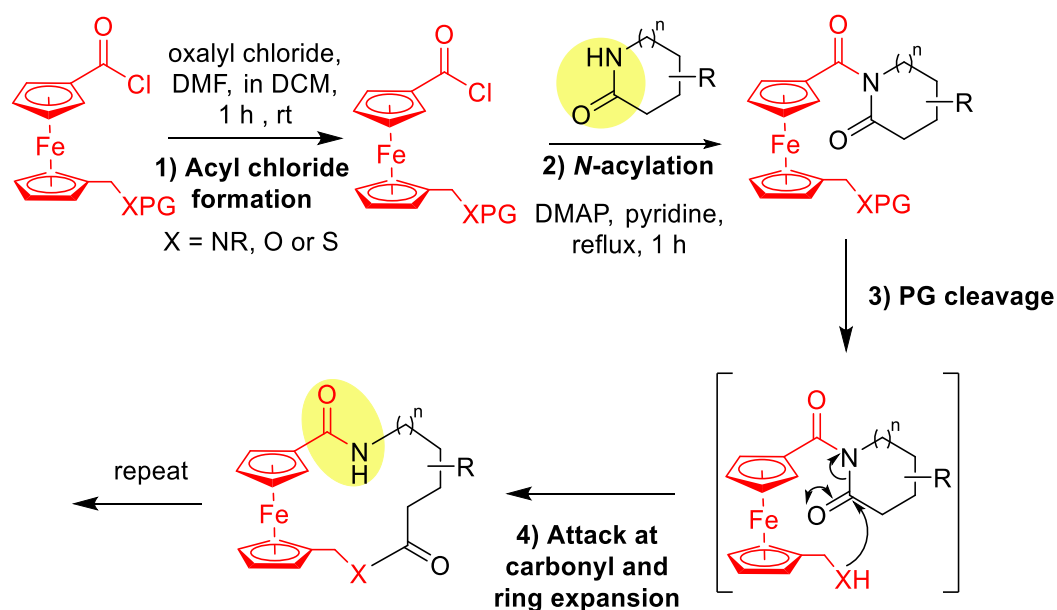
The combination of the carboxylic acid on one Cp ring and the Fmoc protected amine on the other makes **2.5** a good starting material for use in SuRE and it was produced in high enough yields to test the SuRE reaction using the synthetic pathway explored later in this chapter. Some synthetic problems were encountered, but nonetheless the desired product **2.5** was obtained, albeit with a relatively low yield of 15 % overall from **2.3** (scheme 35). The sequence is not very cost-effective as the cost of **2.3** is around £200 for 5 g and unfortunately its synthesis from **2.2** was unreliable in our hands. It was therefore important to investigate other methods of creating a ferrocene-starting material for use in SuRE to not only improve yield and cost-efficiency but also allow the investigation of different functional groups for implementation into SuRE.



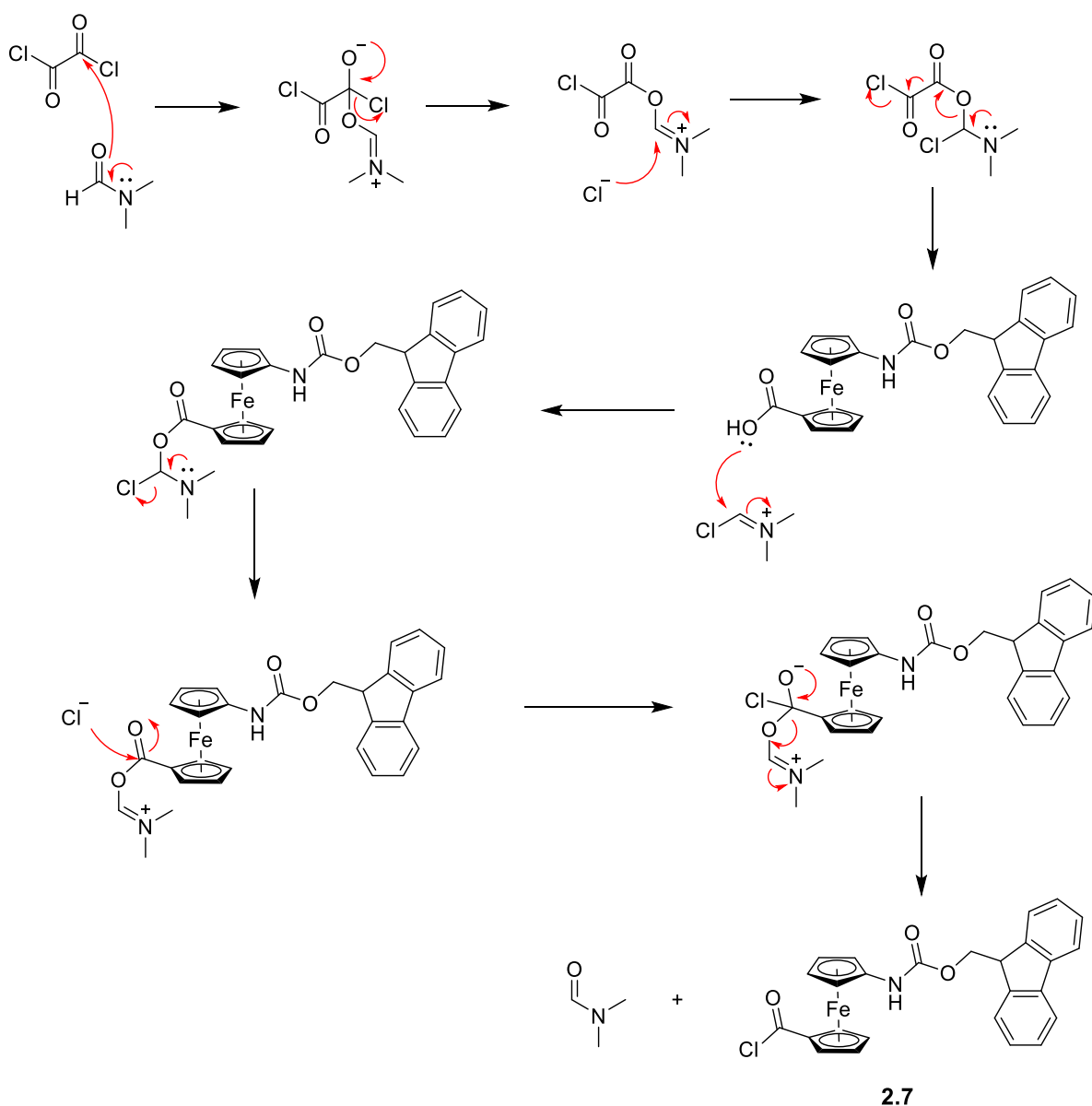
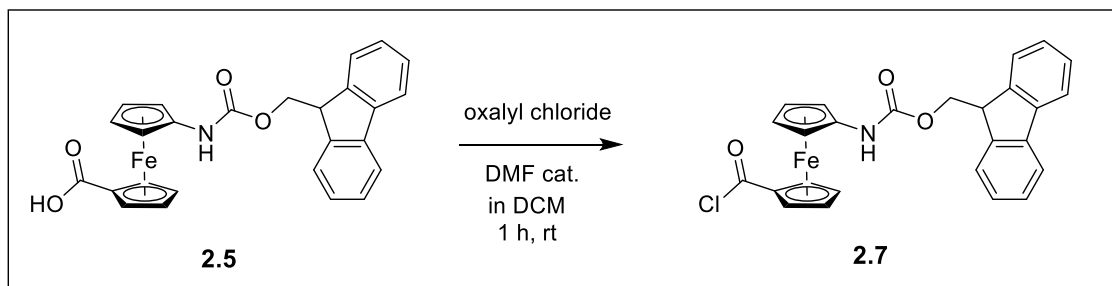
Scheme 35. Final synthetic method resulting in 15 % yield for **2.5** from **2.3** across a 2-step pathway.

### 3. SuRE: Acyl Chloride Formation

The first step of SuRE is the formation of an acyl chloride which is then taken straight on to the *N*-acylation step (Scheme 36, step 1&2). To test this step, **2.5** was converted into **2.7** by reaction using oxalyl chloride, and DMF as a nucleophilic catalyst (Scheme 37). The oxalyl chloride was then removed *in vacuo* and the product was analysed by IR and <sup>1</sup>H NMR spectroscopy (dry DMSO-*D*<sub>6</sub>). A change in the IR spectrum was observed from two carbonyl stretching frequencies at 1670 and 1698 cm<sup>-1</sup> in the acid starting material, to a single band at 1703 cm<sup>-1</sup> in the reaction product. This is consistent with the IR spectrum expected for an acid chloride, although the frequencies for conjugated acid halides are usually higher and normally fall between 1800-1770 cm<sup>-1</sup>. Significantly, the absorption band for chlorocarbonyl ferrocene falls at 1765 cm<sup>-1</sup>.<sup>115,116</sup> In the <sup>1</sup>H NMR spectrum, the disappearance of the **2.5** peak at 12.02 ppm was observed, indicating that the product no longer contained a carboxylic acid proton, however there was very little change observed in the remaining peaks vs. the starting material, which is to be expected.



Scheme 36. General SuRE methodology using a ferrocene-starting material. PG= protecting group, DMAP.

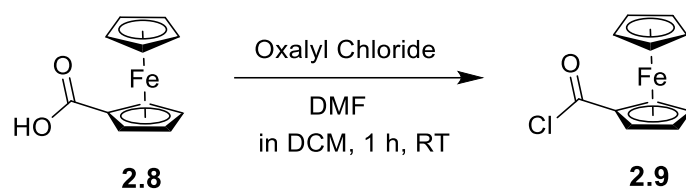


Scheme 37. conversion of **2.5** into **2.7** by the action of oxalyl chloride and DMF.

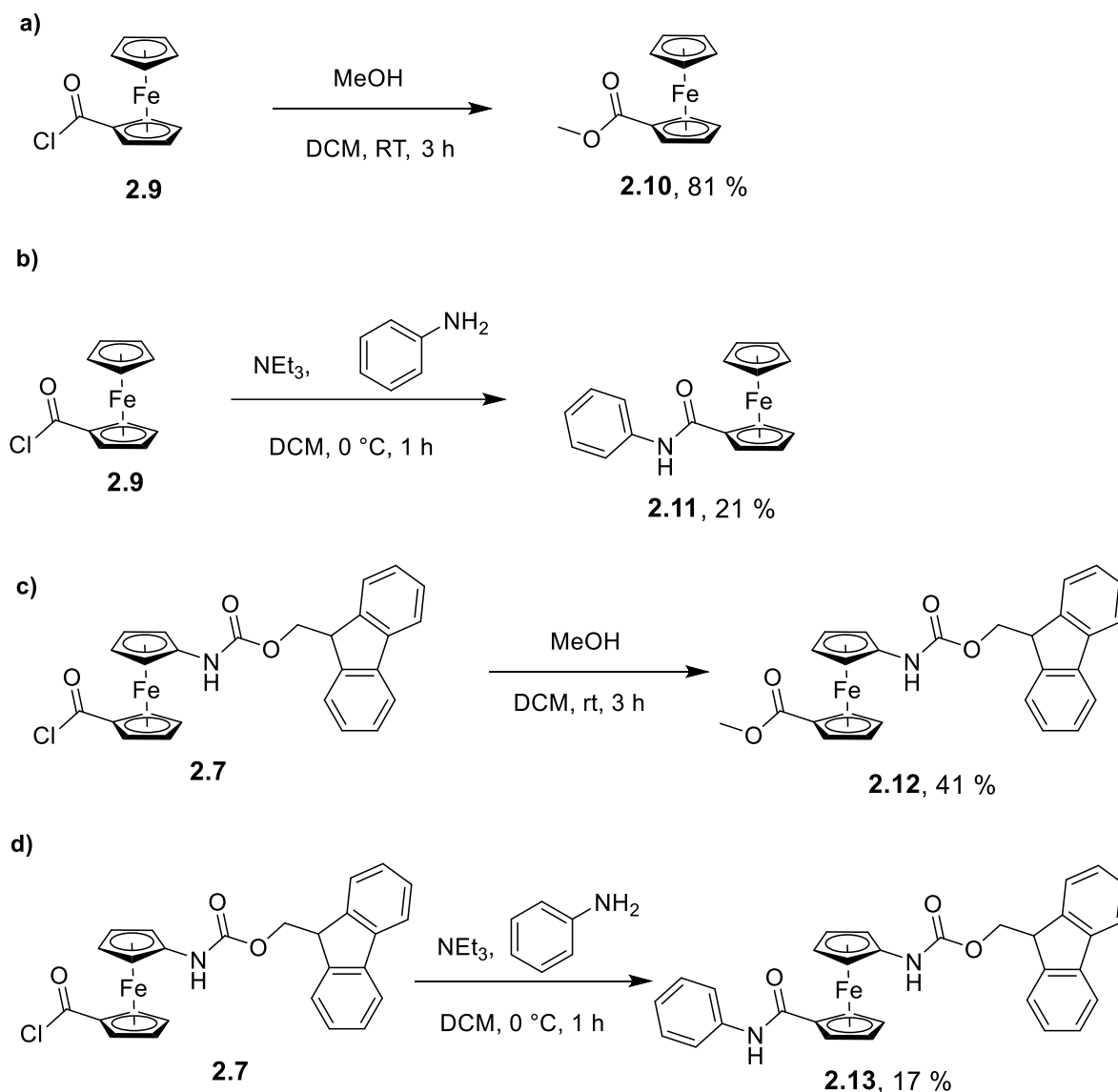
The reactive nature of acid chlorides results in considerable challenges when isolating and analysing them. Therefore, to better confirm a successful synthesis of the acid chloride, it was decided to try trapping it *in situ* through reaction with nucleophiles to form more stable products

that can more easily be isolated and analysed (Scheme 39). Our first attempt was undertaken using methanol, to form a methyl ester, and a second reaction was also performed with an amine (aniline).<sup>117</sup> The reaction of the acid-chloride with methanol was performed under neutral conditions at room temperature. The amide quench was also performed at RT, as such conditions are generally easily sufficient to promote amine acid chloride coupling.

Both of these tests were performed first using simpler acid chloride **2.9**, which was formed from **2.8** (Scheme 38), by the same method described earlier used to make **2.7**. Acid chloride **2.9** was used to test whether the nucleophilic substitution reaction conditions were being applied correctly and also if the “quenches” were viable on similar ferrocene species. Both reactions resulted in the successful synthesis of their ester and amide products **2.10** and **2.11** respectively (Scheme 39a,b) as confirmed by ESI-MS and <sup>1</sup>H NMR spectroscopy which matched literature findings,<sup>118,119</sup> in yields of 81 % and 21 % respectively. Minor side products were removed by column chromatography and recrystallisation methods. These tests showed that the acid chloride forming reaction conditions and nucleophilic substitution reactions were successful on this simple model system.



Scheme 38. Synthesis of **2.9** from **2.8** using oxalyl chloride in and DMF.



Scheme 39. Trapping of ferrocene acyl-chlorides. a) Trapping of **2.9** with methanol, b) Trapping of **2.9** with aniline c) Trapping of **2.7** with methanol, d) Trapping of **2.7** with aniline.

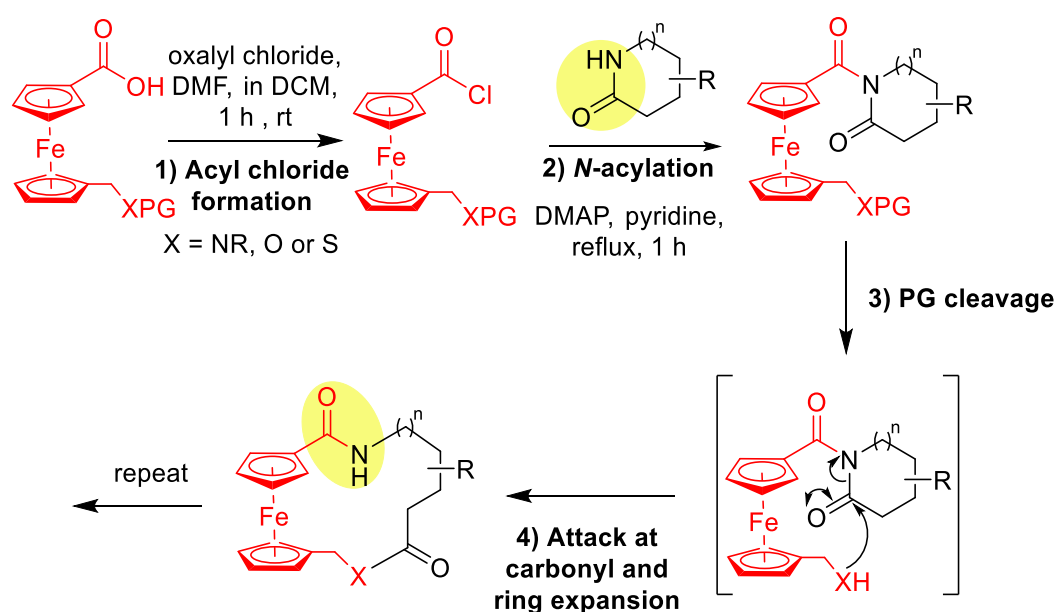
The nucleophilic substitution tests were then attempted on the real system, using Fmoc derivative **2.7** (Scheme 39 c,d). Pleasingly, **2.12** and **2.13** were both successfully isolated as identified by  $^1\text{H}$  NMR and IR spectroscopy and ESI-MS. However, a significant amount of decomposition was also observed here, with yields of 41 % and 17 % respectively obtained for **2.12** and **2.13** respectively.

Since the products of both reactions were successfully obtained, it was concluded that acyl chloride formation had been achieved and this provided confidence that the acid chloride product **2.7** could be used in the following *N*-acylation reactions towards SuRE without being isolated first. The modest yields are likely due in part, to decomposition of the acyl chloride, and in the case of the esterification reaction, may have been due to stopping the reaction before completion (as followed by TLC).

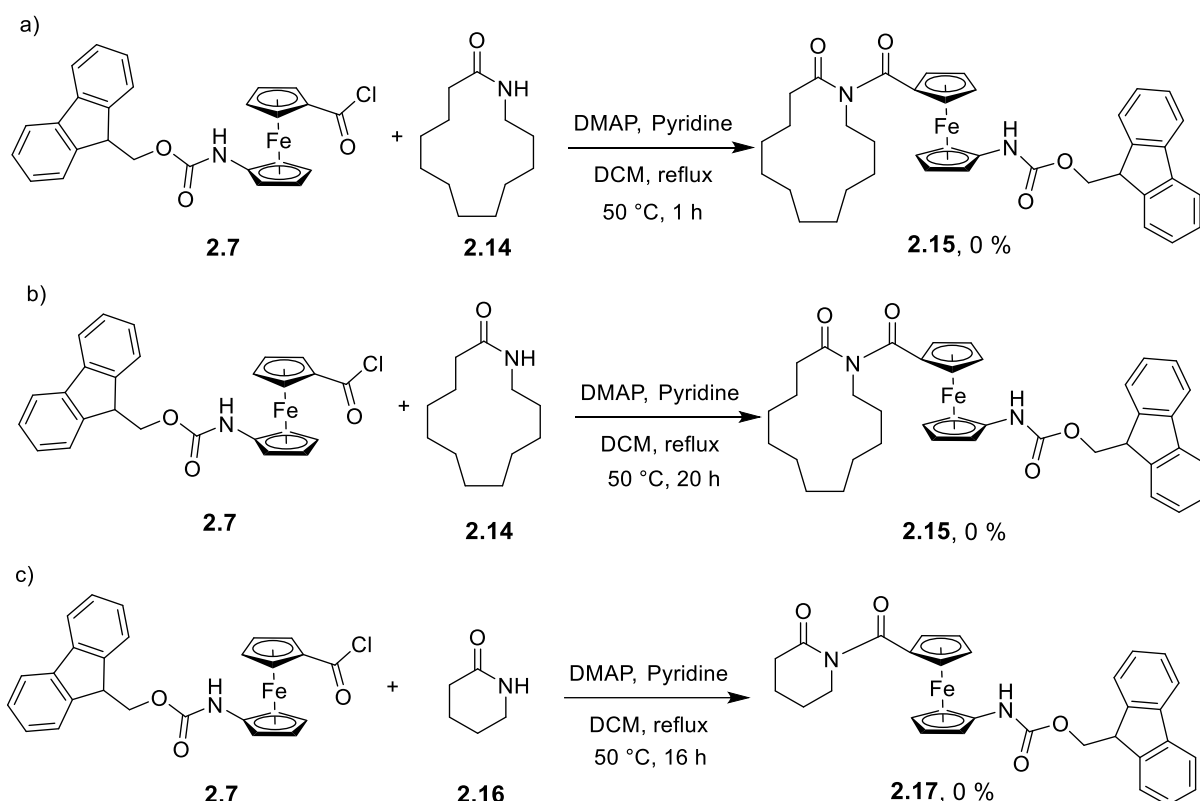
## 4. SuRE: *N*-acylation

### 4.1 General *N*-acylation Conditions

The standard procedure for *N*-acylation in SuRE involves the generation of an acyl chloride (Scheme 40, step 1), followed by the addition of freshly prepared acid chloride into a solution of lactam, pyridine and DMAP, to form an intermediate imide (Scheme 40, step 2) e.g. **2.15** and **2.17**, showed in Scheme 41.<sup>120</sup> These conditions were first attempted with the 13-membered ring lauro lactam **2.14** using DMAP and pyridine as the base and nucleophilic catalyst respectively, in DCM and heating to reflux. The reaction was monitored by TLC and after 1 hour a new TLC spot had appeared indicating the formation of a new product. The reaction was therefore quenched with 1 M aq. HCl and the organic-soluble products were isolated. However, analysis by both <sup>1</sup>H NMR spectroscopy and ESI-MS indicated that **2.15** had not been formed (Scheme 41 c). Next, the reaction was repeated but with a longer reaction time, stirring at reflux overnight (Scheme 41 b), as is typically done in Unsworth group's published methods, but again the desired product **2.15** was not obtained. Finally, *N*-acylation of a smaller, 6-membered lactam **2.16** (Scheme 41 c) was attempted since the nitrogen lone pair in smaller lactams tends to be less well conjugated into the carbonyl,<sup>121</sup> thus making them more nucleophilic and hence more reactive to *N*-acylation.<sup>122</sup> However, this was also unsuccessful, with none of the desired product imide **2.17** obtained.

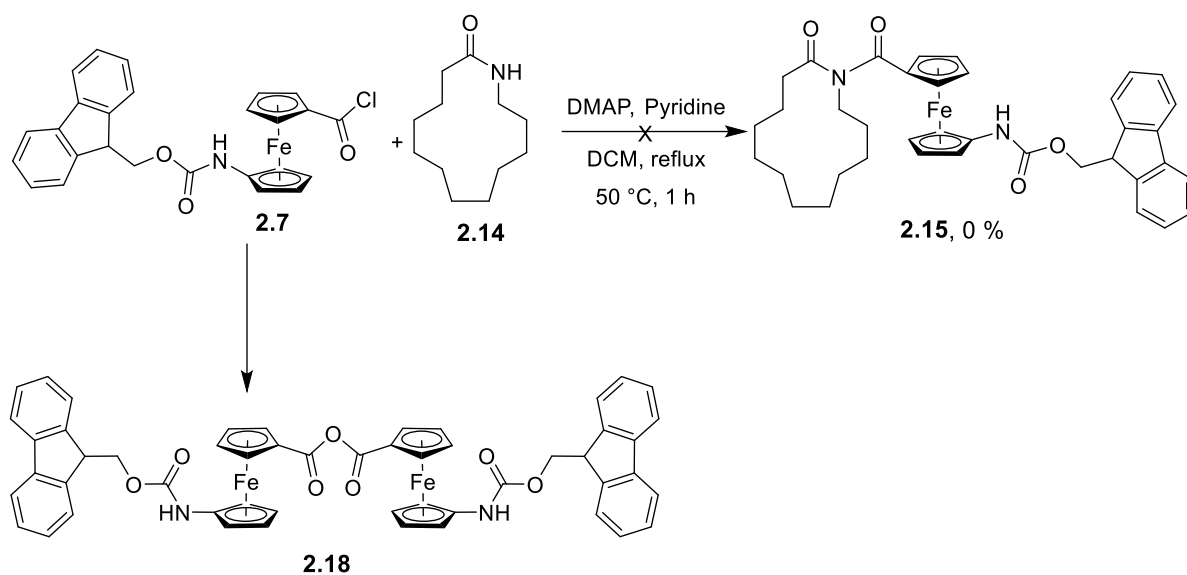


Scheme 40. General scheme for SuRE using a ferrocene-containing starting material. PG = protecting group, DMAP = 4-Dimethylaminopyridine



**Scheme 41.** Attempts at the *N*-acylation step of SuRE. a) Using 13-membered lactam and stirring for 1 h; b) using 13-membered lactam and stirring for 12 h; c) using a 6-membered lactam and stirring for 16 h.

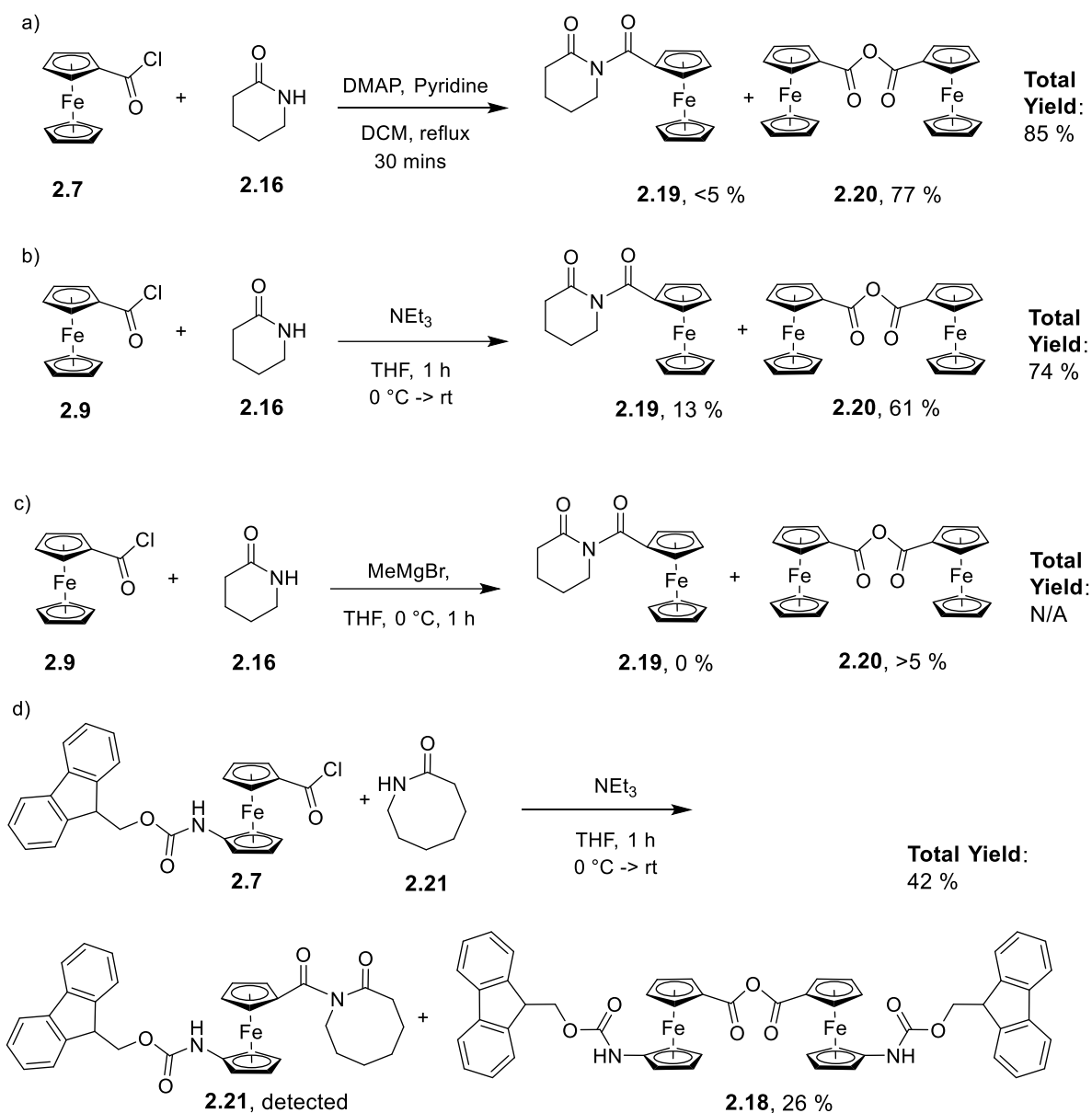
The newly formed spot, indicating by-product formation; was of interest however. Therefore, this by-product was isolated, and was identified as being an acid anhydride side-product **2.18** (Scheme 42). Acid anhydrides are common side-products formed during both acyl chloride and amide formation reaction and therefore may have formed in either step;<sup>123,124</sup> however the lack of a spot on the TLC plate corresponding to this species after acid chloride formation indicated that it most likely formed during the attempted *N*-acylation step. It is likely that anhydride formation is caused by reaction of acyl chloride intermediates with the carboxylic acid starting material, either present in the mixture either due to the acyl chloride formation not going to completion, or formed *in situ* by adventitious moisture. Aliquots taken for TLC analysis after stirring the reaction under reflux for just 10 minutes indicated that formation of **2.18** happens quickly and apparently occurs at a faster rate than *N*-acylation. It should also be noted that **2.18** can also undergo amide forming reactions,<sup>125</sup> and may have served as a synthetic equivalent to the acid chloride, but it did not appear to react with the lactam in this case, which is not too surprising, given that anhydrides are less electrophilic and therefore poorer acylating agents than acyl chlorides.<sup>123</sup>



Scheme 42. Formation of acid anhydride by-product **2.18** in place of the intended imide **2.15**

#### 4.2 Alternative *N*-acylation Conditions

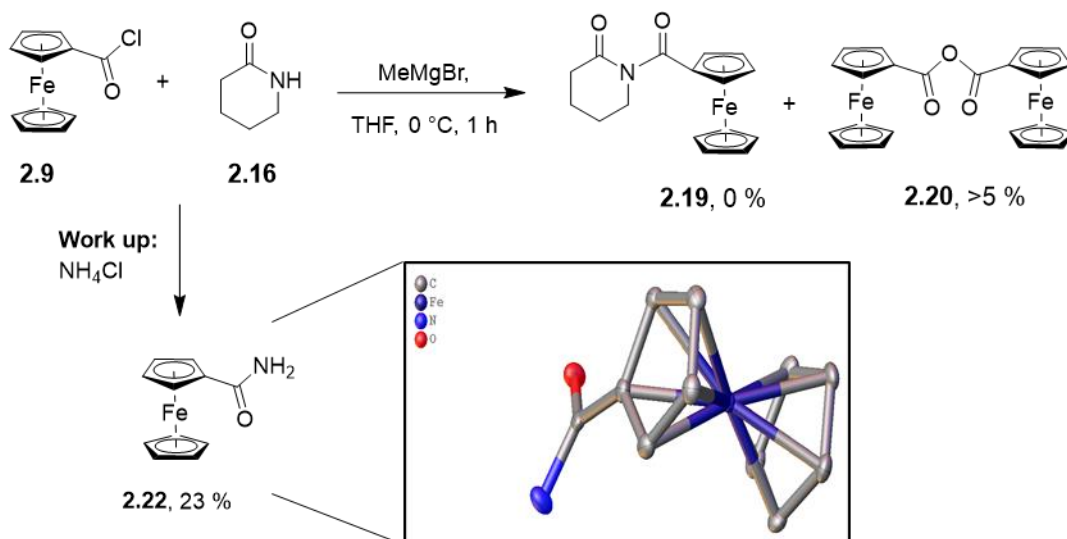
The formation of acid anhydride side-products was also encountered by Dr Palate (Unsworth Group) during previous work on SuRE chemistry.<sup>126</sup> To mitigate this problem, Dr Palate suggested some alternative *N*-acylation conditions which allowed the formation of previously challenging imides. These conditions were attempted using the acyl chloride **2.9** which is cheaper to synthesise than **2.7**. to investigate the plausibility of these methods with a ferrocene-based acylating agent (Scheme 43).



**Scheme 43.** Schemes showing the different *N*-acylation reagents tested and the product (**2.19**, **2.21**) and by-product (**2.20**, **2.18**) yields. a) reacting **2.9** with DMAP and pyridine; b) reacting **2.9** with  $\text{NEt}_3$  in THF first at 0 °C, then warming to room temperature; c) reacting **2.9** with  $\text{MeMgBr}$  d) reacting **2.7** with  $\text{NEt}_3$  in THF first at 0 °C, then warming to room temperature. Total yield = yield of starting material and products collected after reaction completion.

For comparison, a reaction was performed using the previously discussed methodology (DMAP, pyridine; Scheme 43a). Surprisingly, the novel *N*-acylated product **2.19** was isolated, although in very low yields and could not be purified. Next, the reaction was undertaken using  $\text{NEt}_3$  as the base (Scheme 43b) resulting in isolation of **2.19** in 13 % yield. Finally, deprotonation using the Grignard reagent  $\text{MeMgBr}$  was attempted, however only starting

material and amide **2.22** were obtained; likely from the reaction of **2.9** with ammonia, which presumably came from the  $\text{NH}_4\text{Cl}$  used to quench the reaction (Scheme 44). This suggested that the reaction of **2.9** with the lactam and acid chloride was incomplete when the reaction was quenched. The structure of **2.22** was confirmed unambiguously using XRD crystallography.

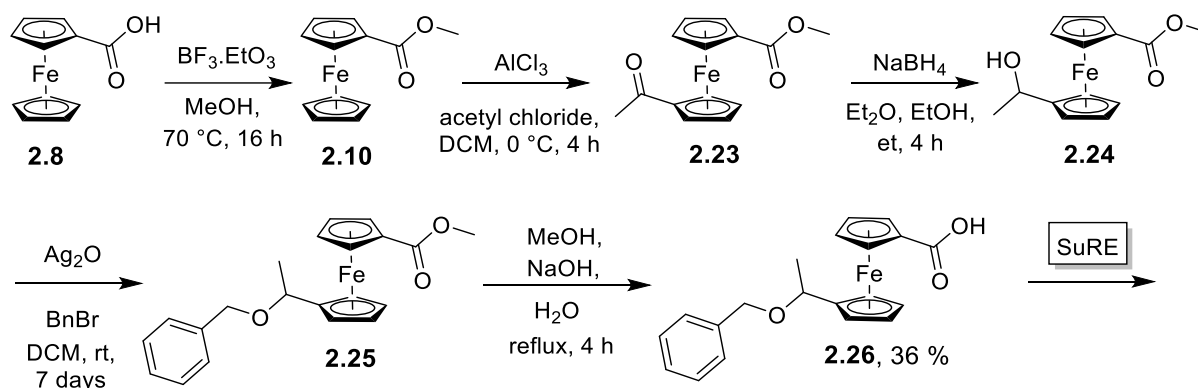


Scheme 44. Reaction of **2.9** with the work-up agent  $\text{NH}_4\text{Cl}$  to form **2.22**. XRD structure is also shown.

It was therefore concluded that use of  $\text{NEt}_3$  as a base was the most suitable reagent for *N*-acylation using a ferrocene-based acylating reagent. For this reason, the *N*-acylation using **2.5** was repeated with  $\text{NEt}_3$  as the reagent, however the imide product could only be detected by ESI-MS and could not be isolated. This suggests that the desired novel product had been formed, but if so, only in very low yields which were not adequate for continuing SuRE. Furthermore, reaction of the *N*-acylating agent **2.5** also resulted in far lower yields of the acid anhydride side-product **2.18**, indicating that functionalisation of the second Cp ring results in increased decomposition rates. This, combined with the favoured formation of acid anhydride side-products, resulted in the conclusion that **2.5** is too unstable for implementation into SuRE. This is likely due to the use of the carboxylic acid and subsequent acyl chloride being attached and directly conjugated to the Cp ring; these *N*-acylation methods tested have been shown to work well with simpler acid chloride reagents, strongly suggesting that Cp group is at least partly responsible for the different reactivity.

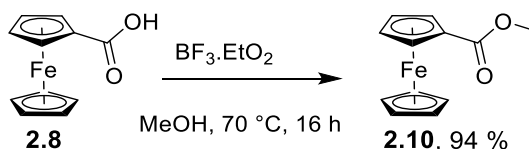
## 5. Synthesis of SuRE Starting Material 2.26

In previous SuRE studies different starting materials, particularly different protected nucleophiles have been more successful than others.<sup>58</sup> Due to this, and in the hope of expanding the scope of SuRE further, an alternative ferrocene-containing starting material including a benzyl protected alcohol was synthesised and investigated for use in SuRE. The proposed synthetic pathway for the second ferrocene-containing starting material for SuRE is shown in Scheme 45. The end **2.26** was successfully synthesised and isolated, as described in the following section. This section of work was undertaken in collaboration with a summer student in the Wilkinson and Unsworth groups', Oscar Schwabe.

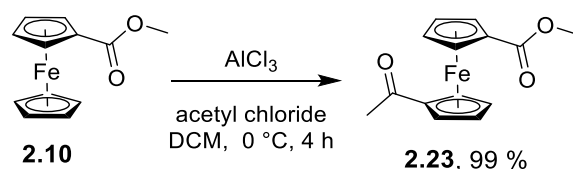


Scheme 45. Proposed synthetic pathway for **2.6**

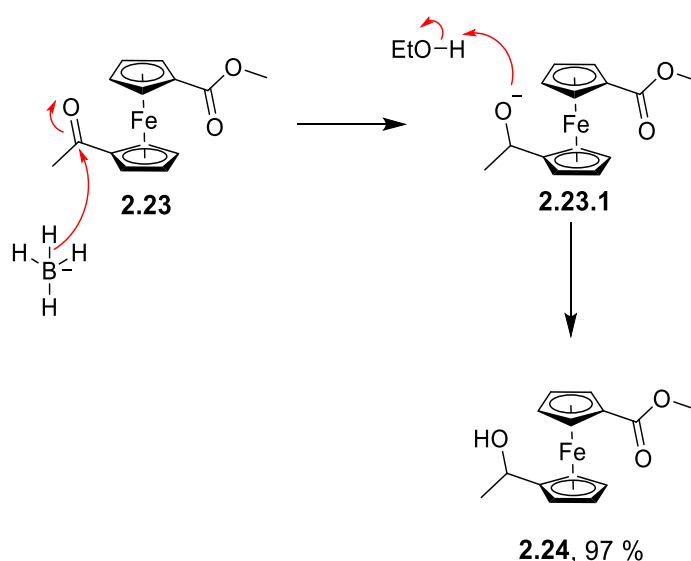
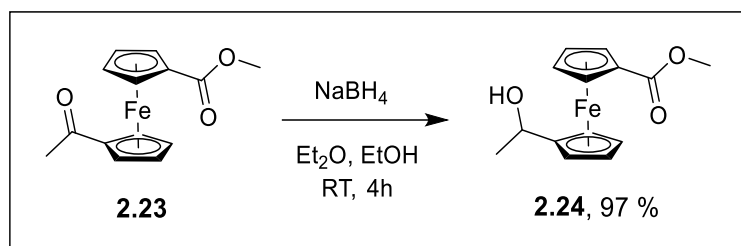
This synthetic route begins with **2.8** as the starting material. This is a far more affordable option in comparison to the di-acid, **2.3**, used for the previous synthetic route, making this synthesis more cost-efficient. **2.8** is then converted into **2.10** via a standard esterification reaction with  $\text{BF}_3 \cdot \text{EtO}_2$  as a Lewis acid catalyst in methanol, resulting in a 94 % yield of **2.10** (Scheme 46). A Friedel-Crafts acylation was then used to acylate the second Cp ring, producing **2.23** in 99 % yield (Scheme 47). The ketone was then reduced using  $\text{NaBH}_4$  yielding **2.24** in yields of 97 % (Scheme 48).



Scheme 46. Reaction scheme for the esterification of **2.8** to form **2.23**.

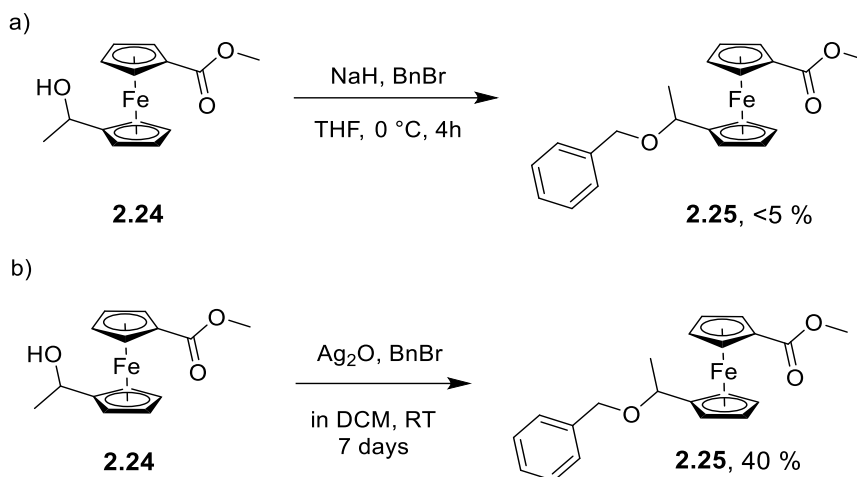


Scheme 47. Reaction scheme for the Friedel-Crafts acylation of **2.23** to form **2.24**.

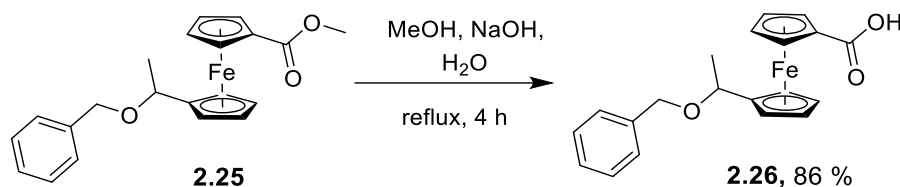


Scheme 48. Reaction scheme and mechanism for the reduction of **2.23** to form **2.24**.

Next, benzyl protection of the alcohol group to form **2.25** was attempted, first using benzyl bromide in combination with a NaH base; however this resulted in a yield of <5 % (Scheme 49a). Protection with a milder base, Ag<sub>2</sub>O, was attempted using the procedure outlined by Kovačević *et al.*<sup>127</sup> This method was successful, resulting in the isolation of **2.25** in 40 % yield (Scheme 49b). Finally, a standard ester hydrolysis was undertaken using a methanol and aq. NaOH solvent system, yielding the second novel, ferrocene-containing, starting material, **2.26** in 84 % yield (Scheme 50). The overall yield for this synthetic pathway was 31 % making it much higher yielding than the pathway used for the synthesis of *N*-Fmoc derivative **2.5**. As mentioned earlier it is also more cost-efficient, however the synthetic route has 5 steps and the alcohol protection step is run over 7 days making it less time efficient compared the synthesis of **2.5**, which has 2 steps and can be made from its starting material in under a day.

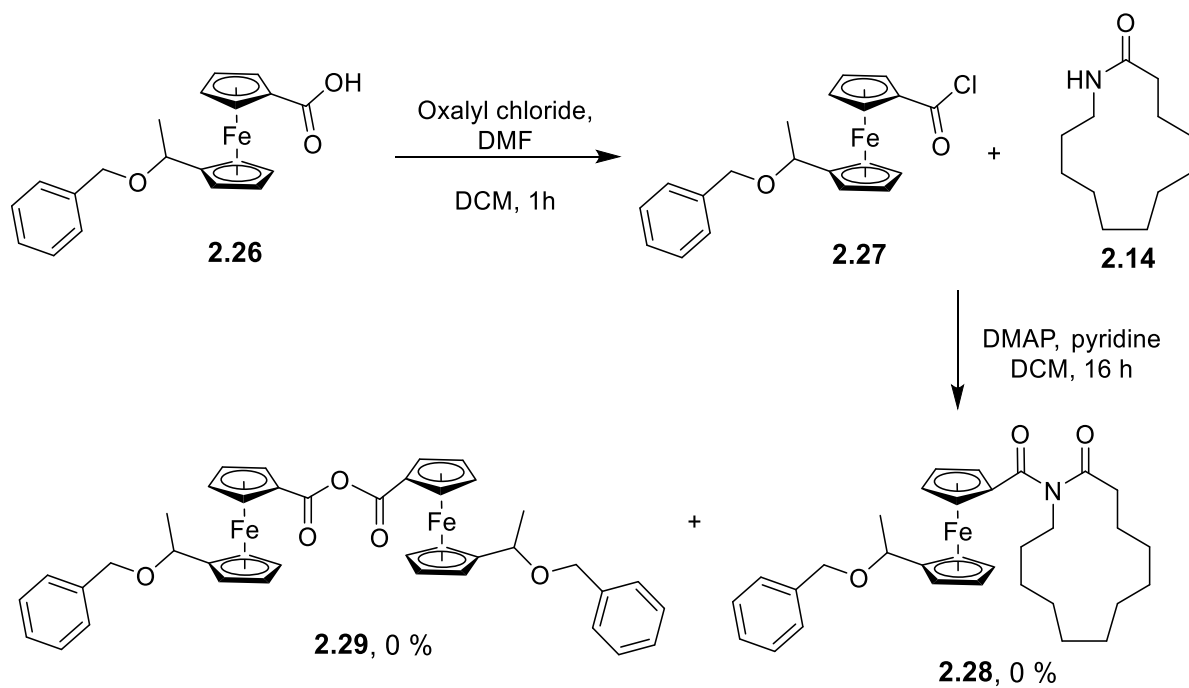


*Scheme 49. Reaction schemes for alcohol protection on of **2.24** to form **2.25**. a) using strong base, NaH and benzyl bromide and b) using milder base Ag<sub>2</sub>O and benzyl bromide.*



*Scheme 50. Reaction scheme for the ester hydrolysis of **2.23** to form **2.24**.*

The first steps in SuRE were then attempted using **2.26**. The acid chloride was synthesised using the same method described for **2.5**, it was then entered into the *N*-acylation step without isolation. The standard SuRE conditions for *N*-acylation were attempted (Scheme 51), however after stirring for 40 minutes no new spot was seen by TLC. Therefore, the reaction was left to stir overnight, however no evidence of the intended *N*-acylated product **2.28**, nor an acid anhydride side-product **2.29** could be detected by either TLC or ESI-MS. Furthermore, <sup>1</sup>H NMR spectroscopy (Figure 28) indicated decomposition of the ferrocene species, as indicated by the appearance a number of new, less intense peaks in the ferrocene region and appearance of new peaks in the aromatic region. It was therefore concluded that this starting material was also unstable to the *N*-acylation conditions. Other conditions were not attempted due to time constraints.



Scheme 51. Reaction scheme for the introduction of into SuRE.

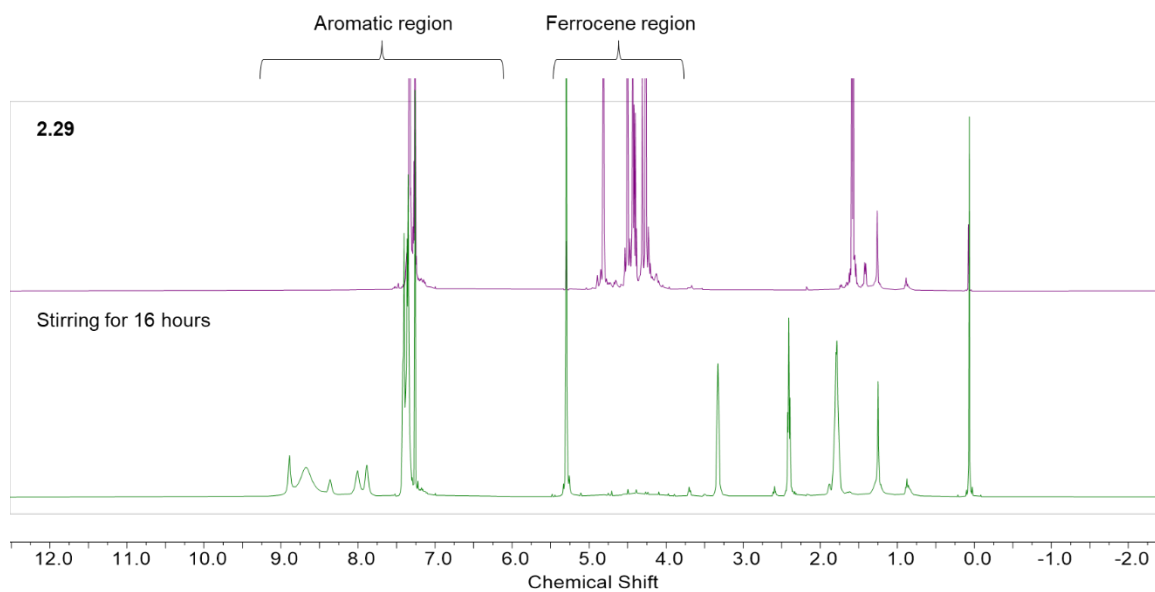


Figure 28. Shifting of peaks in the NMR spectra of **2.29** from the ferrocene region to the aromatic region of the NMR spectrum after stirring for 16 hours, indicating decomposition.

## 6. Electrochemistry & UV-Visible Spectroscopy

As discussed in the introduction, ferrocene displays optical and electrochemical properties of interest such as a mild one electron oxidation at + 0.4 V (vs. SCE) to its ferrocenium ion, resulting in a colour change from orange to blue (Figure 29). Substituting ferrocene with electron withdrawing or donating groups also allows alteration of the redox potential, with electron withdrawing substituents increasing redox potential and *vice versa*. Hence altering the UV-Visible spectra of the compound. This allows fine-tuning of ferrocenes for applications such as reducing agents.<sup>68</sup> Furthermore, the redox activity of ferrocene has been explored in more versatile applications such as for sensors,<sup>73,86</sup> in molecular electronics,<sup>74–76</sup> liquid crystals,<sup>77</sup> or in medicinal chemistry.<sup>78</sup>

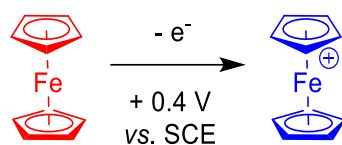


Figure 29. One electron oxidation of ferrocene to its ferrocenium ion. Colour change is from orange to blue. Oxidation occurs at +0.4 V vs. SCE.

In a ferrocene-containing macrocycle, it is unlikely that most of the ring will have a large impact on the redox and optical properties of the system (Figure 30). Therefore, the ferrocene moiety and the groups directly attached to it will likely dictate these properties. For this reason, it is advantageous to study the effects that different substituents have on the electrochemical and optical properties of the ferrocene core, to allow the prediction of the properties of potential ferrocene-containing macrocycles.

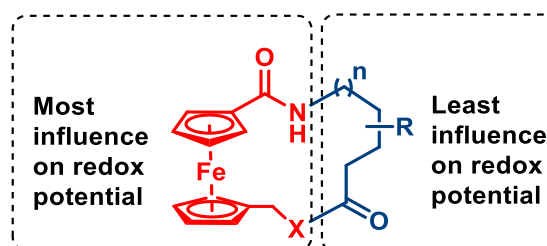


Figure 30. Diagram illustrating the regions of the macrocycle which will have the most impact on optical and redox properties of the entire macrocycle, with the most influential being functional groups directly attached to the ferrocene.

Computational calculations of the ferrocene species synthesised in this project were performed using DFT. Optimised geometries for compounds **Fc** and **2.1–2.6** were obtained using the B3LYP functional and the def2\_SVP basis set. These geometries were then used as the basis for single point calculations at a higher level of theory using the def2\_TZVP basis

set. From these “single point” calculations, the electronic structure of the compounds could be determined and trends in their properties elucidated.

Analysis of the frontier orbitals for these compounds (Figure 31 and in appendix) shows that HOMO in all cases is centred mostly around Fe and having d-orbital character, whereas the LUMOs tend to be ligand-based. Most of the compounds however do show some orbital mixing, with some HOMOs having slight ligand character and the LUMOs often having slight d orbital character. An example of this type of behaviour is illustrated by **2.4** in Figure 32a. In the case of **2.3** the LUMO appears completely delocalised (Figure 31b). The distribution of the HOMO orbitals remained very similar across the series, however the LUMO orbitals appear to become progressively more delocalised across the whole molecule as the substituents become more electron withdrawing (Figure 32).

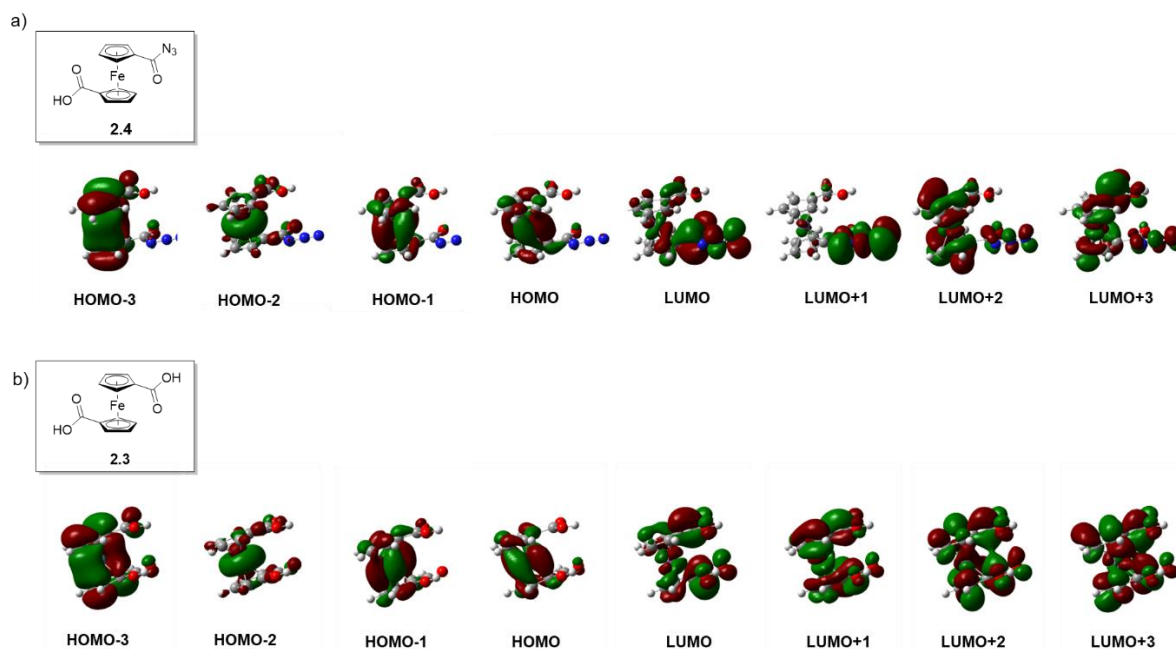


Figure 31. The frontier molecular orbitals HOMO-3 to LUMO+3 of a) **2.4** and b) **2.3** as calculated by DFT

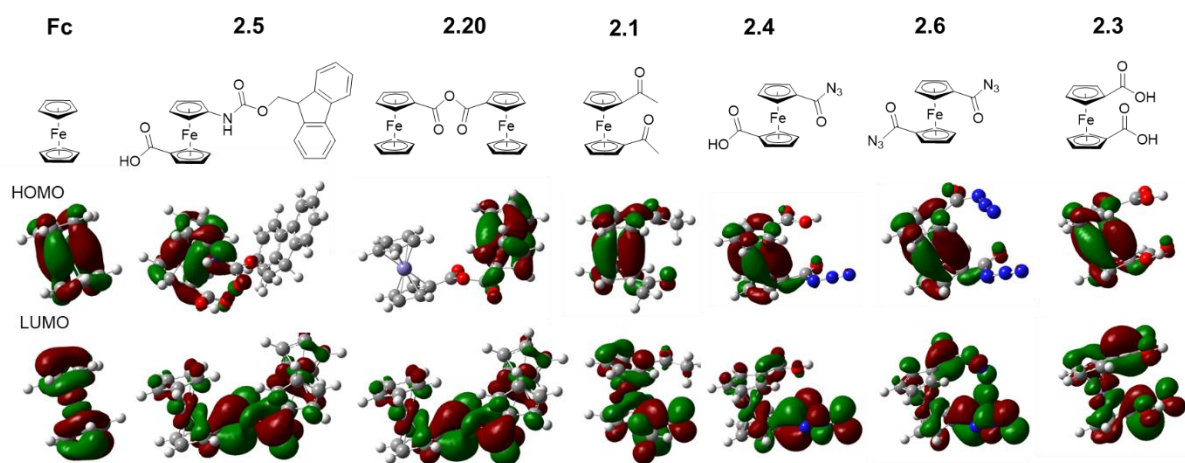


Figure 32. The HOMO and LUMO of compound Fc and 2.1-2.6 in order of electron withdrawing ability of the Cp ring substituents

The figures illustrating the frontier molecular orbitals for compounds **2.3** and **2.4** are listed in the appendix. The energies of the HOMO-3 to LUMO+3 orbitals are depicted in Figure 33 for each species and the HOMO for each species was estimated to be lower in energy than ferrocene. Since all substituents were electron withdrawing in nature, this indicates that addition of electron withdrawing substituents stabilises orbitals. It is therefore likely that addition of electron donating substituents would destabilise orbitals. This knowledge could help further inform the tuning of optical and electrochemical properties of ferrocene-containing macrocycles based on orbital stabilisation.

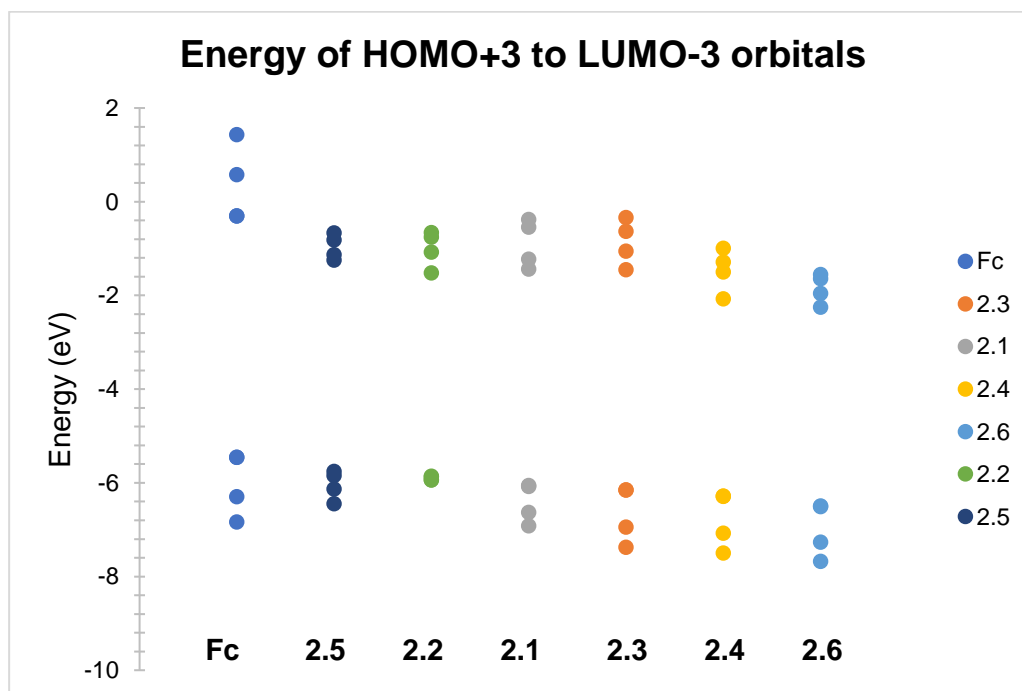


Figure 33. The energy of the frontier molecular orbitals (HOMO-3 to LUMO+3) for compounds **Fc** and **2.1-2.6** arranged from the highest to lowest energy HOMO.

The UV-Visible spectrum of each compound was collected in DCM. A representative spectrum (of **2.1**, **2.4**, **2.6** and **2.20**) is provided in Figure 34 and the data for all compounds are summarised in Table 5.

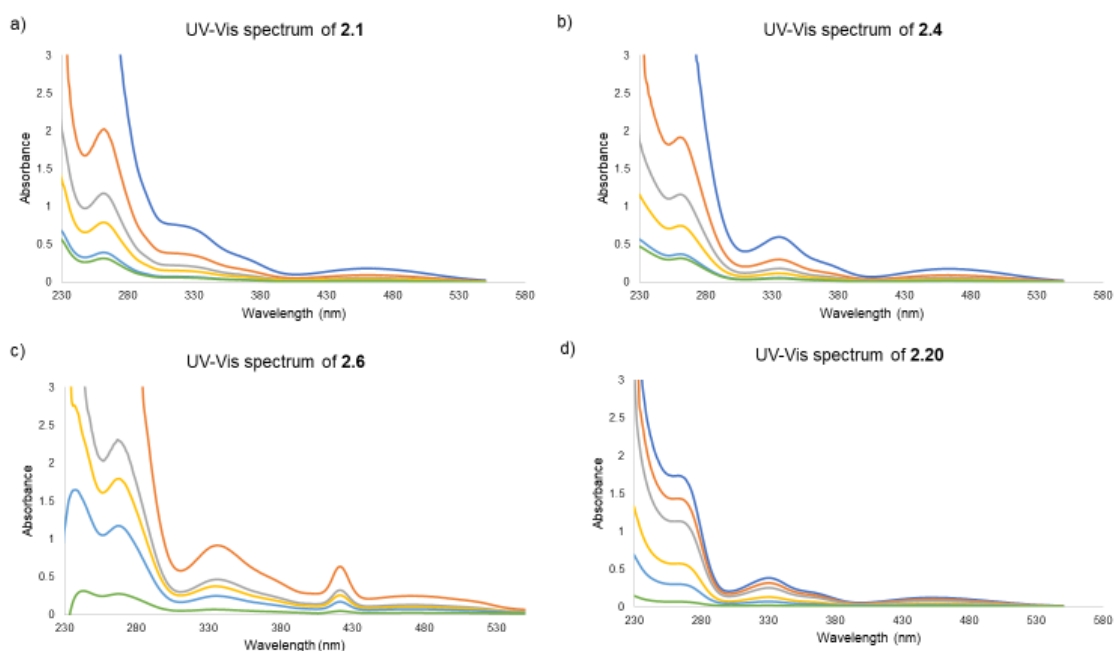


Figure 34. UV-Visible spectrum of compounds **2.1** at concentrations  $4.1 \times 10^{-4}$ ,  $2.0 \times 10^{-4}$ ,  $1.2 \times 10^{-5}$ ,  $8.1 \times 10^{-6}$ ,  $4.1 \times 10^{-7}$  and  $3.3 \times 10^{-8}$  **2.4** at concentrations  $3.3 \times 10^{-4}$ ,  $1.7 \times 10^{-4}$ ,  $1.0 \times 10^{-4}$ ,  $6.7 \times 10^{-5}$ ,  $3.3 \times 10^{-5}$ ,  $3.3 \times 10^{-5}$ ,  $2.7 \times 10^{-5}$ ; **2.6** at concentrations  $3.0 \times 10^{-4}$ ,  $1.5 \times 10^{-4}$ ,  $1.2 \times 10^{-4}$ ,  $7.4 \times 10^{-5}$ ,  $1.5 \times 10^{-5}$ ; **2.20** at concentrations  $2.8 \times 10^{-4}$ ,  $2.3 \times 10^{-4}$ ,  $1.8 \times 10^{-4}$ ,  $9.1 \times 10^{-5}$ ,  $4.5 \times 10^{-5}$  and  $3.6 \times 10^{-5}$  M.

Table 5. Table of the wavelengths of MLCT and  $\pi$ - $\pi^*$  transfer bands of compounds **2.1**, **2.4**, **2.6**, **2.19** and **2.20**.

Compound	MLCT Band, nm ( $\epsilon$ , L mol <sup>-1</sup> cm <sup>-1</sup> )	$\pi$ - $\pi^*$ Band, nm ( $\epsilon$ , L mol <sup>-1</sup> cm <sup>-1</sup> )
<b>2.6</b>	421 (2012)	337 (2999)
<b>2.20</b>	453 (440)	330 (1413)
<b>2.19</b>	459 (465)	343 (1188)
<b>2.1</b>	462 (438)	320 (1841)
<b>2.4</b>	463 (521)	335 (1792)

The dominant transition for each compounds is a band at around 420–460 nm which the literature suggests is the HOMO→LUMO transition, and from the calculations, this suggests that the transition in each case can be described as largely MLCT in nature.<sup>128</sup> The lowest energy transition in UV-Visible was also similar in all compounds and ranged from 421 nm ( $\epsilon = 2012$  L mol<sup>-1</sup> cm<sup>-1</sup>) to 463 nm ( $\epsilon = 521$  L mol<sup>-1</sup> cm<sup>-1</sup>). These transitions were seen as broad bands, except for **2.6** which exhibited a sharp band in this area. The compounds measured

also all exhibited broad bands ranging from 320 nm ( $\epsilon = 1841 \text{ L mol}^{-1} \text{ cm}^{-1}$ ) to 343 nm ( $\epsilon = 1188 \text{ L mol}^{-1} \text{ cm}^{-1}$ ) which in, similar compounds in the literature have been associated with  $\pi \rightarrow \pi^*$  transitions primarily on the Cp substituent or from transitions which are delocalised throughout the molecule.<sup>129</sup> Other bands occurring at lower wavelengths can be attributed to higher energy transitions of the  $\pi \rightarrow \pi^*$  type and are likely associated with the Cp rings and their substituents, and may be due to inter-ligand charge transfer.<sup>128,129</sup>

All substituted compounds were estimated by DFT to have a smaller HOMO-LUMO gap ranging from 4.21 eV (249 nm) to 4.70 eV (264 nm) compared to ferrocene which was estimated to be 5.15 eV (241 nm). These are far smaller than the values observed for UV-Visible and those predicted from the literature, this is likely due to the DFT calculations overestimating absolute values, something which is common when using DFT calculations. It should be noted however, that there was no correlation found between band gap and the equivalent HOMO  $\rightarrow$  LUMO transition observed by UV-Visible, although this is likely to be due to this absorbance band being the result of multiple transitions, therefore obscuring the trend. To obtain a better understanding of the absorption spectra, time-dependent DFT calculations would be required, however this was not possible within the timescale of the project.

Compounds **2.1**, **2.4–2.6**, **2.19** and **2.20** were also analysed by CV using a 0.1 M  $[\text{n-Bu}_4][\text{PF}_6]$  solution in  $\text{CH}_2\text{Cl}_2$  as the supporting electrolyte. All potentials are reported vs. the  $\text{Fc}/\text{Fc}^+$  redox couple and have been corrected for solution resistance effects ( $R_s$ ) using  $R_s$  values estimated from AC impedance spectroscopy.<sup>130</sup> Electrochemical analysis of **2.3** was not undertaken due to its poor solubility in common solvents. Figure 35 shows the electrochemical analysis of **2.20** as an illustrative example. All compounds exhibited a one electron oxidation, corresponding to the  $\text{Fc}/\text{Fc}^+$  redox couple and were found to be chemically reversible ( $i_{pa}/i_{pc} \sim 1$ ). However, some compounds had a  $\Delta E_p > 100 \text{ mV}$ , and all compounds showed slight increases in  $\Delta E_p$  with scan rate, thereby indicating some electrochemical irreversibility. Electrochemical data are reported in Table 6.

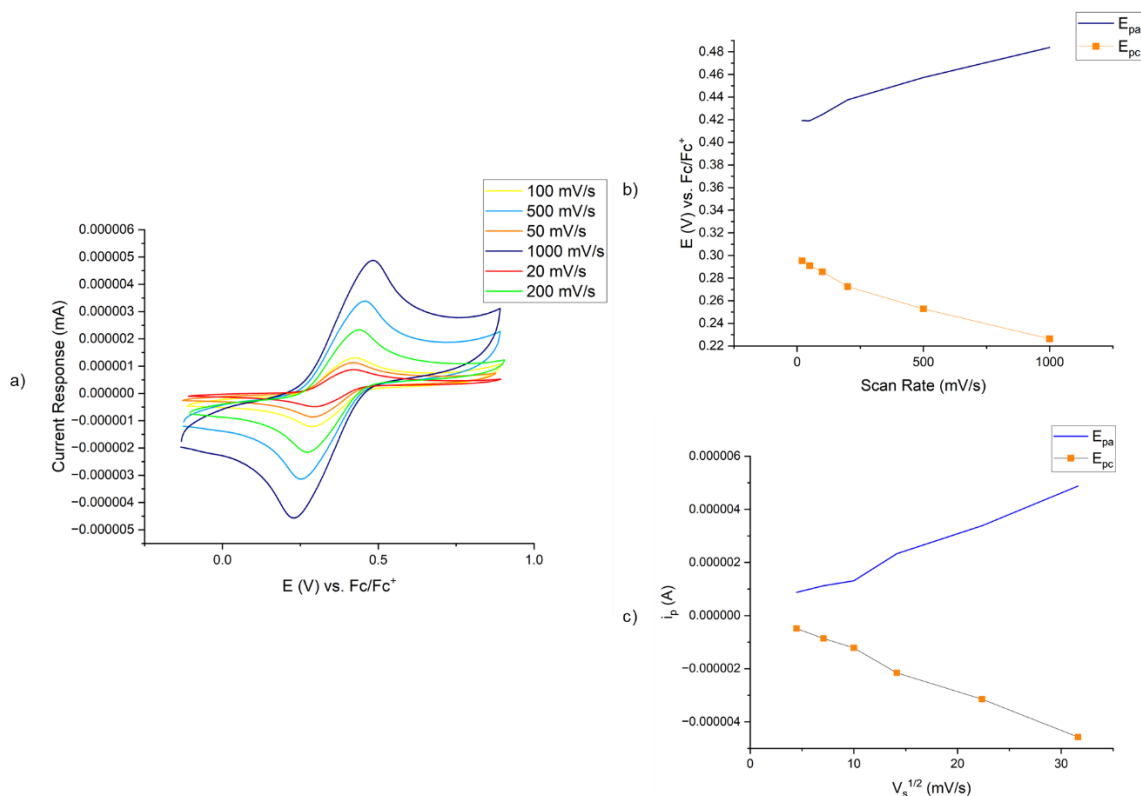


Figure 35. Electrochemical analysis of **2.20**. a) cyclic voltammogram at different scan rates; b) Scan rate dependence vs. voltage; c) current vs. the square root of scan rate.

Table 6. Electrochemical analysis of compounds **2.1**, **2.4-2.6**, **2.19** and **2.20** including  $E_{pa}$  and  $E_{pc}$  along with calculated values of  $\Delta E_p$ ,  $E_{1/2}$  and  $i_{pa}/i_{pc}$ .

Name	$E_{pa}$	$E_{pc}$	$\Delta E_p$	$E_{1/2}$	$i_{pa}/i_{pc}$
<b>2.5</b>	193	69	124	131	-0.817
<b>2.4</b>	721	389	331	555	-1.188
<b>2.19</b>	-796	-886	89	-841	-1.021
<b>2.20</b>	425	286	139	355	-0.954
<b>2.6</b>	652	568	84	610	1.253
<b>2.1</b>	493	402	91	447	-1.052

Gratifyingly, the trend in  $E_{1/2}$  values is reflected in the trend in the calculated HOMO energies of the compounds with the lowest energy HOMO requiring the highest potential to oxidise. This is due to the variation of electron withdrawing ability of the substituents, where compounds with more electron withdrawing substituents (*i.e.* acylazides) will be more stabilised to oxidation. As can be seen from Figure 36, the trend in  $E_{1/2}$  is almost linear,

indicating a potential free-energy relationship across the series. This observation could inform as to which ferrocene substituents to include in a macrocycle based on the intended  $E_{1/2}$  value.

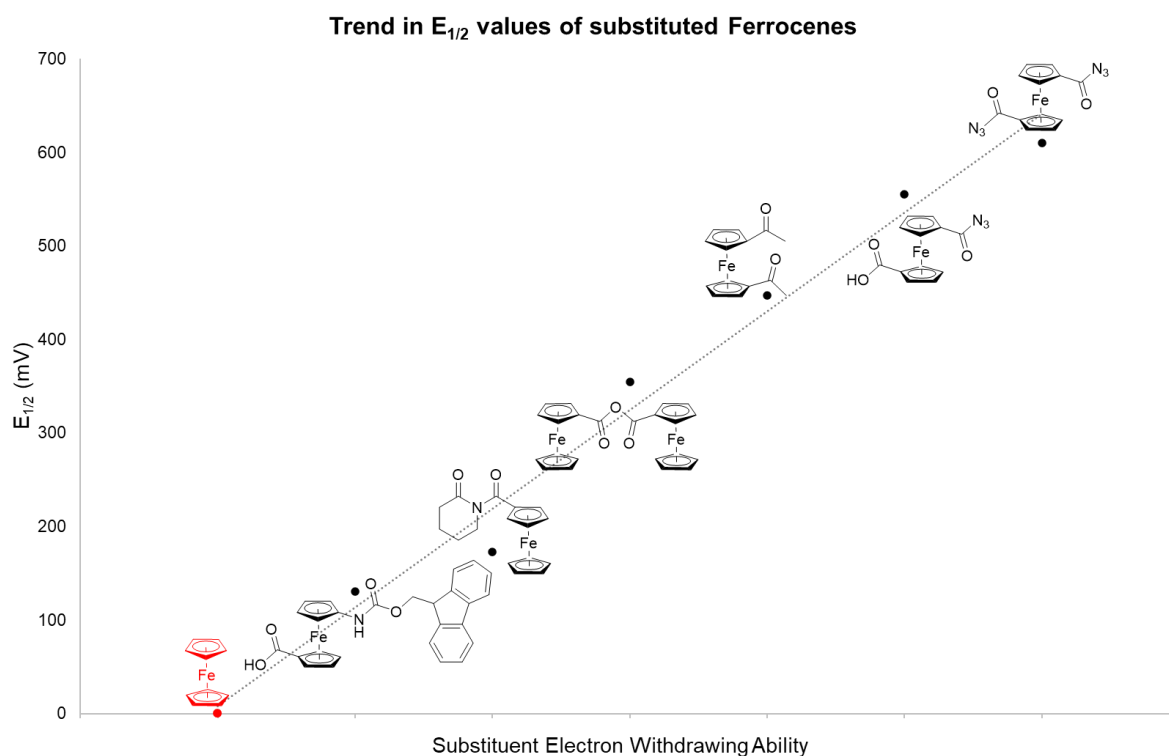


Figure 36. Graph of  $E_{1/2}$  values of compounds **2.1-2.6**, **2.19** and **2.20**

XRD analysis of **2.5** found that in DCM, **2.5** was a dimer connected by hydrogen bonds (Figure 37a) between the acid and amide groups. Due to this, the potential for this species to exhibit proton-coupled mixed valency (resulting from communication across the hydrogen bonds) was explored.<sup>131-133</sup> When analysed by CV only one oxidation peak could be observed, rather than the anticipated two. However, this redox process was relatively broad, which may be the result of two oxidation peaks at very similar oxidation potentials (Figure 37b). A follow-up experiment employing differential pulse voltammetry may provide more information about any potential peak separation.

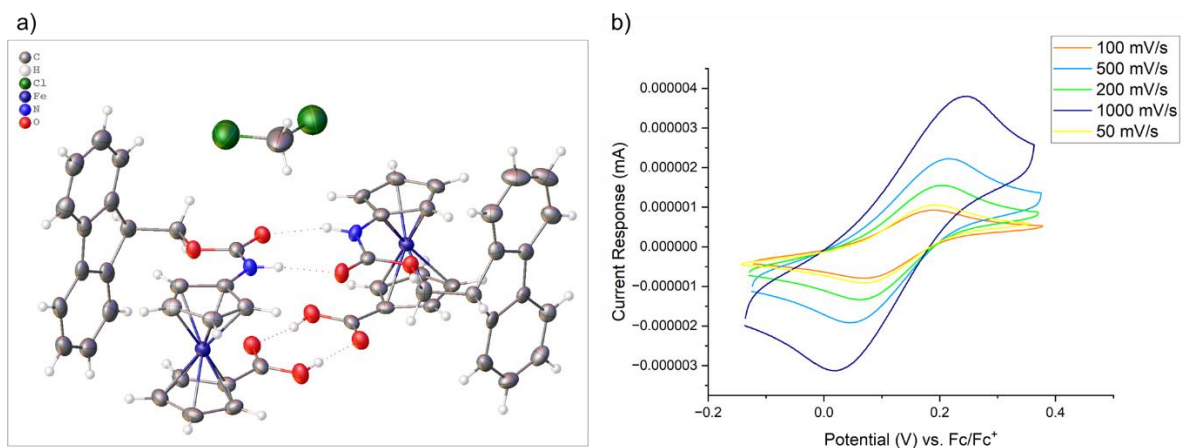


Figure 37. a) XRD analysis of compound **2.5** b) CV analysis of **2.5**

Overall, the results here will allow the prediction of the properties of various ferrocene-containing macrocycles, allowing targeted synthesis by the alteration of the groups directly attached to the ferrocene moiety.

## 7. Further Work

Although both of the disubstituted ferrocenes explored here were unstable under the *N*-acylation conditions tested, it is possible that further alteration of the conditions to prevent acid anhydride formation could enable some formation of the intended *N*-acylated products. Ferrocene reactivity is very similar to that of benzene, and it is known that basic conditions, such as the ones used in *N*-acylation reactions tested in this project, can promote the hydrolysis of benzoyl chlorides.<sup>134</sup> It is therefore possible that the use of basic conditions such as DMAP, pyridine and NEt<sub>3</sub> may have also caused this for the ferrocene-based acyl chlorides discussed in this review. It may therefore be an advantage to explore less non-basic acylating conditions; however it should be noted that acylation of an amide, such as the lactams used here, is significantly more challenging than the acylation of an amine, so basic conditions may be unavoidable for this step.

The results described suggest that  $\alpha$ -ferrocene acyl chlorides such as **2.9**, **2.5** and **2.26**, are challenging substrates, that seemingly undergo hydrolysis and decomposition more readily than acid chlorides used in more typical published SuRE methods. Therefore, synthesis of a ferrocene starting material with the acyl chloride separated from the Cp ring with a hydrocarbon linker may allow *N*-acylation to occur more easily, with possible alternative SuRE starting materials suggested in Figure 38.

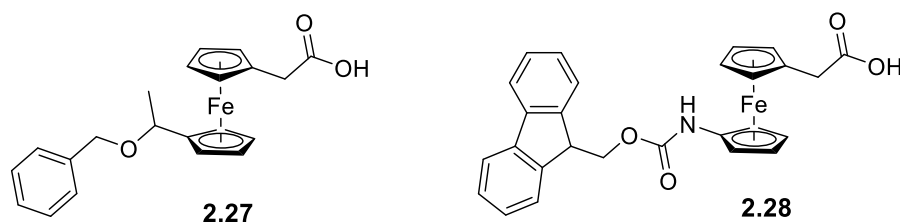


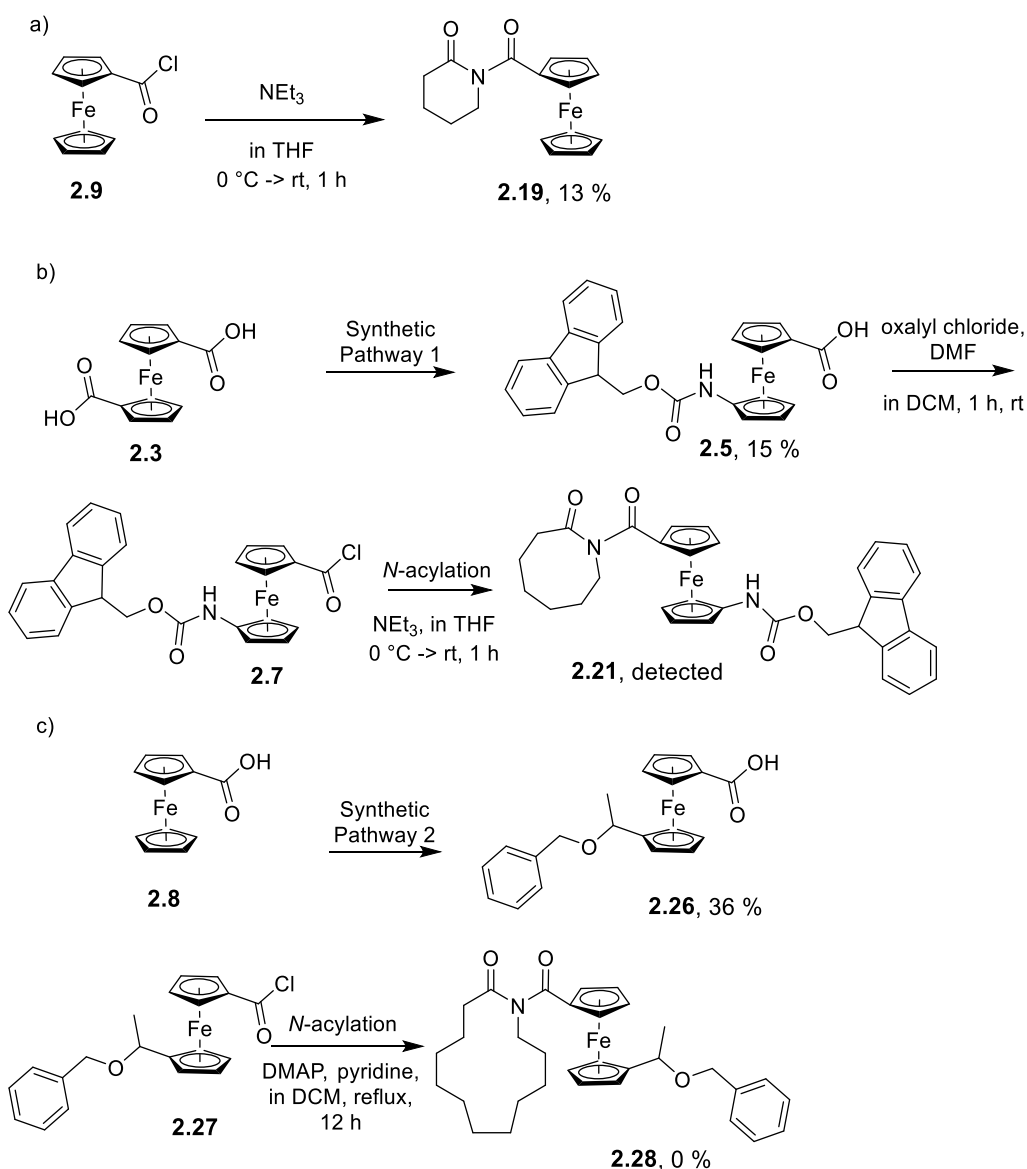
Figure 38. Possible SuRE starting materials **2.27** and **2.28** that incorporate a spacer between the Cp ring and the carboxylic acid functional group.

There is also scope for exploring other organometallic components for implementation into SuRE which may have similar advantages to ferrocene and may be more robust under the conditions used.

## 8. Conclusion and Summaries

SuRE is a new and more efficiency method for synthesising a range of macrocycles with different properties and possible applications. Due to its stability and reactivity along with its optical, mechanical and redox properties, ferrocene is an ideal candidate for investigation of the implementation of organometallics into the SuRE methodology to widen the library of macrocycles created by SuRE even further and make the synthesis of ferrocene-containing macrocycles more accessible. Ferrocene is likely to alter the properties of macrocycles, possibly resulting in macrocycles which can be applied to areas such as medicinal chemistry, molecular electronics and host-guest catalysis.

Two ferrocene-based starting materials **2.5** and **2.26** were synthesised in 15 % and 31 % yields respectively. **2.26** was the highest yielding and most cost-efficient, however the synthesis of **2.5** was less time consuming. Both were tested for use in SuRE along with monosubstituted **2.8** (scheme 52), and although after modifications, a ferrocene-*N*-acylated lactam could be formed using **2.8**, both **2.5** and **2.26** were too unstable under *N*-acylation conditions resulting in decomposition and acid anhydride formation. This is likely due to the proximity of electron withdrawing groups to ferrocene's Cp rings. For *N*-acylation reactions with both **2.8** and **2.5** the major product was an acid anhydride by-product, likely formed as a result of the reaction of hydrolysis products. Future work should look into making alternative starting materials that are more stable with respect to *N*-acylation conditions, therefore allowing progression into the ring expansion step of SuRE.



**Scheme 52.** Summary of the key molecules synthesised and their attempted use in SuRE. a) Formation of **2.19** from **2.9** using  $\text{NEt}_3$ , stirring for 1 hour at  $0^\circ\text{C}$  upon addition, then warming to room temperature. b) formation of **2.21** from **2.5** first by the formation of acid chloride **2.7** stirring with oxalyl chloride and DMF at room temperature for 1 h; then reacting with  $\text{NEt}_3$ , stirring for 1 hour at  $0^\circ\text{C}$  upon addition, then warming to room temperature; c) attempted formation of **2.28** from **2.26**.

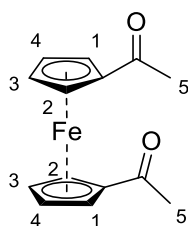
Throughout this process a number of ferrocene-containing precursors were synthesised. These were analysed for their electrochemical and optical properties by CV, DFT calculations and UV-Visible. A trend in HOMO energies, electron withdrawing ability of functional groups and  $E_{1/2}$  values was observed, where compounds in which functional groups with more electron withdrawing ability were more stabilised to oxidation, therefore exhibiting larger  $E_{1/2}$  values and lower energy, more stabilised HOMO orbitals. This trend will allow us to predict the effects that different ferrocene substituents may have on macrocycles allowing more

informed decisions to be made when choosing which ferrocene starting material to be used in SuRE.

## 9. Experimental

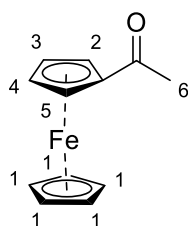
Except where stated, all reagents were purchased from commercial sources and used without further purification. Anhydrous DCM, toluene, Et<sub>2</sub>O and DMF were obtained from an Innovative Technology Inc. PureSolv<sup>®</sup> solvent purification system. MeOH and EtOH, advertised as dry solvents were purchased from various commercial vendors and used as supplied without any additional drying or purification. Water used in all reactions was deionised (DI). <sup>1</sup>H NMR and <sup>13</sup>C NMR were recorded on a JEOL ECS400 spectrometer (operating at 400 MHz and 101 MHz). All spectral data was acquired at 295 K. Chemical shifts ( $\delta$ ) are quoted in parts per million (ppm). The residual solvent peaks,  $\delta_{\text{H}}$  7.26 and  $\delta_{\text{C}}$  77.16 for CDCl<sub>3</sub> and  $\delta_{\text{H}}$  2.50 and  $\delta_{\text{C}}$  39.52 for DMSO-*D*<sub>6</sub> were used as a reference. Coupling constants (*J*) are reported in Hertz (Hz) to the nearest 0.1 Hz. The multiplicity abbreviations used are s(br) broad singlet, s singlet, d doublet, t triplet, pt pseudo triplet, q quartet, m multiplet. Signal assignment was achieved by analysis of COSY, HMBC and HSQC experiments where required. Infrared (IR) spectra were recorded on a PerkinElmer UATR 2 spectrometer as a thin film dispersed from DCM. Mass spectra (high-resolution) were obtained by the University of York Mass Spectrometry Service, using Electrospray Ionization (ESI) on a Bruker compact<sup>®</sup> time of flight mass spectrometer. Thin layer chromatography was carried out on Merk silica gel 60F<sub>254</sub> pre-coated aluminium foil sheers and were visualised using UV light (254 nm) and where necessary, stained with basic aqueous potassium permanganate. X-ray crystallography was conducted by Adrian Whitwood and Theo Tanner, University of York using an Oxford Diffraction SuperNova equipped with a 4-circle goniometer, microfocus Mo & Cu X-ray sources and CCD detector. UV/Vis spectra were measured on a Jasco V-560 UV/Vis spectrophotometer. CV were recorded under an argon atmosphere, in a 0.1 M [n-Bu<sub>4</sub>][PF<sub>6</sub>] DCM solution with a Gamry reference 600TM potentiostat, with a Pt disk electrode (diameter = 3 mm), and two Pt wire electrodes acting as the counter electrode and pseudo-reference electrode. Potentials are reported relative to Fc/Fc<sup>+</sup> couple, with ferrocene, decamethylferrocene and 1,1'-dicyanoferrocene added as internal references at the end of each experiment. Flash column chromatography was carried out using slurry packed Fluka silica gel (SiO<sub>2</sub>), 35-70  $\mu\text{m}$ , 60  $\text{\AA}$ , under a light positive pressure, eluting with the specified solvent system.

### 1,1'-Diacetylferrocene (2.1)



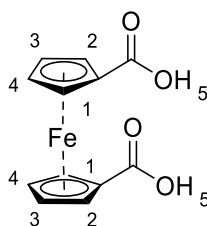
The following procedure was performed based on a literature method.<sup>135</sup> A suspension of anhydrous AlCl<sub>3</sub> (3.99 g, 29.9 mmol) in dry CH<sub>2</sub>Cl<sub>2</sub> (40 mL) was stirred under nitrogen at room temperature. To this, acetyl chloride (4.00 mL, 56.3 mmol) was added slowly through a pressure equalising dropping funnel. The mixture was then cooled to 0 °C and a solution of ferrocene (2.38 g, 12.6 mmol) in dry CH<sub>2</sub>Cl<sub>2</sub> (15 mL) was added dropwise. The resultant solution was stirred at room temperature for 6 hours before pouring the crude reaction mixture into ice water (200 mL) and extracting with CH<sub>2</sub>Cl<sub>2</sub> (2 x 100 mL). The organic extract was combined and washed with 5 wt % aq. NaHCO<sub>3</sub> solution (2 x 50 mL) and dried over Na<sub>2</sub>SO<sub>4</sub>. The crude product was concentrated *in vacuo*. The product was purified by silica-gel column chromatography (petroleum ether/EtOAc; 100:0 → 50:50 → 0:100) and after evaporation to dryness, **2.1** (2.64 g, 9.78 mmol, 76 %) was obtained as a red crystalline solid. <sup>1</sup>H NMR (400 MHz, CDCl<sub>3</sub>) δ (ppm) 4.77 (*pt*, <sup>3</sup>J<sub>HH</sub> = 2.0 Hz, 4 x CpCH: H1,2), 4.51 (*pt*, <sup>3</sup>J<sub>HH</sub> = 2.0 Hz, 4 x CpCH: H3,4), 2.36 (s, 6 x COCH<sub>3</sub>: H5). ESI-MS: *m/z* calcd for [**2.1**+H]<sup>+</sup> [C<sub>14</sub>H<sub>15</sub>FeO<sub>2</sub>]<sup>+</sup>: 271.0416, found: 271.0420; calcd for [**2.1**+Na]<sup>+</sup> [C<sub>14</sub>H<sub>14</sub>FeNaO<sub>2</sub>]<sup>+</sup>: 293.0235, found: 293.0232; calcd for [**2.1**+K]<sup>+</sup> [C<sub>14</sub>H<sub>14</sub>FeKO<sub>2</sub>]<sup>+</sup>: 308.9975, found: 308.9977. The spectroscopic data obtained matched those reported in the literature.<sup>135</sup>

### Acetylferrocene (**2.2**)



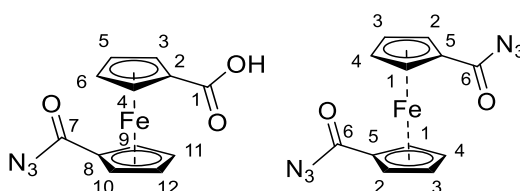
The following procedure was performed based on a literature method.<sup>136</sup> A solution of acetyl chloride (1.85 mL, 23.6 mmol) in DCM (20 mL) was added dropwise to a solution of aluminium chloride (3.50 g, 26.0 mmol) in DCM (20 mL) whilst cooling to 0 °C. This was then added dropwise to a solution of ferrocene (4.00 g, 21.4 mmol) in DCM (20 mL) whilst cooling in an ice bath. The solution was stirred at 0 °C for 30 minutes then allowed to warm to room temperature. After 3 hours of stirring at room temperature, the solution was quenched with ice water (100 mL), extracted with DCM (3 x 100 mL), washed with 5 % wt. NaHCO<sub>3</sub> (100 mL) and dried over MgSO<sub>4</sub>. The volatiles were then removed *in vacuo* and the crude mixture was purified by silica-gel column chromatography (petroleum ether/EtOAc; 50:50) resulting in **2.2** (4.04 g, 17.7 mmol, 82 %) as an orange solid. <sup>1</sup>H NMR (400 MHz, DMSO-*D*<sub>6</sub>) 4.74 (s(br), 2 x CpH: H2,5), 4.47 (s(br), 2 x CpH: H3,4), 4.19 (s, 5 x CpH: H1), 2.38 (s, 1 x CH<sub>3</sub>: H6). The spectroscopic data obtained matched those reported in the literature.<sup>136</sup>

### 1,1'-Ferrocenedicarboxylic acid (**2.3**)



The following procedure was performed based on a literature method.<sup>112</sup> 12 % aq. NaClO (9 mL) was heated to 46 °C under rapid stirring and light-protected conditions. **2.1** (1.00 g, 3.70 mmol), was added in a single portion. After 1.5, 2 and 3 hours 12 % aq. NaClO (3 x 5.5 mL) was added and after each addition, the sides of the round bottomed flask (RBF) were washed with a small amount of DI water. After stirring for a further 16 hours, the mixture was filtered while hot and a saturated aqueous solution of NaHSO<sub>4</sub> was added until the pH became 1, and a light orange precipitate formed. The suspension was then filtered, and the solids collected were washed with DI water and dried *via* Büchner filtration, affording **2.3** (0.640 g, 2.34 mmol, 63 %). <sup>1</sup>H NMR (400 MHz, DMSO-*D*<sub>6</sub>) δ (ppm) 12.30 (s, 1 x COOH: H5), 4.69 (pt, <sup>3</sup>J<sub>HH</sub> = 2.0 Hz, 4 x CpCH: H1,2), 4.46 (pt, <sup>3</sup>J<sub>HH</sub> = 2.0 Hz, 2 x CpCH: H3,4). ESI-MS: m/z calcd for [**2.3**-H]<sup>-</sup> [C<sub>12</sub>H<sub>9</sub>FeO<sub>4</sub>]: 272.9856, found: 272.9853. The spectroscopic data obtained matched those reported in the literature.<sup>112</sup>

### 10-Azidocarbonylferrocene-1-carboxylic acid (**2.4**) and 1,1'-diazidocarbonylferrocene (**2.6**)

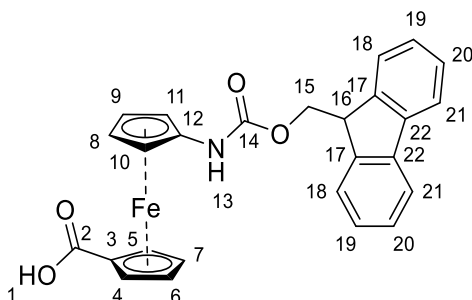


The following procedure was performed based on a literature method.<sup>137</sup> For this experiment **2.3** from a commercial supplier. NEt<sub>3</sub> (0.526 g, 5.20 mmol) was added to a suspension of **2.3** (0.356 g, 1.30 mmol) in dry DCM (1.5 mL). To this, a mixture of DPPA (0.280 mL, 1.30 mmol) in dry DCM (1 mL) was added dropwise. After stirring at room temperature for 10 minutes, 1 M aq. HCl (30 mL) was added and the product mixture was extracted with DCM (4 x 20 mL), filtered and dried over MgSO<sub>4</sub>. The crude mixture was then concentrated *in vacuo* and purified by silica-gel column chromatography (petroleum ether/EtOAc; 50:50 → 0:100), resulting in the formation of **2.6** (yield not measured) as a dark red solid and **2.4** (0.138 g, 0.46 mmol, 36 %) as a red-orange solid. Crystals for XRD analysis were grown from slow diffusion of hexane into DCM.

Data for **2.4**:  $^1\text{H}$  NMR (400 MHz,  $\text{CDCl}_3$ )  $\delta$  (ppm) 4.93 (*pt*,  $^3J_{\text{HH}} = 1.7$  Hz, 2 x CpCH: H11,12), 4.90 (*pt*,  $^3J_{\text{HH}} = 1.7$  Hz, 2 x CpCH: H5,6), 4.58 (*pt*,  $^3J_{\text{HH}} = 1.7$  Hz, 2 x CpCH: H3,4), 4.52 (*pt*,  $^3J_{\text{HH}} = 1.7$  Hz, 2 x CpCH: H9,10);  $^1\text{H}$  NMR (400 MHz,  $\text{DMSO-}D_6$ )  $\delta$  (ppm) 12.45 (s, 1 x  $\text{CH}_3\text{OOH}$ ), 4.80 (*pt*,  $^3J_{\text{HH}} = 1.8$  Hz, 2 x CpCH: H11,12), 4.77 (*pt*,  $^3J_{\text{HH}} = 1.7$  Hz, 2 x CpCH: H5,6), 4.64 (*pt*,  $^3J_{\text{HH}} = 1.8$  Hz, 2 x CpCH: H3,4), 4.55 (*pt*,  $^3J_{\text{HH}} = 1.7$  Hz, 2 x CpCH: H9,10);  $^{13}\text{C}$  NMR (101 MHz,  $\text{DMSO-}D_6$ ) 175.0 (CON<sub>3</sub>: C7), 170.4 (COOH: C1), 74.4 (CpC: C2), 74.1 (2 x CpCH: C9,10), 73.4 (CpC: C8), 72.9 (2 x CpCH: C3,4), 72.0 (2 x CpCH: C11,12), 71.4 (2 x CpCH: C5,6). The spectroscopic obtained matched those reported in the literature.<sup>137</sup>

Data for **2.6**:  $^1\text{H}$  NMR (400 MHz,  $\text{CDCl}_3$ )  $\delta$  (ppm) 4.89 (*pt*,  $^3J_{\text{HH}} = 2.0$  Hz, 4 x CpCH: H1,2), 4.55 (*pt*,  $^3J_{\text{HH}} = 2.0$  Hz, 4 x CpCH: H3,4);  $^1\text{H}$  NMR (400 MHz,  $\text{DMSO-}D_6$ )  $\delta$  (ppm) 4.88 (*pt*,  $^3J_{\text{HH}} = 2.0$  Hz, 4 x CpCH: H1,2), 4.70 (*pt*,  $^3J_{\text{HH}} = 2.0$  Hz, 4 x CpCH: H3,4);  $^{13}\text{C}$  NMR (101 MHz,  $\text{CDCl}_3$ )  $\delta$  (ppm) 175.7 (CO), 74.4 (2 x CpC: C5), 74.25 (4x CH: C1,2), 74.3 (4x CH: C3,4). ESI-MS: *m/z* calcd for [**2.6**+Na]<sup>+</sup> [ $\text{C}_{12}\text{H}_8\text{FeN}_6\text{NaO}_2$ ]<sup>+</sup>: 346.9950, found: 346.9950; IR(FTIR): 2942, 2170, 2139, 1687, 1590, 1488, 1456, 1300, 1267, 1183, 1162  $\text{cm}^{-1}$ . The spectroscopic data obtained matched those reported in the literature.<sup>137</sup>

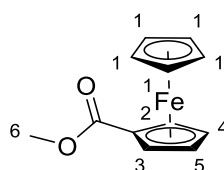
### 10-(((Fluoren-9-yl)methoxycarbonyl)amino]ferrocene-1-carboxylic acid (**2.5**)



The following procedure was performed based on a literature method.<sup>137</sup> For this experiment **2.3** from a commercial supplier. To **2.3** (0.448 g, 1.50 mmol, 0.16 M) in toluene Fmoc-OH (0.739 g, 3.75 mmol) was added and the suspension was heated at reflux for 1 hour resulting in a solution which darkened from red to dark brown. The solution was cooled to room temperature and the toluene was removed *in vacuo*. The crude product was then purified using silica-gel column chromatography (petroleum ether/EtOAc; 60:40 → 50:50 → 0:100) resulting in **2.5** (0.208 g, 0.45 mmol, 30 %) as a gold, crystalline solid. Crystals for XRD analysis were grown from slow diffusion of hexane into DCM.  $^1\text{H}$  NMR (400 MHz,  $\text{DMSO-}D_6$ )  $\delta$  (ppm) 12.04 (s, 1 x OH: H1), 9.02 (s, 1 x NH: H13), 7.92 (d,  $^3J_{\text{HH}} = 7.0$  Hz, 2 x PhH: H18), 7.75 (d,  $^3J_{\text{HH}} = 7.0$  Hz, 2 x PhH: H21), 7.43 (t,  $^3J_{\text{HH}} = 7.0$  Hz, 2 x PhH: H20), 7.36 (t,  $^3J_{\text{HH}} = 7.0$  Hz, 2 x PhH: H19), 4.60 (s(br), 2 x CpH), 4.53 (s(br), 2 x CpH), 4.46-4.42 (m, 1 x CH<sub>2</sub>:

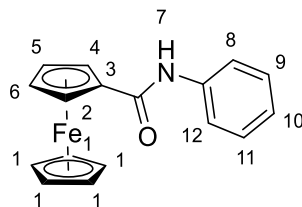
H15), 4.43-4.26 (m, 2 x CpH, 1 x CH: H16), 3.95 (s(br), 2 x CpH:).  $^{13}\text{C}$  NMR (101 MHz,  $\text{CDCl}_3$ )  $\delta$  (ppm) 153.5 (1 x  $\text{C}_{\text{carbamate}}$ : C14), 143.9 (2 x PhC: C17), 140.9 (2 x PhC: C22), 129.0 (1 x  $\text{C}_{\text{carboxylic acid}}$ : C2), 128.2 (2 x PhC: C20), 127.2 (2 x PhC: C19), 125.2 (2 x PhC: C21), 120.2 (2 x PhC: C18), 72.4 (2 x CpC: C4,5 or C6,7 or C8,9 or C11,12), 70.7 (2 x CpC: C4,5 or C6,7 or C8,9 or C11,12), 65.6 (2 x CpC: C4,5 or C6,7 or C8,9 or C11,12), 65.42 (1 x  $\text{CH}_2$ : H15) 60.7 (2x CpC: C4,5 or C6,7 or C8,9 or C11,12), 46.8 (1 x CH: C16). ESI-MS:  $m/z$  calcd for  $[\mathbf{2.5}+\text{Na}]^+$ : 490.0712, found: 490.0707. IR(FTIR): 3065 (br), 1698, 1671, 1553, 1477, 1450, 1393, 1329, 1295, 1235, 1207, 1164, 1082, 1029,  $\text{cm}^{-1}$ . The spectroscopic data obtained matched those reported in the literature.<sup>137</sup>

### (Methoxycarbonyl)ferrocene (**2.10**)



The following procedure performed based on a literature method.<sup>138</sup> For this experiment **2.2** from a commercial supplier was used.  $\text{BF}_3 \cdot \text{Et}_2\text{O}$  (12.3 mL) was added to **2.2** (4.00 g, 17.4 mmol) in dry methanol (120 mL) and heated at reflux. After 16 hours, 5 %  $\text{NaHCO}_3$  (125 mL) was added and the organic material was extracted with DCM (3 x 50 mL) then washed with brine and dried over  $\text{MgSO}_4$  resulting in **2.10** (3.99 g, 16.3 mmol, 94 %) as a dark orange solid.  $^1\text{H}$  NMR (400 MHz,  $\text{CDCl}_3$ ) 4.80 (pt,  $^3J_{\text{HH}} = 2.0$  Hz, 2 x CpH: H2,3), 4.39 (pt,  $^3J_{\text{HH}} = 1.9$  Hz, 2 x CpH: H4,5), 4.20 (s, 5 x CpH: H1), 3.80 (s, 1 x  $\text{CH}_3$ : H6). ESI-MS:  $m/z$  calcd for  $[\mathbf{2.10} + \text{H}]^+[\text{C}_{12}\text{H}_{12}\text{FeO}_2]^+$ : 244.0181, found: 244.0181, calcd for  $[\mathbf{2.10} + \text{Na}]^+[\text{C}_{12}\text{H}_{12}\text{FeNaNO}_2]^+$ : 267.0079, found: 267.0081. The spectroscopic data obtained matched those reported in the literature.<sup>138</sup>

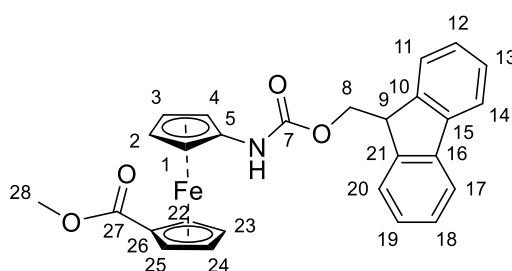
### *N*-Phenylferrocenamide (**2.11**)



The following procedure performed based on a literature method.<sup>139</sup>  $\text{NEt}_3$  (2.0 mL, 14.3 mmol) and aniline (0.919 g, 9.8 mmol) were added to a solution of **2.9** (0.249 g, 1.0 mmol) in dry DCM (20 mL) at 0 °C under a nitrogen atmosphere. After stirring overnight the solution was

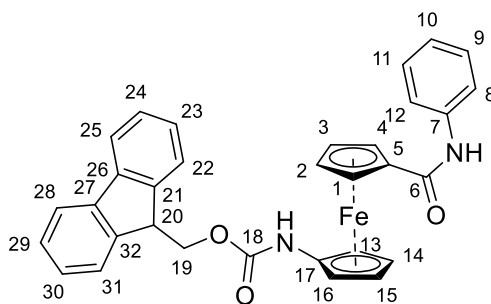
quenched with sat. aq. NaHCO<sub>3</sub> solution (20 mL), the organics were extracted and dried over MgSO<sub>4</sub>. The crude mixture was then purified by slow diffusion recrystallisation of *n*-hexane into DCM, resulting in the formation of **2.11** (0.063 g, 0.21 mmol, 21 %). <sup>1</sup>H NMR (400 MHz, CDCl<sub>3</sub>) 7.60 (d, <sup>3</sup>J<sub>HH</sub> = 8.0 Hz, 2 x PhH: H8,12), 7.40 (s, 1 x NH: H7), 7.39-7.35 (m, 2 x PhH: H9,11), 7.13 (t, <sup>3</sup>J<sub>HH</sub> = 7.0 Hz, 1 x PhH: H10), 4.79 (s(br), 2 x CpH: H2,4 or H5,6), 4.43 (s(br), 2 x CpH: H2,4 or H5,6), 4.27 (s, 5 x CpH: H1). ESI-MS: m/z calcd for [**2.11** + H]<sup>+</sup>[C<sub>17</sub>H<sub>16</sub>FeNO]<sup>+</sup>: 306.0576, found: 306.0577, calcd for [**2.11** + Na]<sup>+</sup>[C<sub>17</sub>H<sub>15</sub>FeNaNO]<sup>+</sup>: 328.0395, found: 328.0395. IR(FTIR): 3280 (br), 2921, 1637, 1596, 1526, 1500, 1458, 1379, 1320, 1265, 1143 cm<sup>-1</sup>. The spectroscopic data obtained matched those reported in the literature.<sup>140</sup>

### 10-(((Fluoren-9-yl)methoxycarbonyl)amino)-methyl-ferrocene-1-carboxylate (**2.12**)



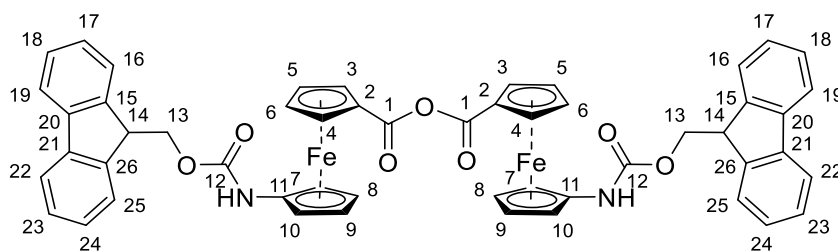
To a solution of **2.7** (0.102 g, 0.21 mmol) in dry DCM (0.5 mL) dry methanol (0.5 mL) was added. After stirring under a nitrogen atmosphere for 3 hours, the volatiles were removed *in vacuo*. The crude mixture was purified by column chromatography silica-gel column chromatography (petroleum ether/EtOAc; 50:50), resulting in **2.13** as a yellow crystalline solid (0.042 mg, 0.09 mmol, 41 %). <sup>1</sup>H NMR (400 MHz, DMSO-*D*<sub>6</sub>) 8.97 (s, 1H, NH), 7.90 (d, <sup>3</sup>J<sub>HH</sub> = 7.0 Hz, 2H, PhH: H11, 20), 7.74 (d, <sup>3</sup>J<sub>HH</sub> = 7.0 Hz, 2H, PhH: 17, 14), 7.41 (t, <sup>3</sup>J<sub>HH</sub> = 7.0 Hz, 2H, PhH: 13, 18), 7.34 (t, <sup>3</sup>J<sub>HH</sub> = 7.0 Hz, 2H, PhH: 12, 19), 4.66 (s(br), 2H, CpH: H1, 4 or 22, 25), 4.55 (s(br), 2H, CpH: H2, 3 or 23, 24), 4.44 (d, <sup>3</sup>J<sub>HH</sub> = 7.0 Hz, 2H, CH<sub>2</sub>: H8), 4.34 (s(br), 2H, CpH: H2, 3 or 23, 24), 4.27 (t, <sup>3</sup>J<sub>HH</sub> = 7.0 Hz, 1H, CH: H9), 3.96 (s(br), 2H, CpH: H1, 4 or 22, 25), 3.61 (s, 3H, CH<sub>3</sub>: H28). <sup>13</sup>C NMR (101 MHz, DMSO-*D*<sub>6</sub>) 170.1 (1 x C<sub>ester</sub>: C27), 153.0 (1 x C<sub>carbamate</sub>: C7), 143.5 (2 x PhC: 10, 21), 140.5 (2 x PhC: 15, 16), 127.4 (2 x PhC: 13, 18), 126.8 (2 x PhC: 12, 19), 124.8 (2 x PhC: 14, 17), 119.9 (2 x PhC: 11, 20), 98.5 (1 x CpC: C5 or 26), 71.7 (1 x CpC: C5 or 26), 71.5 (2 x CpC: C2, 3 or 23, 24), 70.1 (2 x CpC: C1, 4 or 22, 25), 65.0 (1 x CH<sub>2</sub>, C8), 64.8 (2 x CpC: C1, 4 or 22, 25), 60.1 (2 x CpC: C2, 3 or 23, 24), 54.6 (1 x CH<sub>3</sub>: C28), 46.4 (1 x CH: C9). ESI-MS: m/z calcd for [**2.12** + Na]<sup>+</sup>: 504.0869, found: 504.0869. IR(FTIR): 3311 (br), 2951, 1694, 1556, 1465, 1450, 1280, 1141, 740 cm<sup>-1</sup>.

### 10-(((Fluoren-9-yl)methoxycarbonyl)amino)-1-phenylferrocenamamide (**2.13**)



The following procedure was performed based on a literature method.<sup>139</sup> To a solution of **2.7** (0.114 g, 0.24 mmol) in dry DCM (4.7 mL), NEt<sub>3</sub> (0.47 mL, 3.37 mmol) and aniline (0.07 mL, 0.70 mmol) were added whilst cooling to 0 °C. After 1 hour stirring at 0 °C, the volatiles were removed *in vacuo*. The crude mixture was then purified by silica-gel column chromatography (petroleum ether/EtOAc; 50:50) and washing with 1 M HCl (2 x 20 mL) to resulting **2.13** (0.024 g, 0.04 mmol, 17 %) as an orange solid. <sup>1</sup>H NMR (400 MHz, DMSO-*D*<sub>6</sub>) 9.34 (s, 1H, NH<sub>amide</sub>), 9.01 (s, 1H, NH<sub>carbamate</sub>), 7.90 (d, <sup>3</sup>J<sub>HH</sub> = 7.0 Hz, 2H, PhH: 22, 31), 7.75 (d, <sup>3</sup>J<sub>HH</sub> = 8.0 Hz, 2H, 2 x PhH: 8,12), 7.68 (d, <sup>3</sup>J<sub>HH</sub> = 8.0 Hz, 2H, PhH: 25, 28), 7.42 (t, <sup>3</sup>J<sub>HH</sub> = 7.0 Hz, 2H, PhH: 29, 24), 7.34 (t, <sup>3</sup>J<sub>HH</sub> = 7.0 Hz, 2H, PhH: 23, 30), 7.26 (t, <sup>3</sup>J<sub>HH</sub> = 8.0 Hz, 2H, PhH: 9, 11), 7.00 (t, <sup>3</sup>J<sub>HH</sub> = 7.0 Hz, 1H, PhH: H10), 4.95 (s(br), 2H, CpH: H2,3 or 14, 15), 4.57 (s(br), 2H, CpH: H2, 3 or 14, 15), 4.33 (s(br), 2H, CpH: H1, 5 or 13, 16), 4.22-4.14 (m, 3H, CH<sub>2</sub>: C19, CH: 20), 3.97 (s(br), 2H, CpH: H1, 5 or 13, 16). <sup>13</sup>C NMR (101 MHz, DMSO-*D*<sub>6</sub>) 164.6 (1 x C<sub>amide</sub>: C6), 150.4 (1 x C<sub>carbamate</sub>), 140.8 (2 x PhC: C21, 32), 137.8 (2 x PhC: C26, 27), 136.4 (1 x PhC: C7), 125.3 (2 x PhC: C9, 11), 124.6 (2 x PhC: C24, 29), 124.1 (2 x PhC: C23, 30), 122.1 (2 x PhC: C25, 28), 119.9 (1 x PhC: C10), 117.1 (2 x PhC: C22, 31), 117.0 (2 x PhC: 8,12), 95.3 (1 x CpC: C1 or 17), 74.4 (1 x CpC: C1 or 17), 68.3 (2 x CpC: 1,5 or 13, 16), 66.2 (2 x CpC: 2,3 or 14, 15) 62.2 (2 x CpC: 1,5 or 13, 16), 57.5 (2 x CpC: 2,3 or 14, 15), 43.6 (1 x CH<sub>2</sub>: H19), 62.0 (1 x CH: C20). ESI-MS: *m/z* calcd for [**2.13** + Na]<sup>+</sup>: 565.1185, found: 565.1191. IR(FTIR): 3286 (br), 2923, 1705, 1645, 1596, 1538, 1498, 1450, 1393, 1374, 1317, 1262, 1207, 1139, 1083, 1025 cm<sup>-1</sup>.

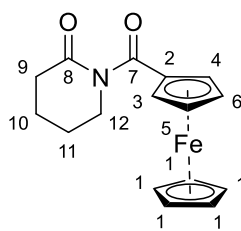
### 1,1''-(Oxydicarbonyl)bis[1'-[[[9H-fluoren-9-ylmethoxy]carbonyl]amino]ferrocene] (**2.18**)



The following procedure performed based on a literature method for the synthesis of **2.21**, with the title product forming as a side-product.<sup>126</sup> 1-Aza-2-cyclooctanone (0.082 g, 0.64 mmol) in

THF (1 mL) was cooled to 0 °C under nitrogen and dry NEt<sub>3</sub> (0.64 mmol, 0.09 mL) was added. Next, a solution of **2.5** (0.21 mmol, 0.104 g) in THF (0.1 mL) was added dropwise. After stirring for 1 hour at 0 °C the solution was quenched with 1 M HCl (10 mL), extracted with DCM (2 x 10 mL) and dried over MgSO<sub>4</sub> and the volatiles were removed *in vacuo*. The crude mixture was then purified by silica-gel column chromatography (petroleum ether/EtOAc; 50:50) resulting in **2.18** (0.026 g, 0.03 mmol, 27 %) as an orange solid. <sup>1</sup>H NMR (400 MHz, DMSO-*D*<sub>6</sub>) 9.09 (s, 2H, 2 x NH), 7.89 (d, <sup>3</sup>J<sub>HH</sub> = 7.0 Hz, 4H, 4 x PhH: H16, 25), 7.70 (d, <sup>3</sup>J<sub>HH</sub> = 8.0 Hz, 4H, 4 x PhH: H19, 22), 7.40 (t, <sup>3</sup>J<sub>HH</sub> = 8.0 Hz, 4H, 4 x PhH: H17, 18, 23 or 24), 7.33 (t, <sup>3</sup>J<sub>HH</sub> = 8.0 Hz, 4H, 4 x PhH: H17, 18, 23 or 24) 4.80 (s(br), 4H, 4 x CpCH: H3, 4, 7 or 10), 4.66 (s(br), 4H, 4 x CpCH: H3, 4, 7 or 10), 4.49 (s(br), 4H, 4 x CpCH: H5, 6, 8 or 9), 4.42 (d, <sup>3</sup>J<sub>HH</sub> = 7.0 Hz, 4H, 2 x CH<sub>2</sub>: H13), 4.24 (t, <sup>3</sup>J<sub>HH</sub> = 7.0 Hz, 2H, 2 x CH: H14), 4.14 (s(br), 4H, 4 x CpCH: H5, 6, 8 or 9). <sup>13</sup>C NMR (101 MHz, DMSO-*D*<sub>6</sub>) 163.9 (2 x C<sub>anhydride</sub>: C1), 150.4 (2 x C<sub>carbamate</sub>: C12), 140.7 (4 x PhC: C15, C26), 137.8 (4 x PhC: C20, C21), 124.6 (4 x PhC: C16, 19, 22 or 25), 124.1 (4 x PhC: C16, 19, 22 or 25), 122.1 (4 x PhC: C16, 19, 22 or 25), 117.1 (4 x PhC: C16, 19, 22 or 25), 71.2 (4 x CpC: C5, 6, 8 or 9), 68.1 (4 x CpC: C3, 4, 7 or 10), 66.2 (2 x CpC: C2 or 11), 62.9 (4 x CpC: C5, 6, 8 or 9), 62.3 (2 x CpC: C2 or 11), 57.9 (4 x CpC: C3, 4, 7 or 10), 51.9 (2 x CH<sub>2</sub>: C13), 43.7 (2 x CH: C14). ESI-MS: *m/z* calcd for [**2.18** +Na]<sup>+</sup>: 939.1426, found: 939.1441. IR(FTIR): 3316 (br), 3066 (br) 1764, 1733, 1702, 1552, 1450, 1244, 1066, 1046, 740 cm<sup>-1</sup>. The spectroscopic data obtained matched those reported in the literature.<sup>123</sup>

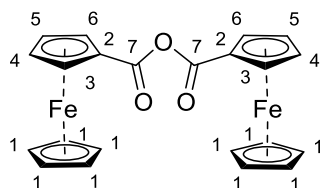
### ***N*-Acylferrocene-2-piperidone (2.19)**



The following procedure performed based on a literature method.<sup>120</sup> NEt<sub>3</sub> (0.460 mL, 3.40 mmol), was added to  $\sigma$ -valerolactam (0.130 g, 1.30 mmol) in dry THF (2 mL). After stirring for 30 minutes **2.9** (0.108 g, 0.44 mmol) in dry THF (0.70 mL) was added dropwise at 0 °C resulting in the solution fuming. After stirring at 0 °C for 1 hour the volatiles were removed *in vacuo* and the crude mixture was purified by silica-gel column chromatography (petroleum ether/EtOAc; 50:50 → 0:100) resulting in **2.19** (0.02 g, 0.06 mmol, 13 %) as an orange crystalline solid. <sup>1</sup>H NMR (400 MHz, CDCl<sub>3</sub>) 4.71 (s(br), 2 x CpH: H3,4 or 5,6) 4.45 (s(br), 2 x CpH: H3,4 or 5,6), 4.17 (s, 5 x CpH: H1), 3.73 (t, <sup>3</sup>J<sub>HH</sub> = 6.0 Hz, 1 x CH<sub>2</sub>: H12), 2.54 (t, <sup>3</sup>J<sub>HH</sub> = 7.0 Hz, 1 x CH<sub>2</sub>: H9), 1.98-1.88 (m, 4H, 2 x CH<sub>2</sub>: H10,11). <sup>13</sup>C NMR (101 MHz, CDCl<sub>3</sub>) 178.4

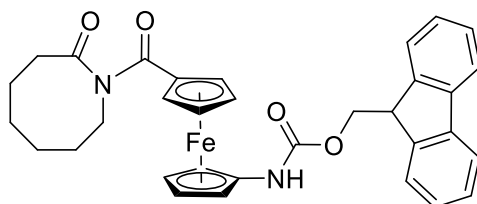
(1 x  $\mathbf{C}_{imide}$ : C7 or C8), 173.3 (1 x  $\mathbf{C}_{imide}$ : C7 or C8), 71.7 (2 x CpC: C5,6), 71.1 (2 x CpC: C3,4), 70.4 (5 x CpC: C1), 46.7 (1 x  $\mathbf{CH}_2$ : C9 or C12), 34.4 (1 x  $\mathbf{CH}_2$ : C9 or C12), 23.2 (1 x  $\mathbf{CH}_2$ : C10 or C11), 21.6 (1 x  $\mathbf{CH}_2$ : C10 or C11). ESI-MS:  $m/z$  calcd for [ $\mathbf{2.19} + \mathbf{H}$ ] $^+$ [ $\mathbf{C}_{16}\mathbf{H}_{18}\mathbf{FeNO}_2$ ] $^+$ : 312.0681, found: 312.0678, calcd for [ $\mathbf{2.19} + \mathbf{Na}$ ] $^+$ [ $\mathbf{C}_{16}\mathbf{H}_{17}\mathbf{FeNNaO}_2$ ] $^+$ : 334.0501, found: 334.0505, calcd for [ $\mathbf{2.19} + \mathbf{Na}$ ] $^+$ [ $\mathbf{C}_{16}\mathbf{H}_{17}\mathbf{FeKNO}_2$ ] $^+$ : 350.0240, found: 350.0254. IR(FTIR): 2951 (br), 1670, 1480, 1449, 1391, 1375, 1285, 1264, 1168 (d), 1105  $\text{cm}^{-1}$ .

### 1,1''-(Oxydicarbonyl)bisferrocene (**2.20**)



The following procedure performed based on a literature method for the synthesis of **2.19**, with the title product forming as a by-product.<sup>126</sup>  $\text{NEt}_3$  (0.46 mL, 3.4 mmol), was added to  $\sigma$ -Valerolactam (0.130 g, 1.3 mmol) in dry THF (2 mL). After stirring for 30 minutes **2.9** (0.108 g, 0.44 mmol) in 0.7 mL dry THF was added dropwise at 0 °C resulting in the solution fuming. After stirring at 0 °C for 1 hour the volatiles were removed in vacuo and the crude mixture was purified by silica-gel column chromatography (petroleum ether/EtOAc; 50:50  $\rightarrow$  0:100) resulting in **2.20** (0.06 g, 0.13 mmol, 60 %). Crystals for XRD analysis were grown from slow diffusion of hexane into DCM.  $^1\text{H}$  NMR (400 MHz,  $\text{CDCl}_3$ ) 4.90 (*pt*,  $^3J_{\text{HH}} = 1.9$  Hz, 4 x CpH: H3,6), 4.56 (*pt*,  $^3J_{\text{HH}} = 2.0$  Hz, 4 x CpH: H4,5), 4.37 (s (br), 10 x CpH: H1).  $^{13}\text{C}$  NMR (101 MHz,  $\text{CDCl}_3$ ) 167.8 (2 x CO: C7), 72.8 (4 x CpC: C4,5), 70.9 (4 x CpC: C3,6), 70.3 (5 x CpC: C1), 69.5 (2 x CpC: C2). ESI-MS:  $m/z$  calcd for [ $\mathbf{2.20} + \mathbf{H}$ ] $^+$ [ $\mathbf{C}_{22}\mathbf{H}_{19}\mathbf{Fe}_2\mathbf{O}_3$ ] $^+$ : 443.0027, found: 443.0018, calcd for [ $\mathbf{2.20} + \mathbf{Na}$ ] $^+$ [ $\mathbf{C}_{22}\mathbf{H}_{18}\mathbf{Fe}_2\mathbf{NaO}_3$ ] $^+$ : 464.9847, found: 464.9847, calcd for: [ $\mathbf{2.20} + \mathbf{K}$ ] $^+$ [ $\mathbf{C}_{22}\mathbf{H}_{18}\mathbf{Fe}_2\mathbf{KO}_3$ ] $^+$ : 480.9586, found: 480.9585. IR(FTIR): 3109 (br), 2922 (br), 1765, 1711, 1444, 1412, 1373, 1243, 1107  $\text{cm}^{-1}$ . The spectroscopic data obtained matched those reported in the literature.<sup>141</sup>

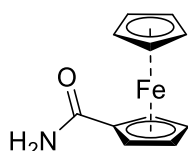
### N-Ferrocene-2-enantholactam (**2.21**)



The following procedure was performed based on a literature method.<sup>126</sup> **2.21** (0.082 g, 0.64 mmol) in THF (1 mL) was cooled to 0 °C under nitrogen and dry  $\text{NEt}_3$  (0.64 mmol, 0.09 mL)

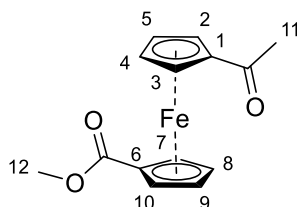
was added. Next, a solution of **2.5** (0.21 mmol, 0.104 g) in THF (0.1 mL) was added dropwise. After stirring for 1 hour at 0 °C an ESI-MS was taken. The solution was quenched with 1 M HCl (10 mL), extracted with DCM (2 x 10 mL), dried over MgSO<sub>4</sub> and the volatiles removed *in vacuo*. The crude mixture was then purified by silica-gel column chromatography (petroleum ether/EtOAc; 50:50), however no **2.21** was isolated. [**2.21** + Na]<sup>+</sup>: 599.1604, found: 599.1603.

### Ferrocenecarboxyl amide (**2.22**)



The following procedure performed based on a literature method for the synthesis of **2.19**, with the title product forming as a by-product.<sup>126</sup> MeMgBr (0.11 mL, 0.32 mmol, 3M solution in diethyl ether) was added to  $\sigma$ -valerolactam (0.03 g, 0.29 mmol) in dry THF (1.1 mL) using a syringe pump over the course of 30 minutes, under a nitrogen atmosphere at 0 °C. This was followed by stirring for another 10 minutes. The solution had frozen by the end of the 10 minutes and was not stirring. To this, a solution of **2.9** (0.11 g, 0.44 mmol) in dry THF (0.5 mL) was added in a single portion. After stirring for another 30 minutes the solution was quenched with sat. aq. NH<sub>4</sub>Cl (10 mL) and extracted with diethyl ether (3 x 20 mL), washed with sat. aq. NaHCO<sub>3</sub> and dried over MgSO<sub>4</sub>. The volatiles were then concentrated *in vacuo* and the crude product was purified by silica-gel column chromatography (petroleum ether/EtOAc; 90:10 → 40:60 → 0:100) and after evaporation to dryness this resulted in the isolation of **2.22** in trace amounts as a crystalline solid. Crystals for XRD analysis were grown from slow evaporation of CDCl<sub>3</sub>. ESI-MS: m/z calcd for [**2.22** + Na]<sup>+</sup>[C<sub>11</sub>H<sub>11</sub>FeNaNO]<sup>+</sup>: 252.0090, found: 252.0088, calcd for [**2.22** + H]<sup>+</sup>[C<sub>11</sub>H<sub>12</sub>FeNO]<sup>+</sup>: 230.0270, found: 230.0260.

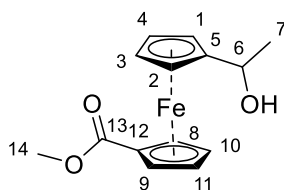
### 1-Acetyl-1'-(methoxycarbonyl)ferrocene (**2.23**)



The following procedure performed based on a literature method.<sup>142</sup> Acetyl chloride (1.30 mL, 18.5 mmol) was added to a suspension of aluminium chloride (2.46 g, 18.5 mmol) in DCM (12 mL) under a nitrogen atmosphere whilst cooling to 0 °C. After stirring for 15 minutes the suspension was added to a solution of **2.10** (1.50 g, 6.15 mmol) in DCM (23 mL) dropwise, over approximately 15 minutes at 0 °C. The flask was then covered with aluminium foil and

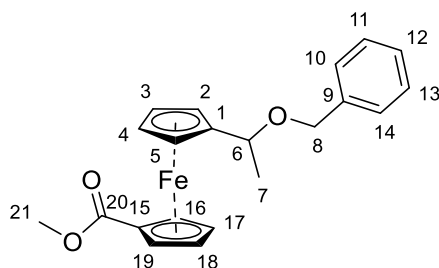
the mixture was stirred at 0 °C for a further 4 hours, forming a purple solution. The reaction was then quenched by addition to ice water (50 mL) and conc. HCl was added until no more precipitate was observed. The organics were then extracted into DCM (3 x 20 mL), dried over MgSO<sub>4</sub> and the volatiles removed *in vacuo* resulting in **2.23** (1.71 g, 5.98 mmol, 97 %) as an orange-brown solid. <sup>1</sup>H NMR (400 MHz, CDCl<sub>3</sub>) 4.80 (pt, <sup>3</sup>J<sub>HH</sub> = 1.8 Hz, 2 x CpH: H8,9), 4.76 (pt, <sup>3</sup>J<sub>HH</sub> = 1.9 Hz, 2 x CpH: H3,2), 4.50 (pt, <sup>3</sup>J<sub>HH</sub> = 1.8 Hz, 2 x CpH: H8,9), 4.40 (pt, <sup>3</sup>J<sub>HH</sub> = 1.9 Hz, 2 x CpH: H3,2), 3.80 (s, 1 x CH<sub>3</sub>,<sub>ketone</sub>: H11), 2.36 (s, 1 x CH<sub>3</sub>,<sub>ester</sub>: H12). The spectroscopic data obtained matched those reported in the literature.<sup>143</sup>

### 1-(1-Hydroxyethyl)-1'-(methoxycarbonyl)ferrocene (2.24)



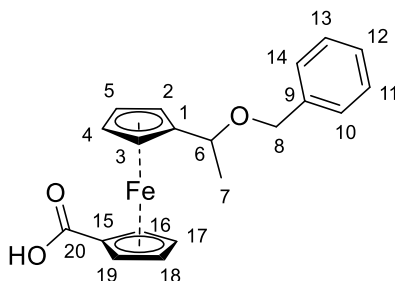
The following procedure performed based on a literature method.<sup>144</sup> To a solution of **2.23** (0.43 g, 1.49 mmol) in dry ethanol (6 mL) and diethyl ether (6 mL) NaBH<sub>4</sub> (0.39 g, 10.4 mmol) was added over approximately 5 minutes. After 4.5 hours of stirring at room temperature under a nitrogen atmosphere, the solution was added to water (20 mL) and extracted with DCM (3 x 20 mL) the organics were then washed with brine (100 mL), dried over MgSO<sub>4</sub>, and the volatiles removed *in vacuo* resulting in **2.24** (0.42 g, 1.45 mmol, 97 %). <sup>1</sup>H NMR (400 MHz, CDCl<sub>3</sub>) 4.84-4.82 (m, 1 x CpH: H1), 4.78-4.77 (m, 1 x CpH: H2), 4.56 (q, <sup>3</sup>J<sub>HH</sub> = 6.0 Hz, 1 x CH: H6), 4.46-4.42 (m, 2 x CpH: H3,4), 4.24 (s(br), 1 x CpH: H10 or H11), 4.21 (s(br), 1 x CpH: H10 or H11), 4.18 (s(br), 2 x CpH: H8,9), 3.83 (s, 3 x CH<sub>3</sub>: H14), 2.63 (s, 1 x OH), 1.38 (d, <sup>3</sup>J<sub>HH</sub> = 6.0 Hz, 3 x CH<sub>3</sub>: H7). <sup>13</sup>C NMR (101 MHz, CDCl<sub>3</sub>) 172.9 (1 x COOMe: C13), 96.8 (1 x CpC: C12), 72.1 (1 x CpC: C5), 71.8 (1 x CpC: C3,4), 71.8 (1 x CpC: C3,4), 70.9 (1 x CpC: C2), 70.3 (1 x CpC: C1), 69.3 (1 x CpC: C 8,9,10,11), 69.2 (1 x CpC: C 8,9,10,11), 67.7 (1 x CpC: 8,9,10,11), 67.6 (1 x CpC: 8,9,10,11), 65.6 (1 x C(H)OH: C6), 52.0 (1 x CH<sub>3</sub>: C14), 24.7 (1 x CH<sub>3</sub>: C7). ESI-MS: m/z calcd for [**2.24** + Na]<sup>+</sup>[C<sub>14</sub>H<sub>16</sub>FeNaO<sub>3</sub>]<sup>+</sup>: 311.0341, found: 311.0340. The spectroscopic data obtained matched those reported in the literature.<sup>144</sup>

### 1-Methoxycarbonyl-1'-[(methylphenyl)isopropyl]ferrocene ether (2.25)



The following procedure was performed based on a literature method.<sup>127</sup> BnBr (1.18 g, 6.92 mmol) and Ag<sub>2</sub>O (1.93 g, 8.31 mmol) were added to a solution of **2.24** (0.40 g, 1.38 mmol) in DCM (15 mL). After stirring for 7 days, the reaction mixture was filtered through celite and washed with brine (20 mL) and extracted with DCM (20 mL) and the organics were dried over MgSO<sub>4</sub>. The crude mixture was then purified by column chromatography (DCM/EtOAc; 100:0 → 10:1) and the volatiles were removed *in vacuo* enabling **2.25** (0.21 g, 0.55 mmol, 40 %) to be isolated as a yellow oil. <sup>1</sup>H NMR (400 MHz, CDCl<sub>3</sub>) 7.34–7.33 (m, 5 x PhH: H10,11,12,13,14), 4.75 (pt, <sup>3</sup>J<sub>HH</sub> = 1.9 Hz, 2 x CpH: 16, 19 or 17,18), 4.49 (d, 2J<sub>HH</sub> = 12.0 Hz, 1 x CH<sub>2</sub>: H8), 4.45 (d, 2J<sub>HH</sub> = 12.0 Hz, 1 x CH<sub>2</sub>: H8), 4.39-4.35 (m, 1 x CH: H6, 2 x CpH: 16, 19 or 17,18 ), 4.28-4.26 (m, 1 x CpH: 2 or 5), 4.22-4.20 (m, 2 x CpH: 3,4, 1 x CpH: 2 or 5), 3.76 (s, 3 x CH<sub>3</sub>: H21), 1.55 (d, <sup>3</sup>J<sub>HH</sub> = 6.0 Hz, 3 x CH<sub>3</sub>: H7). <sup>13</sup>C NMR (101 MHz, CDCl<sub>3</sub>) 172.1 (1 x COOMe: C20), 139.0 (1 x PhC: C9), 128.5 (2 x PhC: C11,13 or C10,14), 127.7 (C12), 127.6 (2 x PhC: C11,13 or C10,14), 122.7 (C15), 91.4 (1 x CpC: C1), 72.2 (1 x CH: C6 or 1 x CpC: 16, 17, 18 or 19), 72.1 (1 x CH: C6 or 1 x CpC: 16, 17, 18 or 19), 71.7 (1 x CpC: 16, 17, 18 or 19), 70.9 (1 x CpC: 16, 17, 18 or 19), 70.3 (1 x CpC: C2, 3, 4, 5), 69.9 (1 x CpC: C2, 3, 4, 5), 69.9 (1 x CH<sub>2</sub>: C8), 69.8 (1 x CpC: C2, 3, 4, 5), 67.6 (1 x CpC: C2, 3, 4, 5), 51.7 (1 x CH<sub>3</sub>: C21), 20.3 (1 x CH<sub>3</sub>: C7). ESI-MS: m/z calcd for [**2.25** + Na]<sup>+</sup>[C<sub>21</sub>H<sub>22</sub>FeNaO<sub>3</sub>]<sup>+</sup>: 401.0811, found: 401.0808. calcd of: [**2.25** + K]<sup>+</sup>[C<sub>21</sub>H<sub>22</sub>FeKO<sub>3</sub>]<sup>+</sup>: 417.0550, found: 417.0543.

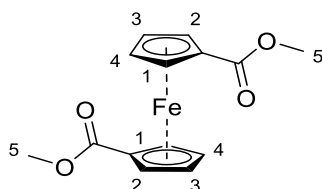
### Carboxy-1'-[(methylphenyl)isopropyl]ferrocene ether (**2.26**)



The following procedure was performed based on a literature method. NaOH (0.01 g, 0.32 mmol) and water (0.04 mL) were added to a solution of **2.25** (0.12 g, 0.31 mmol) in MeOH (1.1 mL). After refluxing overnight the volatiles were removed *in vacuo* and the solid was washed with 5 % aq. NaHCO<sub>3</sub> solution (10 mL). The organics were then extracted with DCM (2 x 10 mL), the organics acidified with 2M HCl until pH 1 and the extracted again with DCM (2 x 10 mL). The organics were washed with brine (20 mL), dried over MgSO<sub>4</sub> and the volatiles removed *in vacuo* resulting in **2.26** (0.10 g, 0.26 mmol, 84 %) as an orange oil. 7.34-7.25 (5 x PhC: C10, 11, 12, 13 or 14), 4.81 (pt, <sup>3</sup>J<sub>HH</sub> = 1.9 Hz, 2 x CpH: 16, 19 or 17,18), 4.50 (s (br), 1 x CH<sub>2</sub>: H8), 4.44-4.38 (m, 1 x CH: H6, 2 x CpH: 16, 19 or 17,18), 4.32-4.30 (m, 1 x H 2 or 3), 4.27-4.25 (m, 1 x CpH: H2 or 3, 2 x CpH: H4,5), 1.58 (d, <sup>3</sup>J<sub>HH</sub> = 6.0 Hz, 3 x CH<sub>3</sub>: H7). <sup>13</sup>C NMR

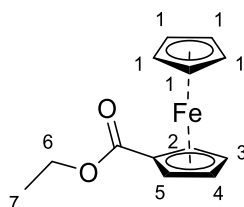
(101 MHz, CDCl<sub>3</sub>) 138.8 (1 x PhC: C9), 128.5 (4 x PhC: 10, 11, 12, 13, 14), 127.8 (1 x CpC: C15), 127.8 (4 x PhC: 10, 11, 12, 13, 14), 127.6 (1 x COOH: C20), 91.8 (1 x CpC: C1), 72.9 (1 x CH: C6 or 2 x CpC: 16, 19 or 17, 18), 72.2 (1 x CH: C6 or 2 x CpC: 16, 19 or 17, 18), 71.4 (1 x CpC: 16, 19, 17 or 18), 71.4 (1 x CpC: 16, 19, 17 or 18), 70.4 (1 x CpC: C2 or 3 or 1 x CpC: C4 or 5), 70.3 (1 x CpC: C2 or 3 or 1 x CpC: C4 or 5), 70.2 (1 x CpC: C2 or 3 or 1 x CpC: C4 or 5). 70.1 (1 x CpC: C8), 68.0 (1 x CpC: C2 or 3), 20.4 (1 x CH<sub>3</sub>: C7). ESI-MS: m/z calcd for [2.26 + Na + H]<sup>+</sup>[C<sub>20</sub>H<sub>20</sub>FeNaO<sub>3</sub>]<sup>+</sup>: 387.0654, found: 387.0644. Calcd for [2.26 + 2Na]<sup>+</sup>[C<sub>20</sub>H<sub>19</sub>FeNa<sub>2</sub>O<sub>3</sub>]<sup>2+</sup>: 409.0473, found: 409.0470. IR(FTIR): 2867 (br), 1713, 1668, 1475, 1454, 1368, 1291, 1261, 1238, 1163 cm<sup>-1</sup>.

### 1,1'-Bis(methoxycarbonyl)ferrocene (2.29)



The following procedure was performed based on a literature method.<sup>112</sup> For this experiment **2.3** from a commercial supplier. **2.3** (0.130 g, 0.474 mmol) was suspended in methanol (19 mL) and while stirring, BF<sub>3</sub>.Et<sub>2</sub>O (0.380 mL, 3.08 mmol) was added. The reaction was heated at 70 °C for 16 hours. The solution was filtered and the solids were washed with methanol (50 mL). The volatiles were removed from the filtrate in vacuo to form **2.29** as a red crystalline solid (0.0902 g, 0.299 mmol, 63 %). <sup>1</sup>H NMR (400 MHz, DMSO-*D*<sub>6</sub>) δ (ppm) 4.78 (pt, <sup>3</sup>J<sub>HH</sub> = 2.0 Hz, 4 x CpCH: H1,2 or H3,4), 4.54 (pt, <sup>3</sup>J<sub>HH</sub> = 2.0 Hz, 4 x CpCH: H1,2 or H3,4), 3.73 (s, 6 x COOCH<sub>3</sub>: H5). ESI-MS: m/z calcd for [2.29+H]<sup>+</sup> [C<sub>14</sub>H<sub>15</sub>FeO<sub>4</sub>]<sup>+</sup>: 303.0314, found: 303.0316. calcd for [2.29+Na]<sup>+</sup> [C<sub>14</sub>H<sub>14</sub>FeNaO<sub>4</sub>]<sup>+</sup>: 325.0134, found 325.0130. The spectroscopic data obtained matched those reported in the literature.<sup>112</sup>

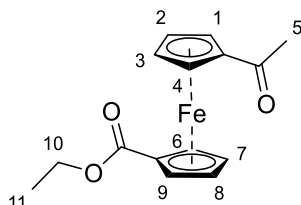
### Ethyl ferrocenecarboxylate (2.30)



The following procedure was performed based on a literature method.<sup>138</sup> For this experiment **2.10** from a commercial supplier. BF<sub>3</sub>.Et<sub>2</sub>O (12.3 mL) was added to **2.10** (4.00 g, 17.4 mmol) in dry ethanol (120 mL) and heated at reflux. After 16 hours, 5 % NaHCO<sub>3</sub> (125 mL) was added and the organic material was extracted with DCM (3 x 50 mL) then washed with brine (50 mL)

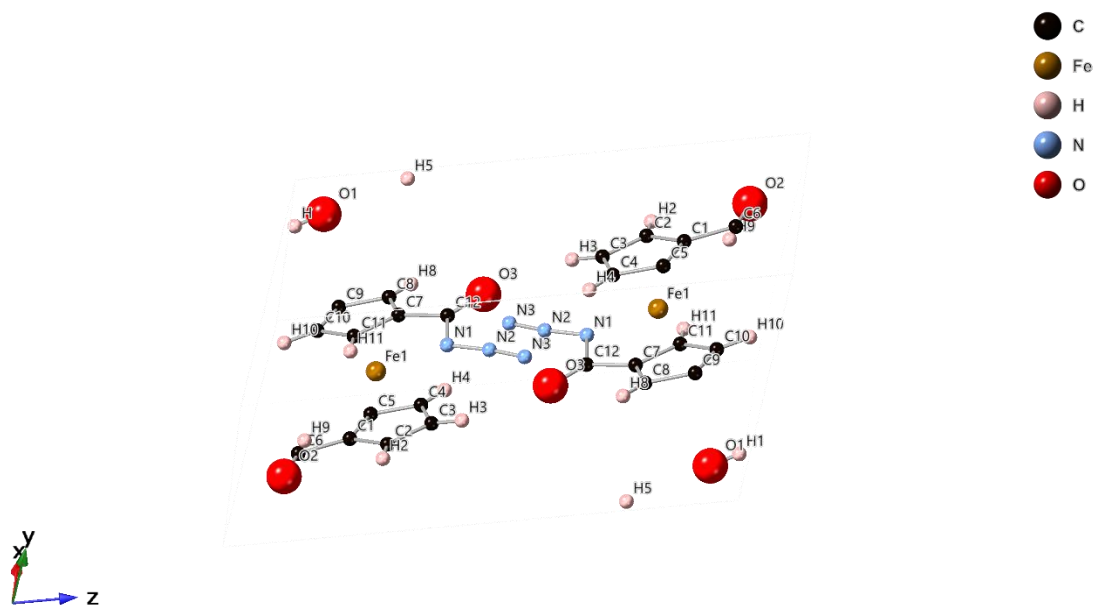
and dried over  $\text{MgSO}_4$  resulting in **2.30** (4.29 g, 16.6 mmol, 96 %) as a brown crystalline solid.  $^1\text{H}$  NMR (400 MHz,  $\text{CDCl}_3$ ) 4.80 (*pt*,  $^3J_{\text{HH}} = 1.9$  Hz, 2 x CpH: H2,5 or H3,4), 4.38 (*pt*,  $^3J_{\text{HH}} = 2.0$  Hz, 2 x CpH: H2,5 or H3,4), 4.28 (q,  $^3J_{\text{HH}} = 6.0$  Hz, 1 x  $\text{CH}_2$ : H6), 4.20 (s, 5 x CpH: H1), 1.35 (t,  $^3J_{\text{HH}} = 7.0$  Hz, 1 x  $\text{CH}_3$ : H7). ESI-MS: *m/z* calcd for [**2.30** + Na] $^+$ [ $\text{C}_{13}\text{H}_{14}\text{FeNaO}_2$ ] $^+$ : 281.0135, found: 281.0233. The spectroscopic data obtained matched those reported in the literature.<sup>145</sup>

### 1-Acetyl-1'-(Ethoxycarbonyl)ferrocene (**2.31**)



The following procedure performed based on a literature method.<sup>142</sup> Acetyl chloride (2.64 mL, 37 mmol) was added to a suspension of aluminium chloride (4.94 g, 37 mmol) in DCM (24 mL) under a nitrogen atmosphere whilst cooling to 0 °C. After stirring for 15 minutes the suspension was added to a solution of **2.30** (3.17 g, 12.3 mmol) in DCM (46 mL) dropwise, over approximately 15 minutes at 0 °C. The flask was then covered with aluminium foil and the mixture was stirred at 0 °C for a further 4 hours, forming a purple solution. The reaction was then quenched by addition to ice water (50 mL) and conc. HCl was added until no more precipitate was observed. The organics were then extracted into DCM (3 x 20 mL), dried over  $\text{MgSO}_4$  and the volatiles removed in vacuo resulting in **2.31** (3.67 g, 12.2 mmol, 99 %).  $^1\text{H}$  NMR (400 MHz,  $\text{CDCl}_3$ ) 4.80 (*pt*,  $^3J_{\text{HH}} = 1.9$  Hz, 2 x CpH: H1,4 or H2,3 or H6,9 or H7,8), 4.75 (*pt*,  $^3J_{\text{HH}} = 1.8$  Hz, 2 x CpH: H1,4 or H2,3 or H6,9 or H7,8), 4.50 (*pt*,  $^3J_{\text{HH}} = 1.8$  Hz, 2 x CpH: H1,4 or H2,3 or H6,9 or H7,8), 4.40 (*pt*,  $^3J_{\text{HH}} = 1.9$  Hz, 2 x CpH: H1,4 or H2,3 or H6,9 or H7,8), 4.28 (q,  $^3J_{\text{HH}} = 7.0$  Hz,  $\text{CH}_2$ : H10), 2.38 (s, H5), 1.35 (t,  $^3J_{\text{HH}} = 7.0$  Hz,  $\text{CH}_3$ : H11).

# Appendices

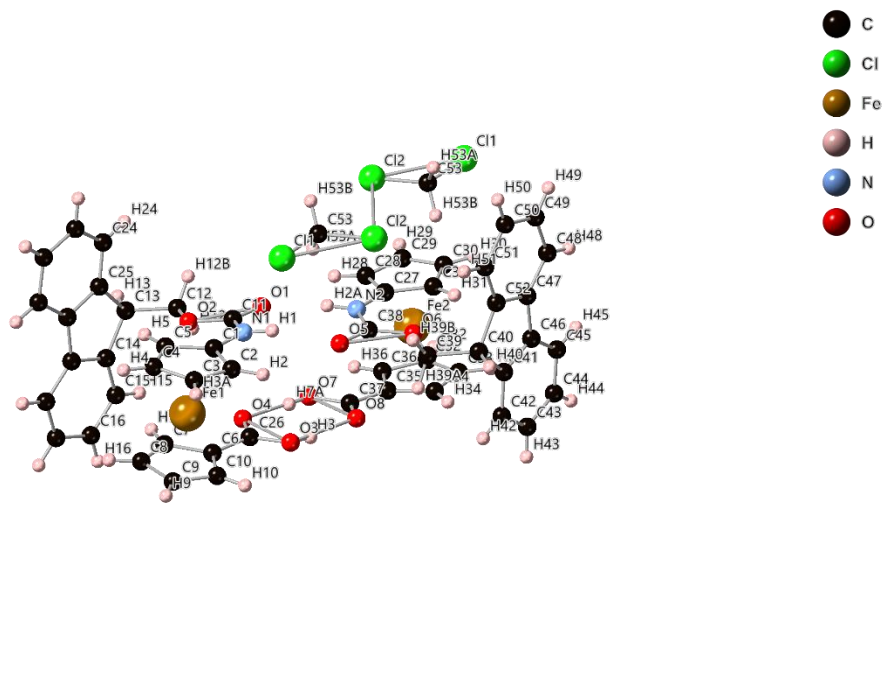


Appendix figure 1. Crystal structure of **2.4** as discovered by XRD analysis

Appendix Table 1. Crystal data for **2.4**.

Identification code	law22014
Empirical formula	$C_{12}H_9FeN_3O_3$
Formula weight	299.07
Temperature/K	110.00(10)
Crystal system	triclinic
Space group	P-1
$a/\text{\AA}$	5.8118(3)
$b/\text{\AA}$	7.2958(4)
$c/\text{\AA}$	14.0882(6)
$\alpha/^\circ$	75.525(4)

$\beta/^\circ$	79.489(4)
$\gamma/^\circ$	78.735(4)
Volume/ $\text{\AA}^3$	561.62(5)
Z	2
$\rho_{\text{calc}}/\text{g}/\text{cm}^3$	1.769
$\mu/\text{mm}^{-1}$	10.867
F(000)	304.0
Crystal size/ $\text{mm}^3$	0.159 × 0.045 × 0.024
Radiation	Cu K $\alpha$ ( $\lambda = 1.54184$ )
2 $\Theta$ range for data collection/ $^\circ$	12.688 to 134.048
Index ranges	$-6 \leq h \leq 6, -8 \leq k \leq 6, -16 \leq l \leq 16$
Reflections collected	4804
Independent reflections	1975 [ $R_{\text{int}} = 0.0363, R_{\text{sigma}} = 0.0424$ ]
Data/restraints/parameters	1975/0/208
Goodness-of-fit on $F^2$	1.094
Final R indexes [ $ I  \geq 2\sigma(I)$ ]	$R_1 = 0.0268, wR_2 = 0.0681$
Final R indexes [all data]	$R_1 = 0.0291, wR_2 = 0.0702$
Largest diff. peak/hole / e $\text{\AA}^{-3}$	0.31/-0.35

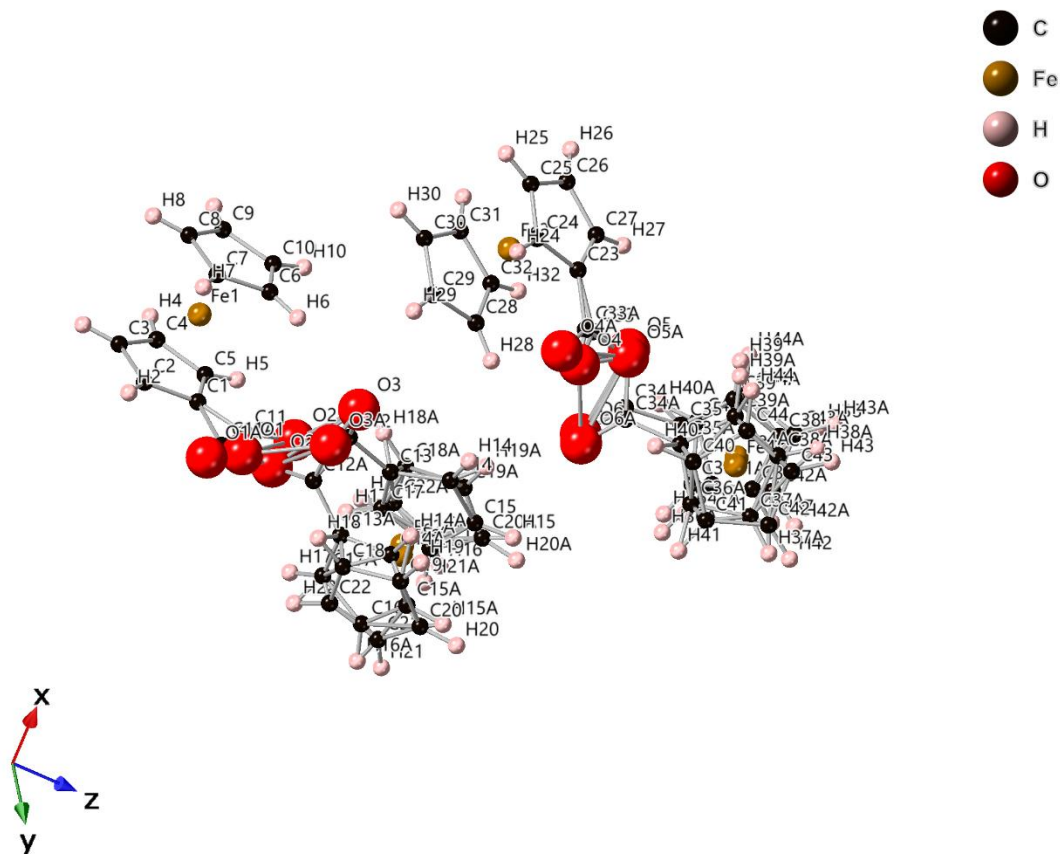


Appendix Figure 2. Crystal structure of **2.5** as discovered by XRD analysis

Appendix Table 2. Crystal data for **2.5**.

Identification code	law22009
Empirical formula	$C_{26.5}H_{22}ClFeNO_4$
Formula weight	509.75
Temperature/K	109.90(14)
Crystal system	monoclinic
Space group	$P2_1/n$
$a/\text{\AA}$	16.3539(4)
$b/\text{\AA}$	16.8286(4)
$c/\text{\AA}$	16.5287(3)
$\alpha/^\circ$	90
$\beta/^\circ$	94.297(2)
$\gamma/^\circ$	90

Volume/Å <sup>3</sup>	4536.13(18)
Z	8
$\rho_{\text{calc}}/\text{cm}^3$	1.493
$\mu/\text{mm}^{-1}$	6.706
F(000)	2104.0
Crystal size/mm <sup>3</sup>	0.12 × 0.1 × 0.1
Radiation	Cu K $\alpha$ ( $\lambda = 1.54184$ )
2 $\Theta$ range for data collection/° 7.334 to 143.792	
Index ranges	-19 ≤ h ≤ 19, -19 ≤ k ≤ 20, -12 ≤ l ≤ 20
Reflections collected	18067
Independent reflections	8614 [R <sub>int</sub> = 0.0552, R <sub>sigma</sub> = 0.0799]
Data/restraints/parameters	8614/0/605
Goodness-of-fit on F <sup>2</sup>	1.039
Final R indexes [ $I \geq 2\sigma(I)$ ]	R <sub>1</sub> = 0.0825, wR <sub>2</sub> = 0.2226
Final R indexes [all data]	R <sub>1</sub> = 0.1194, wR <sub>2</sub> = 0.2571
Largest diff. peak/hole / e Å <sup>-3</sup>	1.33/-1.40

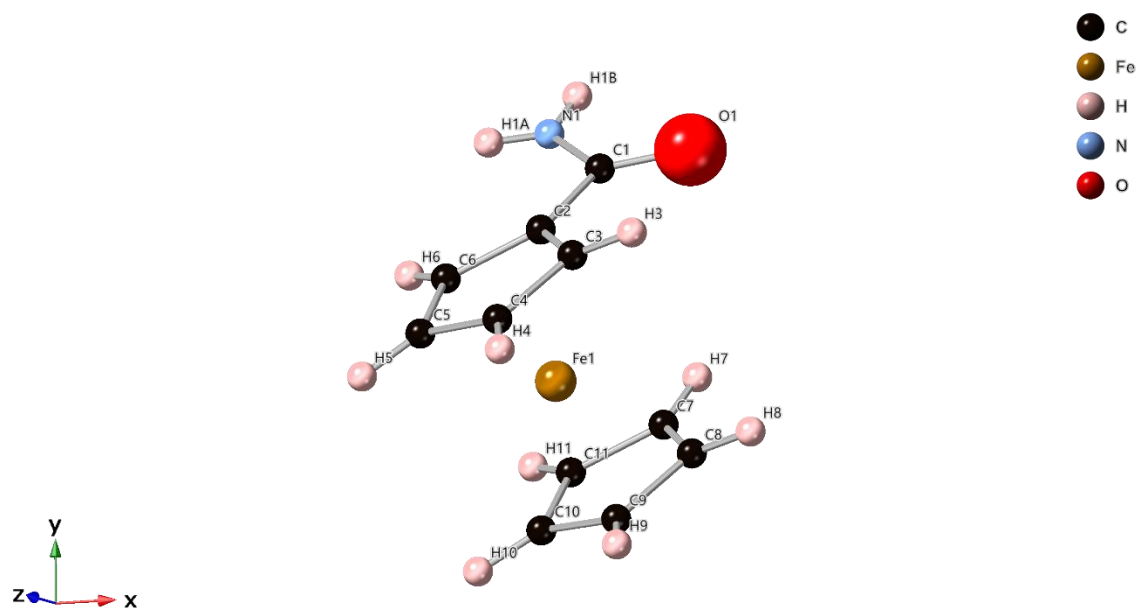


Appendix Figure 3. Crystal structure of **2.20** as discovered by XRD analysis

Appendix Table 3. Crystal data for **2.20**.

Identification code	law22013_twin1_hklf4
Empirical formula	$C_{22}H_{18}Fe_2O_3$
Formula weight	442.06
Temperature/K	110.00(10)
Crystal system	monoclinic
Space group	$P2_1/c$
$a/\text{\AA}$	24.6721(5)
$b/\text{\AA}$	7.84617(14)
$c/\text{\AA}$	19.6893(4)
$\alpha/^\circ$	90

$\beta/^\circ$	112.035(2)
$\gamma/^\circ$	90
Volume/ $\text{\AA}^3$	3533.07(13)
Z	8
$\rho_{\text{calc}}/\text{g/cm}^3$	1.662
$\mu/\text{mm}^{-1}$	13.337
F(000)	1808.0
Crystal size/ $\text{mm}^3$	0.299 × 0.144 × 0.044
Radiation	Cu K $\alpha$ ( $\lambda = 1.54184$ )
2 $\Theta$ range for data collection/ $^\circ$	7.732 to 134.432
Index ranges	$-29 \leq h \leq 29, -9 \leq k \leq 9, -23 \leq l \leq 23$
Reflections collected	10161
Independent reflections	10161 [ $R_{\text{int}} = ?$ , $R_{\text{sigma}} = 0.0237$ ]
Data/restraints/parameters	10161/36/622
Goodness-of-fit on $F^2$	1.049
Final R indexes [ $ I  \geq 2\sigma(I)$ ]	$R_1 = 0.0755, wR_2 = 0.2172$
Final R indexes [all data]	$R_1 = 0.0895, wR_2 = 0.2289$
Largest diff. peak/hole / $e \text{\AA}^{-3}$	1.20/-0.72

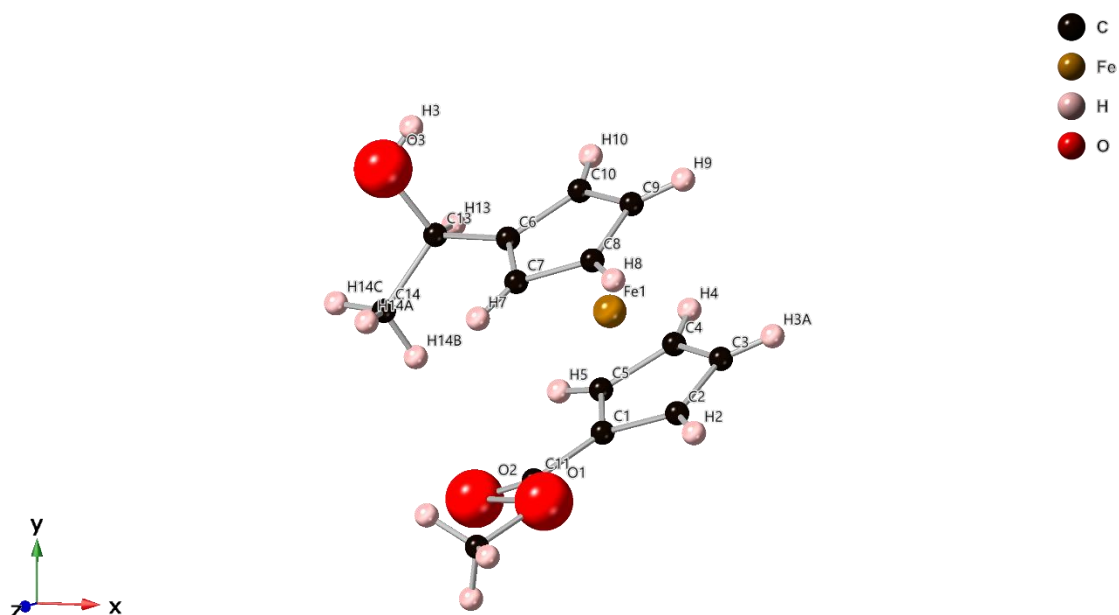


Appendix Figure 4. Crystal structure of **2.22** as discovered by XRD analysis.

Appendix Table 4. Crystal data for **2.22**.

Identification code	law22011
Empirical formula	$C_{11}H_{11}FeNO$
Formula weight	229.06
Temperature/K	109.95(10)
Crystal system	monoclinic
Space group	$P2_1/n$
$a/\text{\AA}$	5.59050(10)
$b/\text{\AA}$	13.1144(2)
$c/\text{\AA}$	12.5739(2)
$\alpha/^\circ$	90
$\beta/^\circ$	95.774(2)
$\gamma/^\circ$	90

Volume/Å <sup>3</sup>	917.19(3)
Z	4
$\rho_{\text{calc}}/\text{g}/\text{cm}^3$	1.659
$\mu/\text{mm}^{-1}$	12.854
F(000)	472.0
Crystal size/mm <sup>3</sup>	0.244 × 0.153 × 0.144
Radiation	Cu K $\alpha$ ( $\lambda = 1.54184$ )
2 $\Theta$ range for data collection/°	9.772 to 134.086
Index ranges	-6 ≤ h ≤ 6, -13 ≤ k ≤ 15, -13 ≤ l ≤ 15
Reflections collected	4680
Independent reflections	1631 [R <sub>int</sub> = 0.0326, R <sub>sigma</sub> = 0.0335]
Data/restraints/parameters	1631/0/172
Goodness-of-fit on F <sup>2</sup>	1.073
Final R indexes [ $ I  \geq 2\sigma(I)$ ]	R <sub>1</sub> = 0.0239, wR <sub>2</sub> = 0.0560
Final R indexes [all data]	R <sub>1</sub> = 0.0257, wR <sub>2</sub> = 0.0568
Largest diff. peak/hole / e Å <sup>-3</sup>	0.33/-0.28

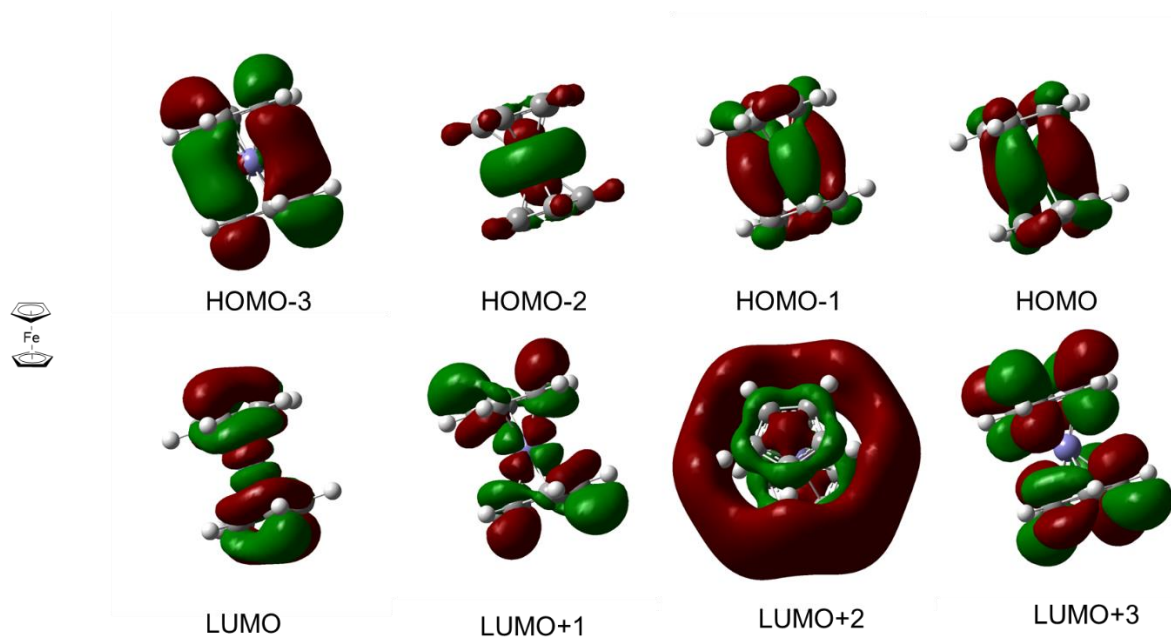


Appendix Figure 5. Crystal structure of **2.24** as discovered by XRD analysis

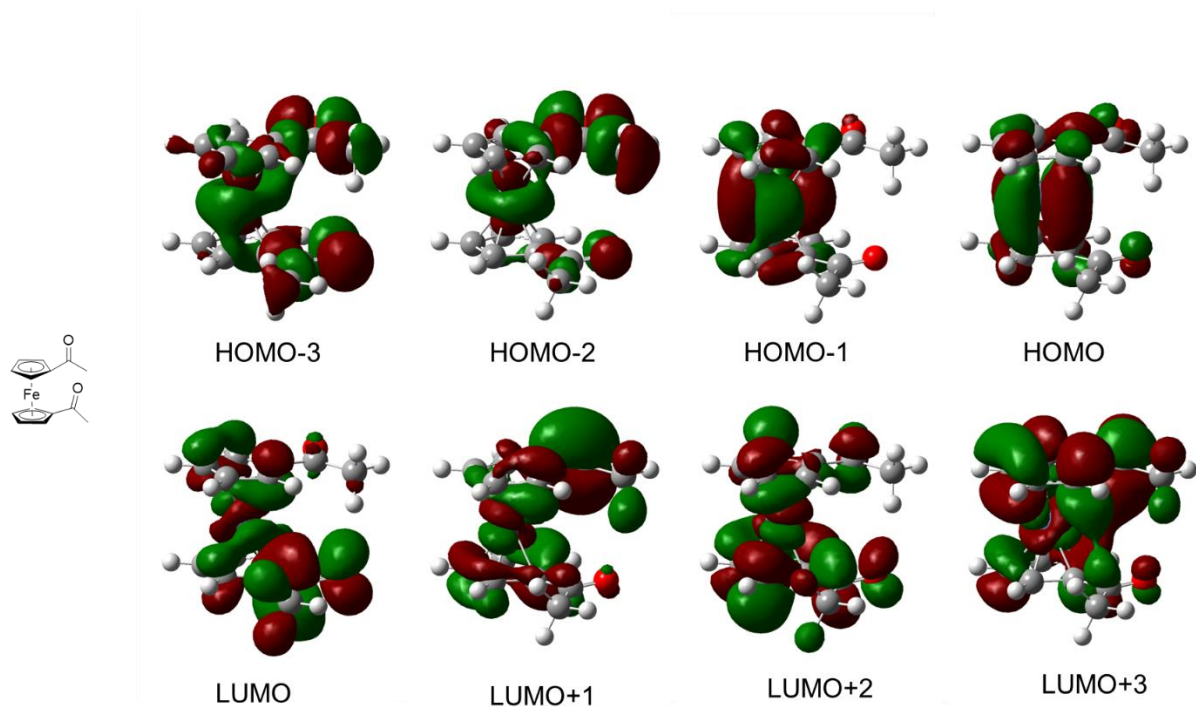
Appendix Table 5. Crystal data for **2.24**.

Identification code	law22010
Empirical formula	$C_{14}H_{16}FeO_3$
Formula weight	288.12
Temperature/K	110.00(10)
Crystal system	monoclinic
Space group	$P2_1/c$
$a/\text{\AA}$	11.30560(10)
$b/\text{\AA}$	7.85870(10)
$c/\text{\AA}$	13.6413(2)
$\alpha/^\circ$	90
$\beta/^\circ$	91.7000(10)
$\gamma/^\circ$	90

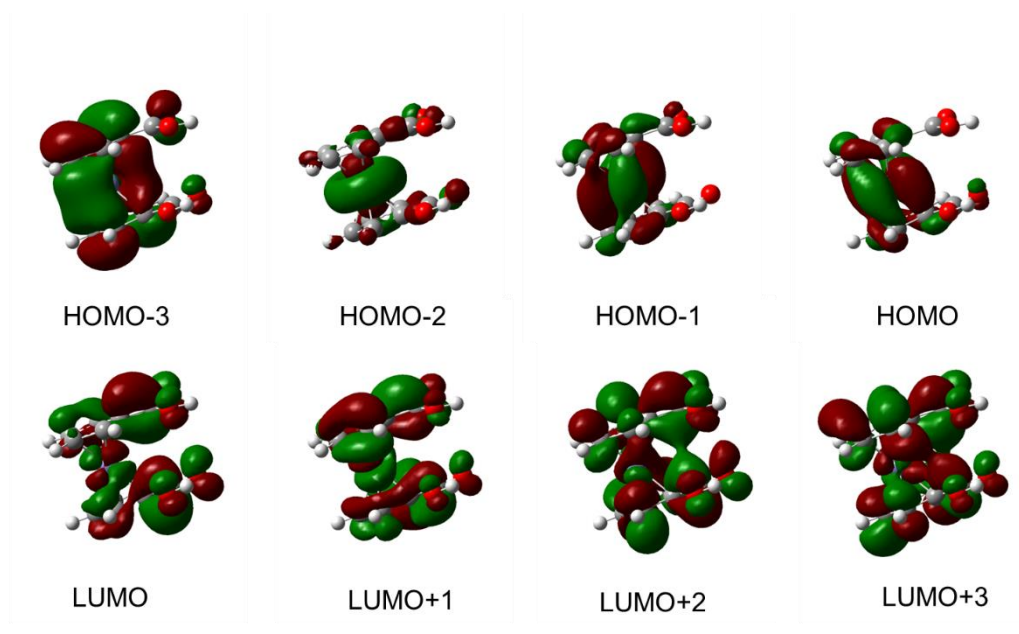
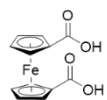
Volume/Å <sup>3</sup>	1211.46(3)
Z	4
ρ <sub>calc</sub> /cm <sup>3</sup>	1.580
μ/mm <sup>-1</sup>	9.965
F(000)	600.0
Crystal size/mm <sup>3</sup>	0.48 × 0.35 × 0.26
Radiation	Cu Kα (λ = 1.54184)
2θ range for data collection/°	7.824 to 153.954
Index ranges	-14 ≤ h ≤ 14, -9 ≤ k ≤ 5, -17 ≤ l ≤ 17
Reflections collected	11203
Independent reflections	2502 [R <sub>int</sub> = 0.0427, R <sub>sigma</sub> = 0.0295]
Data/restraints/parameters	2502/0/155
Goodness-of-fit on F <sup>2</sup>	1.067
Final R indexes [I >= 2σ (I)]	R <sub>1</sub> = 0.0347, wR <sub>2</sub> = 0.0877
Final R indexes [all data]	R <sub>1</sub> = 0.0361, wR <sub>2</sub> = 0.0887
Largest diff. peak/hole / e Å <sup>-3</sup>	0.67/-0.42



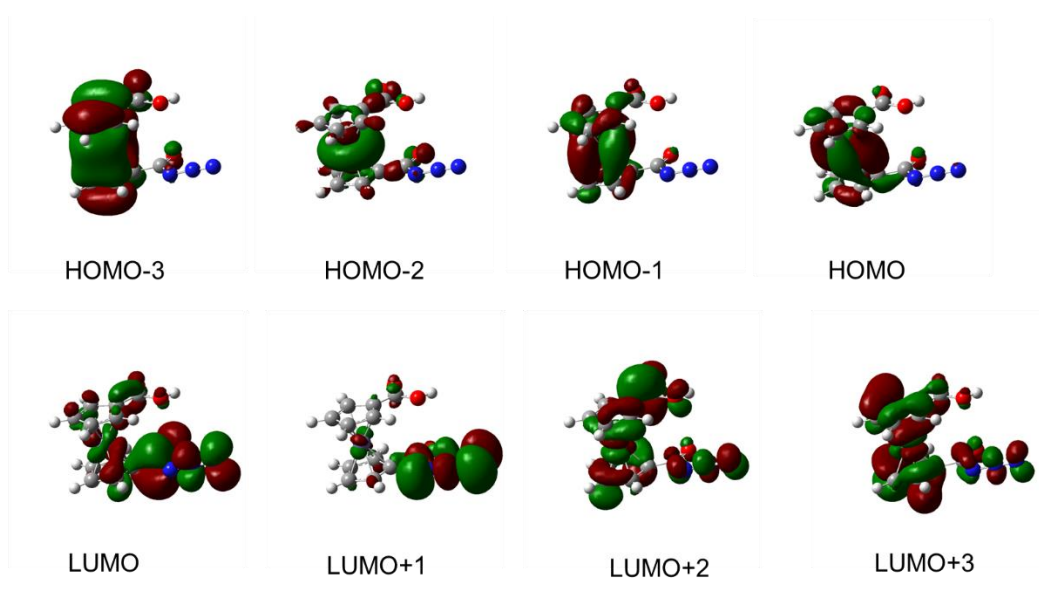
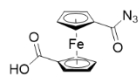
Appendix Figure 6. Molecular orbitals of **Fc** calculated by DFT.



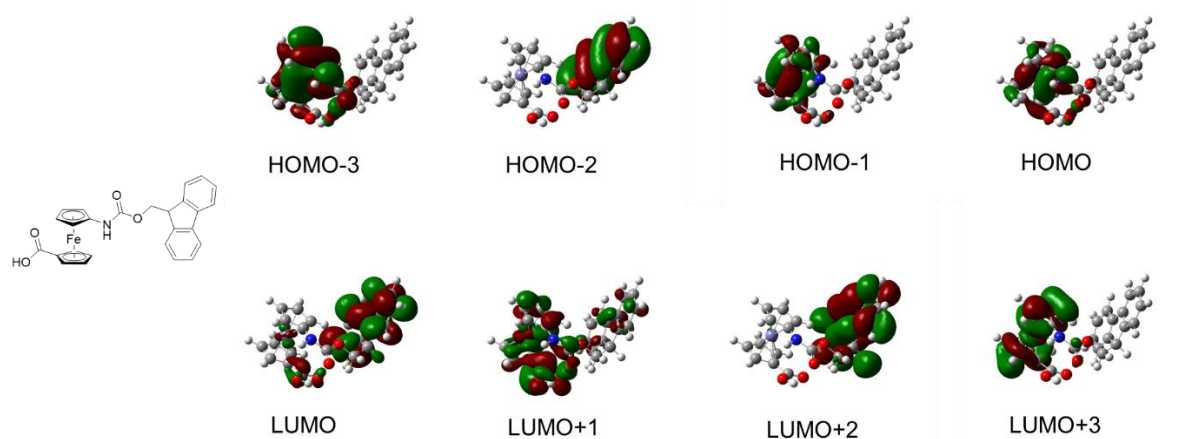
Appendix Figure 7. Molecular orbitals of **2.1** calculated by DFT.



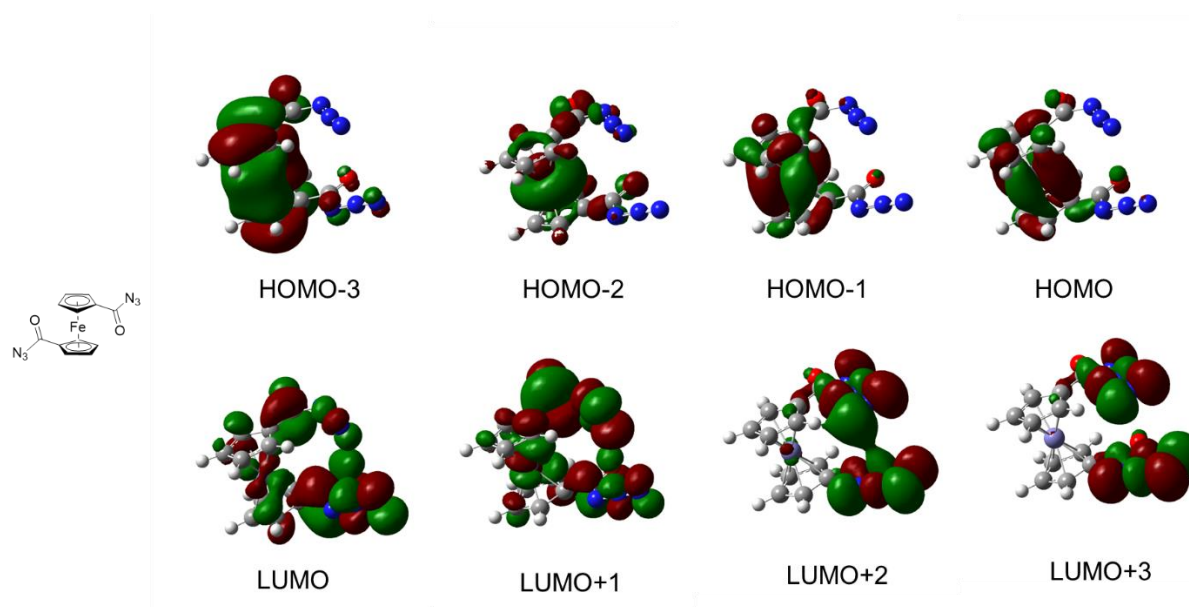
Appendix Figure 8. Molecular orbitals of **2.3** calculated by DFT.



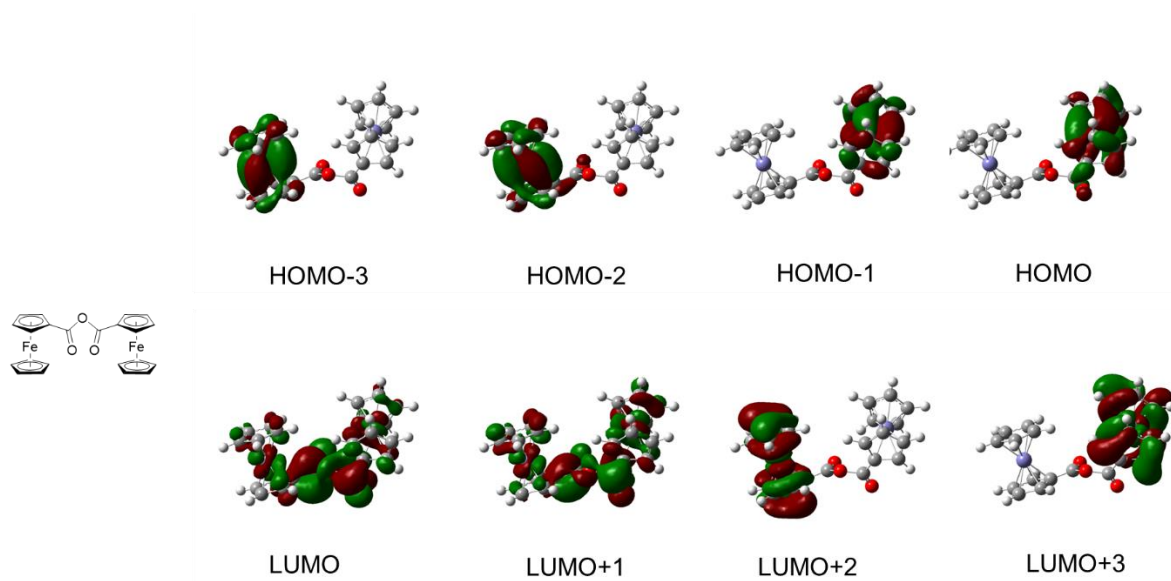
Appendix Figure 9. Molecular orbitals of **2.4** calculated by DFT.



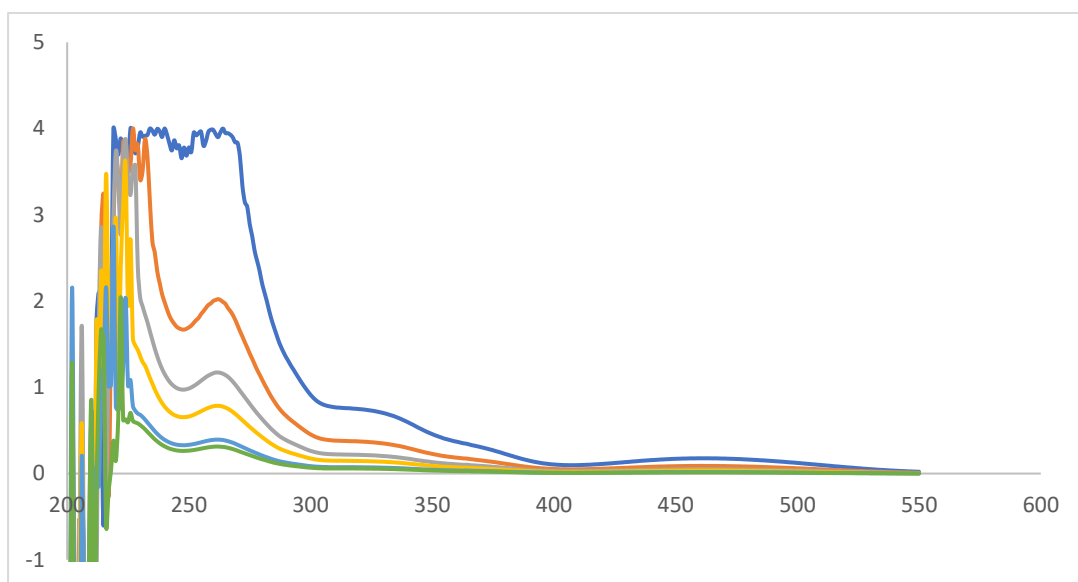
Appendix Figure 10. Molecular orbitals of **2.5** calculated by DFT.



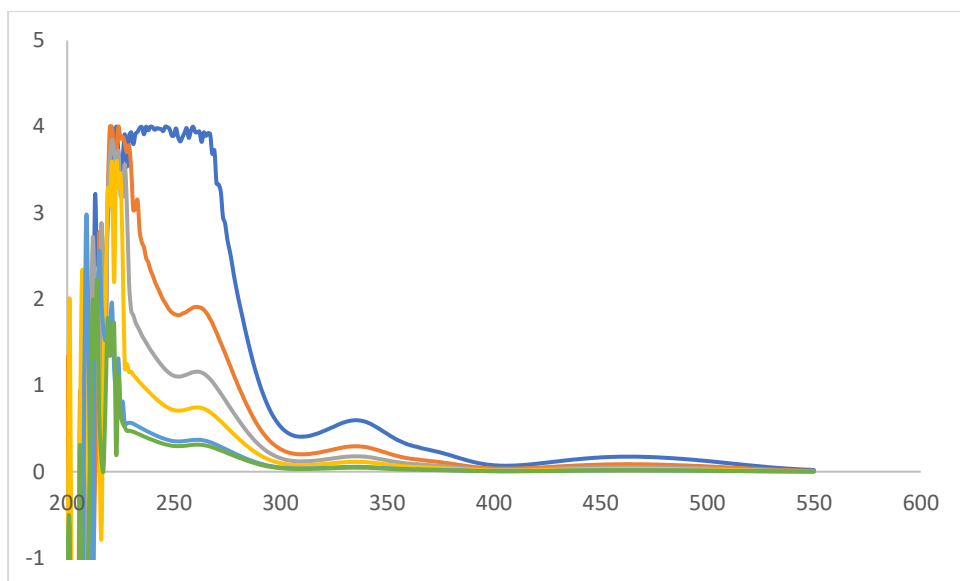
Appendix Figure 11. Molecular orbitals of **2.6** calculated by DFT.



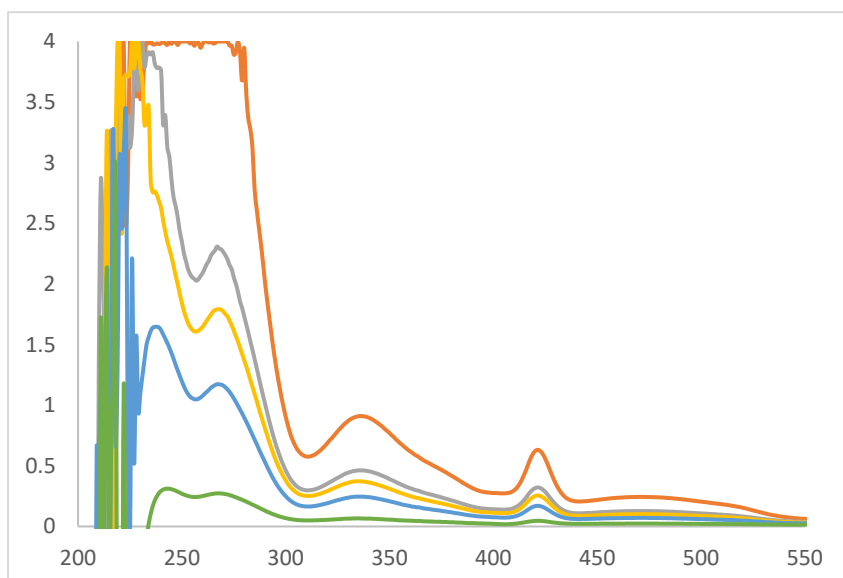
Appendix Figure 12. Molecular orbitals of **2.20** calculated by DFT.



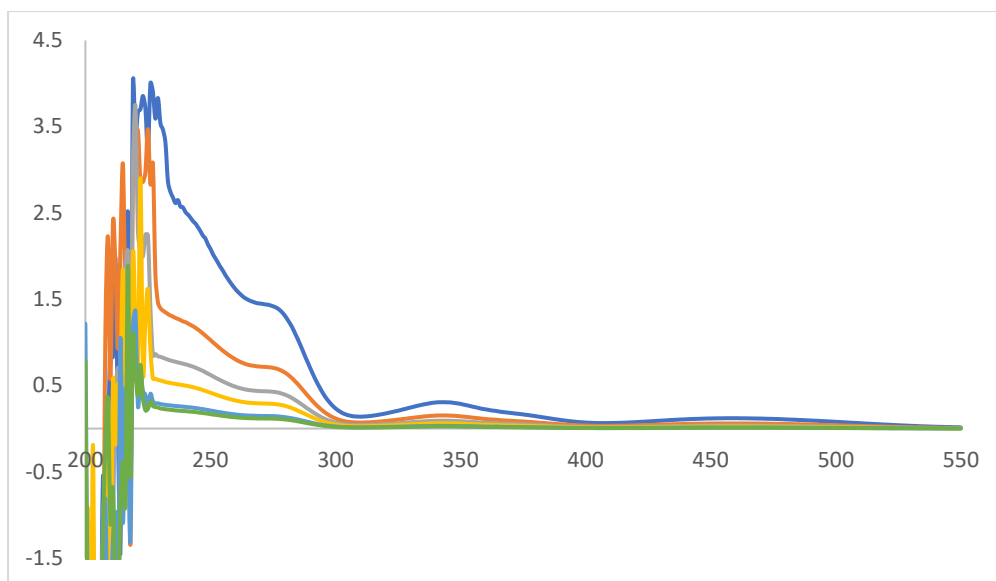
Appendix Figure 13. UV-Visible spectrum of **2.1** at concentrations  $4.1 \times 10^{-4}$ ,  $2.0 \times 10^{-4}$ ,  $1.2 \times 10^{-5}$ ,  $8.1 \times 10^{-6}$ ,  $4.1 \times 10^{-7}$  and  $3.3 \times 10^{-8}$  M.



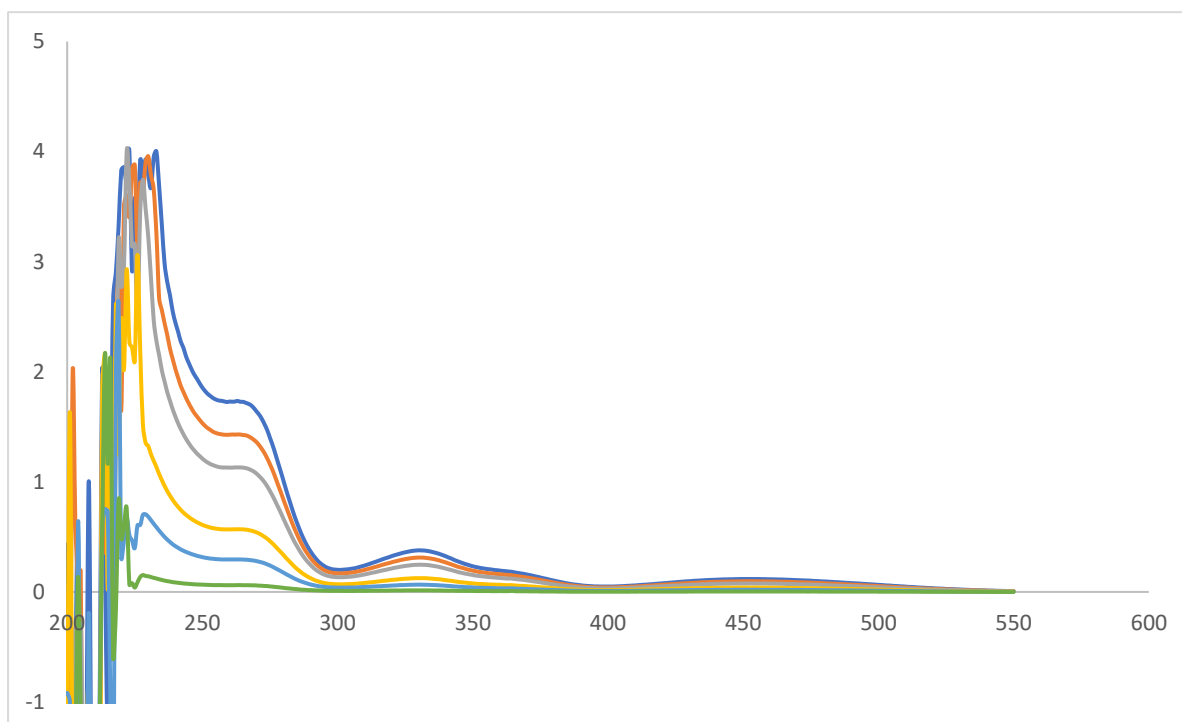
Appendix Figure 2. UV-Visible spectrum of **2.4** at concentrations  $3.3 \times 10^{-4}$ ,  $1.7 \times 10^{-4}$ ,  $1.0 \times 10^{-4}$ ,  $6.7 \times 10^{-5}$ ,  $3.3 \times 10^{-5}$ ,  $3.3 \times 10^{-5}$ ,  $2.7 \times 10^{-5}$  M.



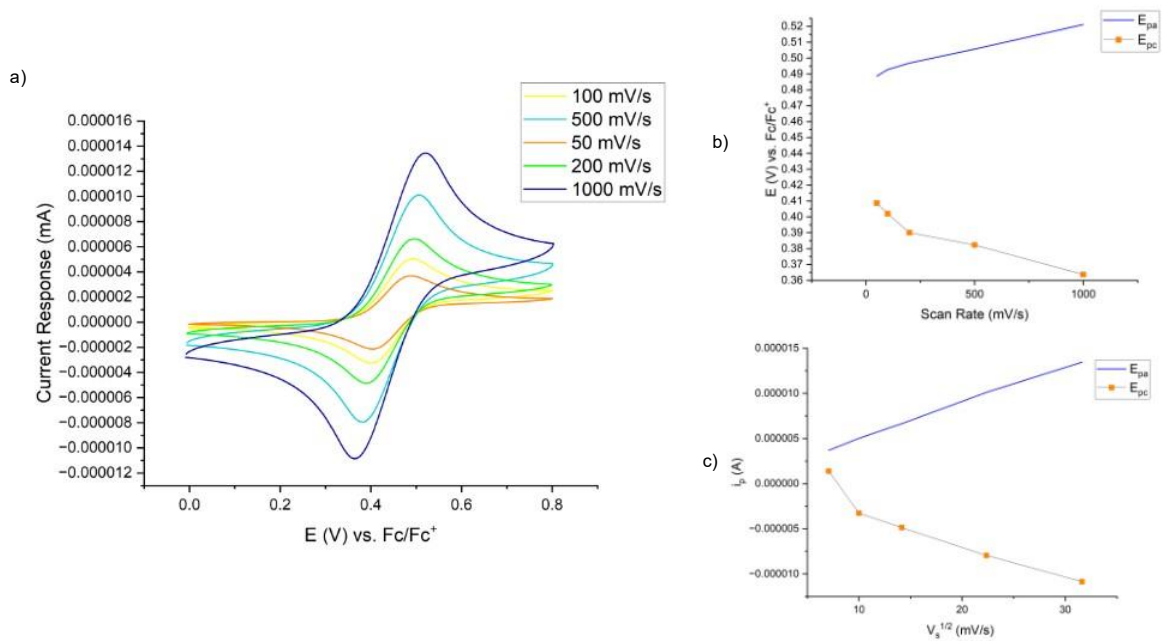
Appendix Figure 15. UV-Visible spectrum of **2.6** at concentrations of  $3.0 \times 10^{-4}$ ,  $1.5 \times 10^{-4}$ ,  $1.2 \times 10^{-4}$ ,  $7.4 \times 10^{-5}$ ,  $1.5 \times 10^{-5}$  M.



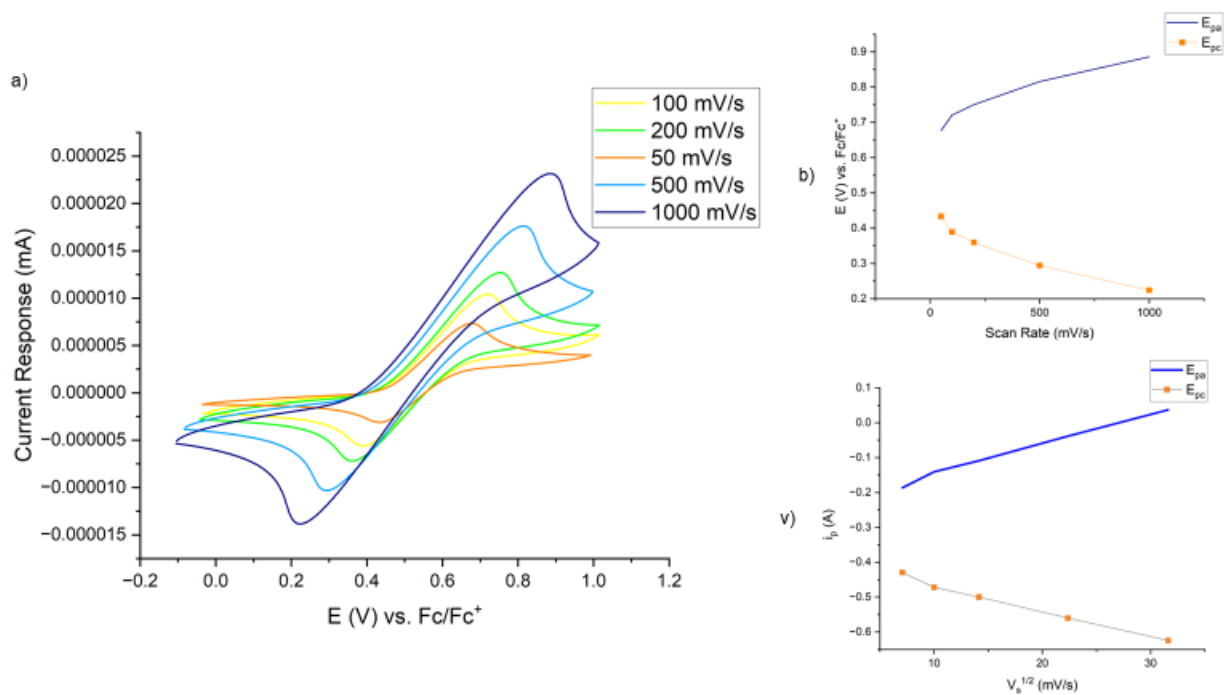
Appendix Figure 16. UV-Visible spectrum of **2.19** at concentrations of  $2.6 \times 10^{-4}$ ,  $1.3 \times 10^{-4}$ ,  $7.7 \times 10^{-5}$ ,  $5.1 \times 10^{-5}$ ,  $2.6 \times 10^{-5}$ ,  $2.1 \times 10^{-5}$  M.



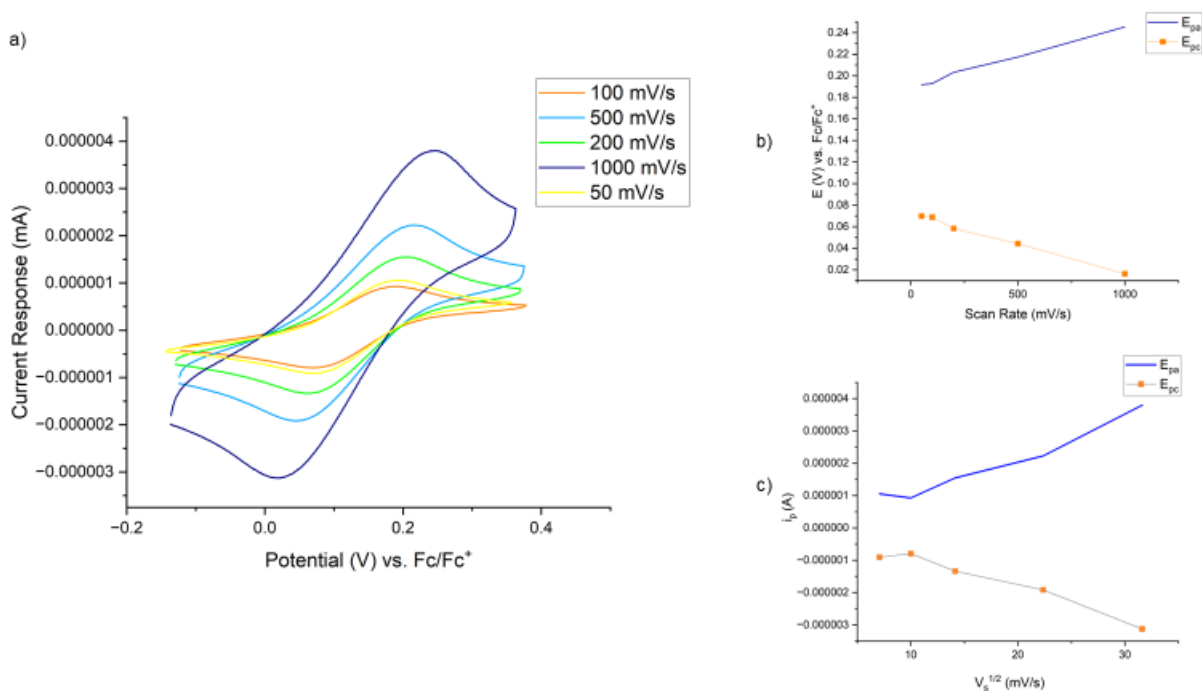
Appendix Figure 17. UV-Visible spectrum of **2.20** at concentrations  $2.8 \times 10^{-4}$ ,  $2.3 \times 10^{-4}$ ,  $1.8 \times 10^{-4}$ ,  $9.1 \times 10^{-5}$ ,  $4.5 \times 10^{-5}$  and  $3.6 \times 10^{-5}$  M.



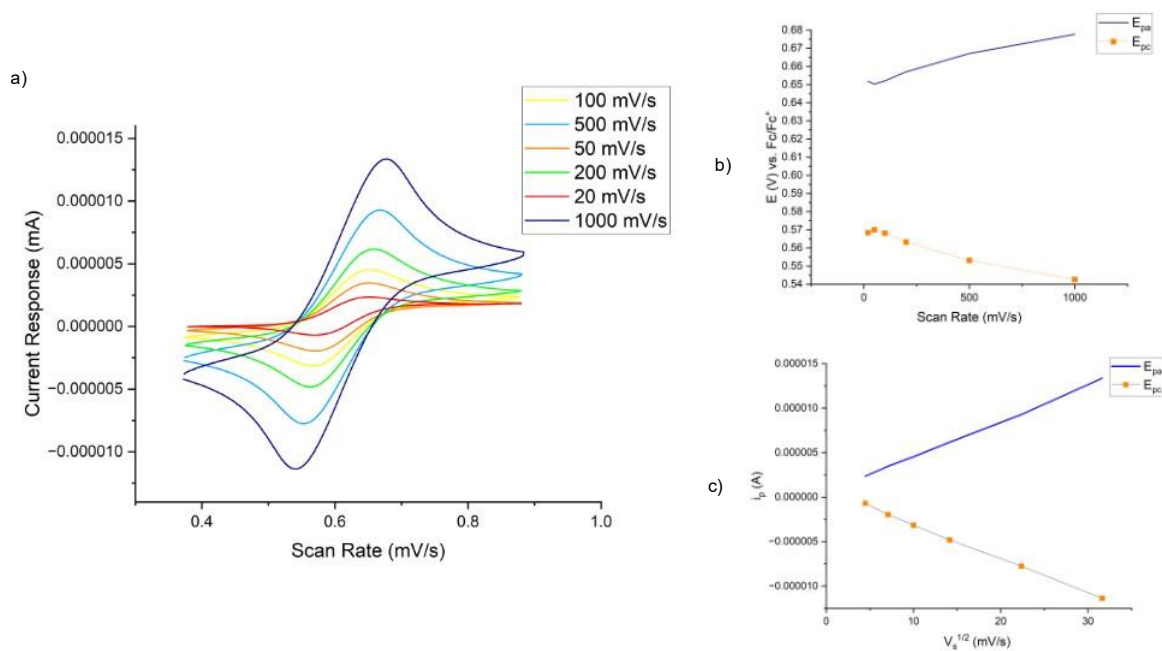
Appendix Figure 18. Electrochemical analysis of **2.1**. a) cyclic voltammogram at different scan rates; b) Scan rate dependence vs. voltage; c) current vs. the square root of scan rate.



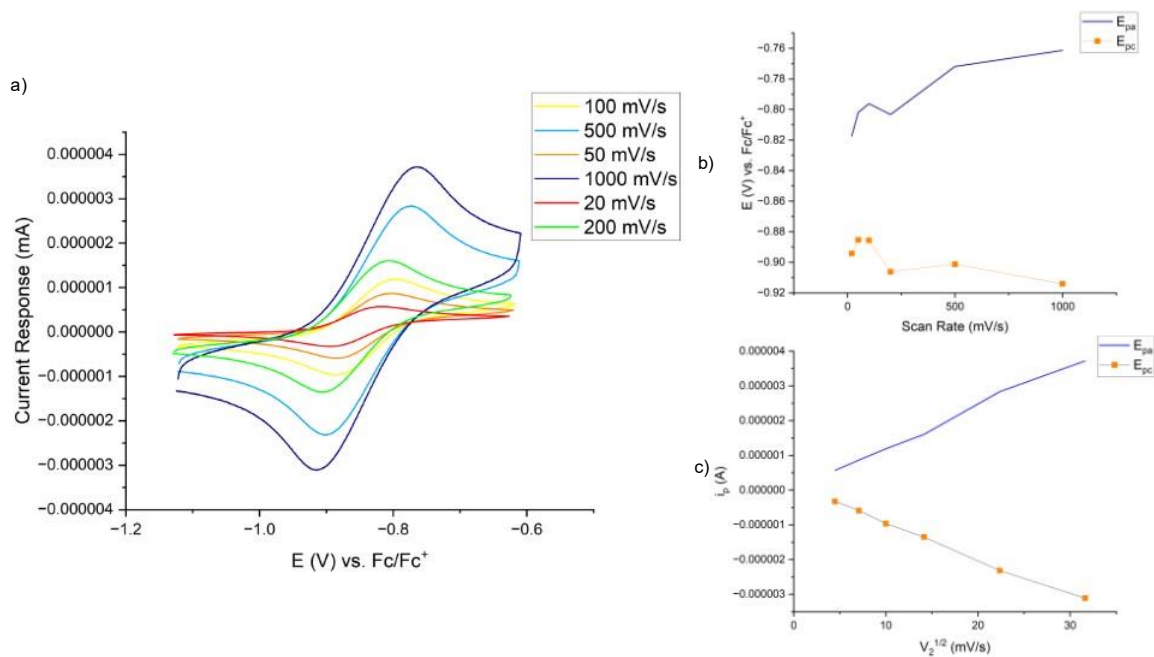
Appendix Figure 19. Electrochemical analysis of **2.4**. a) cyclic voltammogram at different scan rates; b) Scan rate dependence vs. voltage; c) current vs. the square root of scan rate.



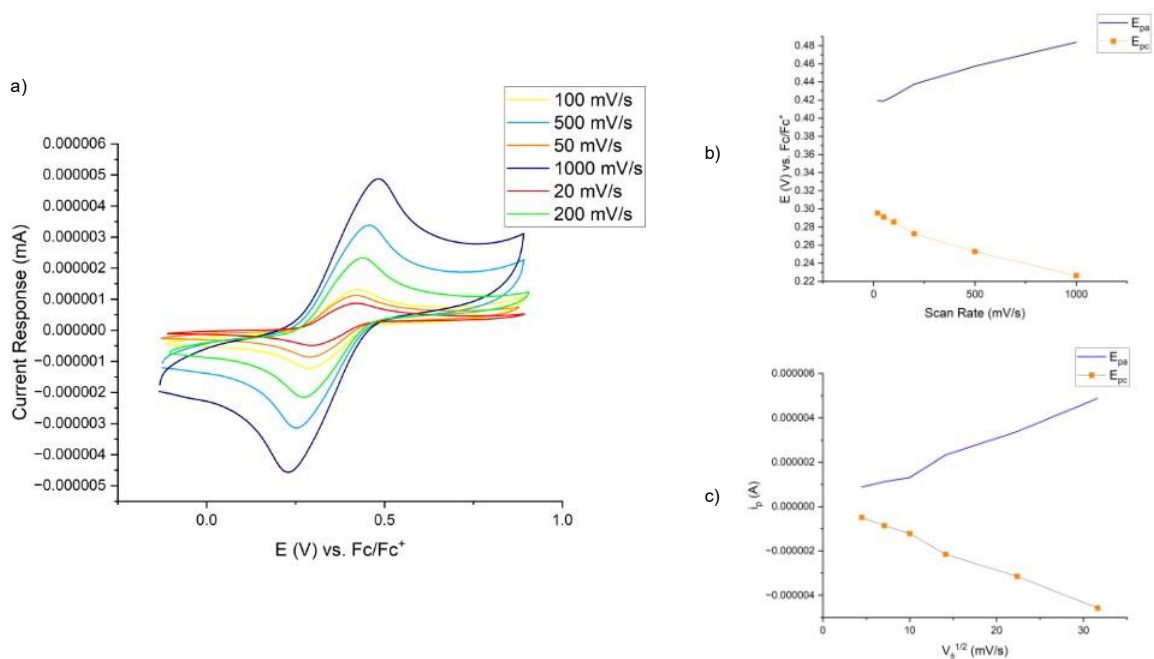
Appendix Figure 20. Electrochemical analysis of **2.5**. a) cyclic voltammogram at different scan rates; b) Scan rate dependence vs. voltage; c) current vs. the square root of scan rate.



Appendix Figure 21. Electrochemical analysis of **2.6**. a) cyclic voltammogram at different scan rates; b) Scan rate dependence vs. voltage; c) current vs. the square root of scan rate.



Appendix Figure 22. Electrochemical analysis of **2.19**. a) cyclic voltammogram at different scan rates; b) Scan rate dependence vs. voltage; c) current vs. the square root of scan rate



Appendix Figure 23. Electrochemical analysis of **2.20**. a) cyclic voltammogram at different scan rates; b) Scan rate dependence vs. voltage; c) current vs. the square root of scan rate

## Abbreviations

SuRE Successive Ring Expansion

NDI naphthalenediimide

TADF thermally activated delayed fluorescence

RCM ring-closing metathesis

CuAAC CuI-catalyzed azide/alkyne cycloaddition

Ts tosyl.

TBAF tetra-*n*-butylammonium fluoride

DMAP 4-dimethylaminopyridine

PG protecting group

DFT Density Functional Theory

Fmoc fluoromethyloxycarbonyl

Cbz *N*-carboxybenzyl

Fm Fluorenylmethyl

Fc ferrocene

Cp cyclopentadieny

SCE saturated calomel electrode

ROP ring opening polymerisation

rGO reduced graphene oxide

STM scanning tunnelling microscope

CV cyclic voltammetry

Fc-COFNs ferrocene-containing covalent organic framework nanosheets

cTnI cardiac troponin I

AMI acute myocardial infarction

TROP thermal ring-opening polymerisation

DCM dichloromethane

THF tetrahydrofuran  
DMF dimethylformamide  
DPPA diphenylphosphorylazide  
Fmoc-OH 9-fluorenylmethanol  
RT room temperature  
Rs solution resistance effects  
DI deionised  
 $\delta$  chemical shifts  
ppm parts per million  
J coupling constants  
Hz hertz  
s(br) broad singlet  
s singlet  
d doublet  
t triplet  
pt pseudo triplet  
q quartet  
m multiplet  
IR Infrared  
ESI electrospray Ionization  
SiO<sub>2</sub> Fluka silica gel  
RBF round bottomed flask

## References

1 X. Yu and D. Sun, *Molecules.*, 2013, **18**, 6230–6268.

- 2 D. Kauerhof and J. Niemeyer, *ChemPlusChem.*, 2020, **85**, 889-899.
- 3 S. Sinn and F. Biedermann, *Isr. J. Chem.*, 2018, **58**, 357–412.
- 4 K. Sharma and P. Cragg, *Chem. Sens.*, 2011, **1**, 1–18.
- 5 R. Paolesse, S. Nardis, D. Monti, M. Stefanelli and C. Di Natale, *Chem. Rev.*, 2017, **117**, 2517–2583.
- 6 E. Marsault and M. L. Peterson, *J. Med. Chem.*, 2011, **54**, 1961–2004.
- 7 D. A. Guarracino, J. A. Riordan, G. M. Barreto, A. L. Oldfield, C. M. Kouba and D. Agrinoni, *Chem. Rev.*, 2019, **119**, 9915–9949.
- 8 W. A. Loughlin, J. D. A. Tyndall, M. P. Glenn and D. P. Fairlie, *Chem. Rev.*, 2004, **104**, 6085–6118.
- 9 M. Iyoda, J. Yamakawa and M. J. Rahman, *Angew. Chem. Int. Ed.*, 2011, **50**, 10522–10553.
- 10 J. R. Donald and W. P. Unsworth, *Chem. Eur. J.*, 2017, **22**, 8780–8799.
- 11 T. C. Stephens and W. P. Unsworth, *Synlett*, 2020, **31**, 133–146.
- 12 C. D. Payne, B. Franke, M. F. Fisher, F. Hajiaghaalipour, C. E. McAleese, A. Song, C. Eliasson, J. Zhang, A. S. Jayasena, G. Vadlamani, R. J. Clark, R. F. Minchin, J. S. Mylne and K. J. Rosengren, *Chem. Sci.*, **12**, 6670-6683.
- 13 J. F. Howard, J. Vissing, N. E. Gilhus, M. I. Leite, K. Utsugisawa, P. W. Duda, R. Farzaneh-Far, H. Murai and H. Wiendl, *Expert. Opin. Investig. Drugs*, **30**, 483-493.
- 14 K. Sugiyasu, Y. Honsho, R. M. Harrison, A. Sato, T. Yasuda, S. Seki and M. Takeuchi, *J. Am. Chem. Soc.*, 2010, **132**, 14754–14756.
- 15 D. Astruc, *Eur. J. Inorg. Chem.*, 2017, **2017**, 6–29.
- 16 A. Lai, Z. C. Hern and P. L. Diaconescu, *ChemCatChem*, 2019, **11**, 4210–4218.
- 17 N. D. Kirchhofer, Z. D. Rengert, F. W. Dahlquist, T. Q. Nguyen and G. C. Bazan, *Chem.*, 2017, **2**, 240-257.
- 18 X. Xiao, D. Brune, J. He, S. Lindsay, C. B. Gorman and N. Tao, *Chem. Phys.*, **326**, 138-143.

- 19 D. S. Abou, N. A. Thiele, N. T. Gutsche, A. Villmer, H. Zhang, J. J. Woods, K. E. Baidoo, F. E. Escorcía, J. J. Wilson and D. L. J. Thorek, *Chem. Sci.*, 2021, **12**, 3733-3742.
- 20 C. D. Payne, B. Franke, M. F. Fisher, F. Hajiaghaalipour, C. E. McAleese, A. Song, C. Eliasson, J. Zhang, A. S. Jayasena, G. Vadlamani, R. J. Clark, R. F. Minchin, J. S. Mylne and K. J. Rosengren, *Chem. Sci.*, 2021, **12**, 6670-6683.
- 21 A. Luther, K. Moehle, E. Chevalier, G. Dale and D. Obrecht, *Curr. Opin. Chem. Biol.*, 2017, **38**, 45–51.
- 22 ChemSpider, <http://www.chemspider.com/Chemical-Structure.71115966.html>, (accessed November 2022).
- 23 S. T. Schneebeli, M. Frasconi, Z. Liu, Y. Wu, D. M. Gardner, N. L. Strutt, C. Cheng, R. Carmieli, M. R. Wasielewski and J. F. Stoddart, *Angew. Chem.*, 2013, **125**, 13338–13342.
- 24 D. Chen, A.-J. Avestro, Z. Chen, J. Sun, S. Wang, M. Xiao, Z. Erno, M. M. Algaradah, M. S. Nassar, K. Amine, Y. Meng and J. F. Stoddart, *Adv. Mater.*, 2015, **27**, 2907–2912.
- 25 M. R. Talipov, R. Jasti and R. Rathore, *J. Am. Chem. Soc.*, 2015, **137**, 14999-15006.
- 26 A. Saura-Sanmartin, A. Pastor, A. Martinez-Cuezva, G. Cutillas-Font, M. Alajarin and J. Berna, *Chem. Soc. Rev.*, 2022, **51**, 4949–4976.
- 27 W. Zhang, M. Guillén-Soler, S. M.-D. Silva, A. López-Moreno, L. R. González, M. del C. Giménez-López and E. M. Pérez, *Chem. Sci.*, 2022, **13**, 9706–9712.
- 28 M. Krajnc and J. Niemeyer, *Beilstein J. Org. Chem.*, 2022, **18**, 508–523.
- 29 Z. Zhang, J. Zhao, Z. Guo, H. Zhang, H. Pan, Q. Wu, W. You, W. Yu and X. Yan, *Nat. Commun.*, 2022, **13**, 1-9.
- 30 H.-Y. Zhou, D.-W. Zhang, M. Li and C.-F. Chen, *Angew. Chem.*, 2022, **134**, e202117872.
- 31 T. Hayashi, Y. Ohishi, J. Chiba and M. Inouye, *European J. Org. Chem.*, 2022, **2022**, e202200136.
- 32 F. N. Tehrani, K. I. Assaf, R. Hein, C. M. E. Jensen, T. C. Nugent and W. M. Nau, *ACS Catal.*, 2022, **12**, 2261–2269.
- 33 A. Wagner, K. H. Ly, N. Heidary, I. Szabó, T. Földes, K. I. Assaf, S. J. Barrow, K. Sokołowski, M. Al-Hada, N. Kornienko, M. F. Kuehnel, E. Rosta, I. Zebger, W. M. Nau, O. A. Scherman and E. Reisner, *ACS Catal.*, 2019, **10**, 751-761.

- 34 A. Rützel, V. Yrjänä, S. A. Kadam, I. Saar, M. Ilsson, A. Darnell, K. Haav, T. Haljasorg, L. Toom, J. Bobacka and I. Leito, *Beilstein J. Org. Chem.*, 2020, **16**, 1901-1914.
- 35 N. Das Saha, S. Pradhan, R. Sasmal, A. Sarkar, C. M. Berač, J. C. Kölsch, M. Pahwa, S. Show, Y. Rozenholc, Z. Topçu, V. Alessandrini, J. Guibourdenche, V. Tsatsaris, N. Gagey-Eilstein and S. S. Agasti, *J. Am. Chem. Soc.*, 2022, **144**, 14363–14379.
- 36 G. Batur, P. Ermert, J. Zimmermann and D. Obrecht, *Chimia*, 2021, **75**, 508.
- 37 T. C. Stephens, M. Lodi, A. M. Steer, Y. Lin, M. T. Gill and W. P. Unsworth, *Chem. Eur. J.*, 2017, **23**, 13314-13318.
- 38 J. P. S. Farinha, S. Piçarra, K. Miesel and J. M. G. Martinho, *J. Phys. Chem. B.*, 2001, **105**, 10536–10545.
- 39 C. Galli and L. Mandolini, *European. J. Org. Chem.*, 2000, **2000**, 3117–3125.
- 40 H. Bieräugel, H. E. Schoemaker, H. Hiemstra and J. H. van Maarseveen, *Org. Biomol. Chem.*, 2003, **1**, 1830–1832.
- 41 R. S. Phatake, N. B. Nechmad, O. Reany and N. G. Lemcoff, *Adv. Synth. Catal.*, 2022, **364**, 1465–1472.
- 42 C. J. White and A. K. Yudin, *Nat. Chem.*, 2011, **3**, 509–524.
- 43 G. G. Zámbo, J. Mayr, M. J. Sauer, T. P. Schlachta, R. M. Reich and F. E. Kühn, *Dalton Trans.*, 2022, **51**, 13591–13595.
- 44 L. Liang and D. Astruc, *Coord. Chem. Rev.*, 2011, **255**, 2933–2945.
- 45 P. Dowd and S. C. Choi, *J. Am. Chem. Soc.*, 1987, **109**, 6548–6549.
- 46 J. Du, X. Yang, X. Wang, Q. An, X. He, H. Pan and Z. Zuo, *Angew. Chem. Int. Ed.*, 2021, **60**, 5370–5376.
- 47 M. A. Manning, W. Sun, M. E. Light and D. C. Harrowven, *Chem. Commun.*, 2021, **57**, 4556–4559.
- 48 L. A. Paquette, J. Yang and Y. O. Long, *J. Am. Chem. Soc.*, 2002, **124**, 6542–6543.
- 49 J. Yang, T. T. Hoang and G. B. Dudley, *Org. Chem. Front.*, 2019, **6**, 2560–2569.
- 50 S. Kotha, A. Agrawal and Y. Tangella, *RSC Adv.*, 2022, **12**, 14278–14281.
- 51 I. J. Borowitz, G. J. Williams, L. Gross and R. D. Rapp, *J. Org. Chem.*, 1968, **33**, 2013–2020.

- 52 G. Ohloff, J. Becker and K. H. Schulte-Elte, *Helv. Chim. Acta*, 1967, **50**, 705–708.
- 53 A. Klapars, S. Parris, K. W. Anderson and S. L. Buchwald, *J. Am. Chem. Soc.*, 2004, **126**, 3529–3533.
- 54 S. Stanchev and M. Hesse, *Helv. Chim. Acta*, 1989, **72**, 1052–1060.
- 55 U. Kramer, A. Guggisberg, M. Hesse, H. Schmid, *Angew. Chem. Int. Ed. Engl.*, 1977, **16**, 861–862.
- 56 D. Lednicer and C. R. Hauser, *J. Am. Chem. Soc.*, 1957, **79**, 4449–4451.
- 57 J. R. Donald and W. P. Unsworth, *Chem. Eur. J.*, 2017, **23**, 8780–8799.
- 58 C. Kitsiou, J. J. Hindes, P. l'Anson, P. Jackson, T. C. Wilson, E. K. Daly, H. R. Felstead, P. Hearnshaw and W. P. Unsworth, *Angew. Chem. Int. Ed.*, 2015, **54**, 15794–15798.
- 59 A. Lawer, R. G. Epton, T. C. Stephens, K. Y. Palate, M. Lodi, E. Marotte, K. J. Lamb, J. K. Sangha, J. M. Lynam and W. P. Unsworth, *Chem. Eur. J.*, **26**, 12674–12683.
- 60 T. C. Stephens, M. Lodi, A. M. Steer, Y. Lin, M. T. Gill and W. P. Unsworth, *Chem. Eur. J.*, **23**, 13314–13318.
- 61 L. G. Baud, M. A. Manning, H. L. Arkless, T. C. Stephens and W. P. Unsworth, *Chem. Eur. J.*, **23**, 2225–2230.
- 62 T. Wang, Y. Liang, M. Wu, Z. Chen, J. Lin and L. Yang, *Chin. J. Chem. Eng.*, 2015, **23**, 744–754.
- 63 K. Y. Palate, R. G. Epton, A. C. Whitwood, J. M. Lynam and W. P. Unsworth, *Org. Biomol. Chem.*, 2021, **19**, 1404–1411.
- 64 A. Kirschning, *Nat. Prod. Rep.*, 2022, **39**, 2175–2199.
- 65 S. Kobayashi and A. Makino, *Chem. Rev.*, 2009, **109**, 5288–5353.
- 66 T. J. Kealy and P. L. Pauson, *Nature*, 1951, **168**, 1039–1040.
- 67 G. Wilkinson, M. Rosenblum, M. C. Whiting and R. B. Woodward, *J. Am. Chem. Soc.*, 1952, **74**, 2125–2126.
- 68 P. Štěpnička, *Dalton Trans.*, 2022, **51**, 8085–8102.
- 69 M. Rosenblum and J. O. Santer, *J. Am. Chem. Soc.*, 1959, **81**, 5517–5518.
- 70 M. D. Rausch and D. J. Ciappenelli, *J. Organomet. Chem.*, 1967, **10**, 127–136.
- 71 M. D. Rausch, E. O. Fischer and H. Grubert, *J. Am. Chem. Soc.*, 1960, **82**, 76–82.

- 72 D. Guillaneux and H. B. Kagan, *J. Org. Chem.*, 1995, **60**, 2502–2505.
- 73 H. Beitollahi, M. A. Khalilzadeh, S. Tajik, M. Safaei, K. Zhang, H. W. Jang and M. Shokouhimehr, *ACS Omega*, 2020, **5**, 2049–2059.
- 74 G. D. Kong, S. E. Byeon, S. Park, H. Song, S.-Y. Kim and H. J. Yoon, *Adv. Electron. Mater.*, 2020, **6**, 1901157.
- 75 R. J. Nichols, *Curr. Opin. Electrochem.*, 2021, **25**, 100650.
- 76 Y. Liu, X. Qiu, S. Soni and R. C. Chiechi, *Chem. Phys. Rev.*, 2021, **2**, 021303.
- 77 R. Deschenaux, M. Schweissguth and AM. Levelut, *Chem. Commun.*, 1996, 1275–1276.
- 78 B. Sharma and V. Kumar, *J. Med. Chem.*, 2021, **64**, 16865–16921.
- 79 E. Matysiak-Brynda, J. P. Sęk, A. Kasprzak, A. Królikowska, M. Donten, M. Patrzalek, M. Poplawska and A. M. Nowicka, *Biosens. Bioelectron.*, 2019, **128**, 23–31.
- 80 B. S. Kim, J. M. Beebe, C. Olivier, S. Rigaut, D. Touchard, J. G. Kushmerick, X. Y. Zhu and C. D. Frisbie, *J. Phys. Chem. C*, 2008, **27**, 1063-1072.
- 81 X. Xiao, D. Brune, J. He, S. Lindsay, C. B. Gorman and N. Tao, *Chem. Phys.*, 2006, **326**, 138-143.
- 82 J. M. Nelson, P. Nguyen, R. Petersen, H. Rengel, P. M. Macdonald, A. J. Lough, I. Manners, N. P. Raju, J. E. Greedan, S. Barlow and D. O'Hare, *Chem. Eur. J.*, 1997, **3**, 573–584.
- 83 R. Maity, B. S. Birenheide, F. Breher and B. Sarkar, *ChemCatChem*, 2021, **13**, 2337–2370.
- 84 A. J. Salmon, M. L. Williams, A. Hofmann and SA. Poulsen, *Chem. Commun.*, 2012, **48**, 2328–2330.
- 85 M. Camarasa-Gómez, D. Hernangómez-Pérez, M. S. Inkpen, G. Lovat, E. D. Fung, X. Roy, L. Venkataraman and F. Evers, *Nano Lett.*, 2020, **20**, 6381-6386.
- 86 F. Zapata, A. Caballero, A. Espinosa, A. Tárraga and P. Molina, *Inorg. Chem.*, 2009, **48**, 11566–11575.
- 87 S. K. Sahoo, *Dalton Trans.*, 2021, **50**, 11681–11700.
- 88 B. H. Northrop, H.-B. Yang and P. J. Stang, *Chem. Commun.*, 2008, 5896–5908.

- 89 GY. Wu, LJ. Chen, L. Xu, XL. Zhao and HB. Yang, *Coord. Chem. Rev.*, 2018, **369**, 39–75.
- 90 L. Xu, Y. X. Wang, L. J. Chen and H. B. Yang, *Chem. Soc. Rev.*, 2015, **44**, 2148-2167.
- 91 M. S. Inkpen, S. Scheerer, M. Linseis, A. J. P. White, R. F. Winter, T. Albrecht and N. J. Long, *Nat. Chem.*, 2016, **8**, 825-830.
- 92 R. Sun, L. Wang, H. Yu, ZU. Abdin, Y. Chen, J. Huang and R. Tong, *Organometallics*, 2014 **33**, 4560-4573.
- 93 NH. Evans, CJ. Serpell, KE. Christensen and PD. Beer, *Eur. J. Inorg. Chem.*, 2012, **2012**, 939–944.
- 94 L. Pisciottani, M. Douarre, B. Bibal, C. Davies, H. Roberts, B. Kauffmann, SL. Horswell, JH. Tucker and ND. McClenaghan, *Supramol Chem*, 2018, **30**, 869-75.
- 95 Z. Song, J. Song, F. Gao, X. Chen, Q. Wang, Y. Zhao, X. Huang, C. Yang and Q. Wang, *Sens. Actuators B Chem.*, 2022, **368**, 132205.
- 96 T. Moriuchi, *Eur. J. Inorg. Chem.*, 2022, **2022**, e202100902.
- 97 J. Sánchez-Quesada, H. Sun Kim and M. R. Ghadiri, *Angew. Chem. Int. Ed.*, 2001, **40**, 2503–2506.
- 98 S. Chowdhury, D. A. R. Sanders, G. Schatte and H.-B. Kraatz, *Angew. Chem. Int. Ed.*, 2006, **45**, 751–754.
- 99 S. Chowdhury, G. Schatte and H.-B. Kraatz, *Dalton Trans.*, 2004, 1726–1730.
- 100 C. Xiao, W. Wu, W. Liang, D. Zhou, K. Kanagaraj, G. Cheng, D. Su, Z. Zhong, J. J. Chruma and C. Yang, *Angew. Chem. Int. Ed.*, 2020, **58**, 8094-8098.
- 101 J. B. Gilroy, A. D. Russell, A. J. Stonor, L. Chabanne, S. Baljak, M. F. Haddow and I. Manners, *Chem. Sci.*, 2021, **3**, 830-841.
- 102 Y. Sha, Y. Zhang, T. Zhu, S. Tan, Y. Cha, S. L. Craig and C. Tang, *Macromolecules*, 2018, **51**, 9131-9139.
- 103 L. E. Wilson, C. Hassenrück, R. F. Winter, A. J. P. White, T. Albrecht and N. J. Long, *Angew. Chem. Int. Ed.*, 2017, **56**, 6838-6842.
- 104 N. Jiang, Z. Yuan, T. Li, Y. Zhu, Y. S. Chen, L. Lin, J. Zhang, Y. T. Chan and J. Wang, *J. Org. Chem.*, 2018, **83**, 4824-4830.

- 105 Y. Sha, Y. Zhang, T. Zhu, S. Tan, Y. Cha, S. L. Craig and C. Tang, *Macromolecules*, 2018, **51**, 9131-9139.
- 106 L. E. Wilson, C. Hassenrück, R. F. Winter, A. J. P. White, T. Albrecht and N. J. Long, *Eur. J. Inorg. Chem.*, 2017, **2017**, 496-504.
- 107 S. A. Sheppard, T. L. R. Bennett and N. J. Long, *Eur. J. Inorg. Chem.*, 2022, **2022**, e202200055.
- 108 L. Xu, Y. X. Wang, L. J. Chen and H. B. Yang, *Chem. Soc. Rev.*, 2015, **44**, 2148-2167.
- 109 C. R. P. Fulong, S. Kim, A. E. Friedman and T. R. Cook, *Front. Chem.*, 2019, **7**, 567.
- 110 C. Xiao, W. Wu, W. Liang, D. Zhou, K. Kanagaraj, G. Cheng, D. Su, Z. Zhong, J. J. Chruma and C. Yang, *Angew. Chem. - Int. Ed.*, , DOI:10.1002/anie.201916285.
- 111 L. Mikulu, R. Michalicova, V. Iglesias, M. A. Yawer, A. E. Kaifer, P. Lubal and V. Sindelar, *Chem. Eur. J.*, 2020, **59**, 8094-8098.
- 112 B. Adhikari, R. Afrasiabi and HB. Kraatz, *Organometallics*, 2013, **32**, 5899–5905.
- 113 W. Erb, G. Levanen, T. Roisnel and V. Dorcet, *New J. Chem.*, 2018, **42**, 3808–3818.
- 114 J. Bernardini, D. Licursi, I. Anguillesi, P. Cinelli, MB. Coltelli, C. Antonetti, AM. Galletti and A. Lazzeri, *BioResources*, 2017, **12**, 3630-55.
- 115 Merk, <https://www.sigmaaldrich.com/GB/en/technical-documents/technical-article/analytical-chemistry/photometry-and-reflectometry/ir-spectrum-table>, (accessed December 2022).
- 116 T. Kojima, D. Noguchi, T. Nakayama, Y. Inagaki, Y. Shiota, K. Yoshizawa, K. Ohkubo and S. Fukuzumi, *Inorg. Chem.*, 2008, **47**, 886–895.
- 117 S. Quintal, T. S. Morais, C. P. Matos, M. Paula Robalo, M. F. M. Piedade, M. J. Villa de Brito, M. Helena Garcia, M. Marques, C. Maia, L. Campino and J. Madureira, *J. Organomet. Chem.*, 2013, **745**, 299–311.
- 118 L. Barišić, V. Rapić, H. Pritzkow, G. Pavlović and I. Nemet, *J. Organomet. Chem.*, 2003, **682**, 131–142.
- 119 S. B. Kang, H. S. Yim, J. E. Won, M.J. Kim, J.J. Kim, H.K. Kim, S.G. Lee and Y.J. Yoon, *Bull. Korean Chem. Soc.*, 2008, **29**, 1025–1032.
- 120 T. C. Stephens, M. Lodi, A. M. Steer, Y. Lin, M. T. Gill and W. P. Unsworth, *Chem. - Eur. J.*, 2017, **23**, 13314-13318.

- 121 P. Wan, T. A. Modro and K. Yates, *Can. J. Chem.*, 1980, **58**, 2423–2432.
- 122 X. Yang, V. D. Bumbu, P. Liu, X. Li, H. Jiang, E. W. Uffman, L. Guo, W. Zhang, X. Jiang, K. N. Houk and V. B. Birman, *J. Am. Chem. Soc.*, 2012, **134**, 17605–17612.
- 123 D. Siebler, C. Förster and K. Heinze, *Eur. J. Inorg. Chem.*, 2010, **2010**, 3986–3992.
- 124 C. J. McAdam and J. Simpson, *IUCrData*, 2016, **1**, x161769.
- 125 J. E. Halls, A. Hernán-Gómez, A. D. Burrows and F. Marken, *Dalton Trans.*, 2012, **41**, 1475–1480.
- 126 K. Y. Palate, PhD thesis, University of York, 2022.
- 127 M. Kovačević, L. Barišić, R. Ribić, V. P. Peroković, S. Tomić and V. Rapić, *Appl. Organomet. Chem.*, 2012, **26**, 74–79.
- 128 M. Yáñez-S, S. A. Moya, C. Zúñiga and G. Cárdenas-Jirón, *Comput. Theor. Chem.*, 2017, **1118**, 65–74.
- 129 T. L. Bennett, L. A. Wilkinson, J. M. Lok, R. C. O’Toole and N. J. Long, *Organometallics*, 2021, **40**, 1156-1162.
- 130 M. S. Inkpen, T. Albrecht and N. J. Long, *Organometallics*, 2013, **32**, 6053–6060.
- 131 L. A. Wilkinson, L. McNeill, A. J. H. M. Meijer and N. J. Patmore, *J. Am. Chem. Soc.*, 2013, **135**, 1723–1726.
- 132 L. A. Wilkinson, L. McNeill, P. A. Scattergood and N. J. Patmore, *Inorg. Chem.*, 2013, **52**, 9683–9691.
- 133 L. A. Wilkinson, K. B. Vincent, A. J. H. M. Meijer and N. J. Patmore, *Chem. Commun.*, 2016, **52**, 100–103.
- 134 K. Phukan, M. Ganguly and N. Devi, *Synth. Commun.*, 2009, **39**, 2694–2701.
- 135 C. Xiao, W. Wu, W. Liang, D. Zhou, K. Kanagaraj, G. Cheng, D. Su, Z. Zhong, J. J. Chruma and C. Yang, *Angew. Chem. Int. Ed.*, 2020, **59**, 8094-8098.
- 136 W. Han, Y. Shi, T. Xue and T. Wang, *Dyes Pigm.*, 2019, **166**, 140–148.
- 137 W. Erb, G. Levanen, T. Roisnel and V. Dorcet, *New J. Chem.*, 2018, **42**, 3808-3818.
- 138 L. Barišić, V. Rapić, H. Pritzkow, G. Pavlović and I. Nemet, *J. Organomet. Chem.*, 2003, **682**, 131–142.

- 139 S. Quintal, T. S. Morais, C. P. Matos, M. Paula Robalo, M. F. M. Piedade, M. J. Villa de Brito, M. Helena Garcia, M. Marques, C. Maia, L. Campino and J. Madureira, *J. Organomet. Chem.*, 2013, **745**, 299–311.
- 140 S. F. Ekti and D. Hür, *Inorg. Chem. Commun.*, 2008, **11**, 1027–1029.
- 141 Z. Dong, G. Lu, J. Wang, P. Liu and G. Dong, *J. Am. Chem. Soc.*, 2018, **140**, 8551–8562.
- 142 D. Huber, H. Hübner and P. Gmeiner, *J. Med. Chem.*, 2009, **52**, 6860–6870.
- 143 A. K. Diallo, J. Ruiz and D. Astruc, *Org. Lett.*, 2009, **11**, 2635–2637.
- 144 M. Čakić Semenčić, L. Barišić and V. Rapić, *Tetrahedron Asymmetry*, 2007, **18**, 2125–2128.
- 145 A. H. Stoll, P. Mayer and P. Knochel, *Organometallics*, 2007, **26**, 6694–6697.